PSFC/RR-03-5 **DOE-ET-54512-347**

Investigation of Alfvén Eigenmodes in Alcator C-Mod Using Active MHD Spectroscopy

D. Schmittdiel

May 2003

Plasma Science and Fusion Center
Massachusetts Institute of Technology
Cambridge, MA 02139

This work supported by the U.S. Department of Energy, Cooperative Grant No. DE-FC02-99ER54512.

This page left intentionally blank

Investigation of Alfvén Eigenmodes in Alcator C-Mod Using Active MHD Spectroscopy

by

David Anthony Schmittdiel

Submitted to the Department of Nuclear Engineering
in partial fulfillment of the requirements for the degree of

Master of Science in Nuclear Engineering

at the

MASSACHUSETTS INSTITUTE OF TECHNOLOGY

June 2003

Author .....
Department of Nuclear Engineering
May 9, 2003

Certified by .....
Joseph A. Snipes
Research Scientist
Thesis Supervisor

Certified by .....
Ronald R. Parker
Professor, Departments of Electrical and Nuclear Engineering
Thesis Reader

Accepted by .....
Jeffrey Coderre
Chairman, Department Committee on Graduate Students

Investigation of Alfvén Eigenmodes in Alcator C-Mod Using Active MHD Spectroscopy

by

David Anthony Schmittdiel

Submitted to the Department of Nuclear Engineering
on May 9, 2003, in partial fulfillment of the
requirements for the degree of
Master of Science in Nuclear Engineering

Abstract

Alfvén eigenmodes that exist in the shear Alfvén continuum of toroidal magnetic fusion devices may be important for the confinement of energetic particles, particularly fusion-born alpha particles in burning plasma experiments. Interaction between these energetic particles and weakly damped toroidal Alfvén eigenmodes (TAE's) may cause anomalous particle transport leading to incomplete thermalization and possible first wall damage. These consequences must be avoided in next step burning plasma devices and thus an investigation into the stability of TAE's in present machines under reactor-like conditions is essential. Measurement of the damping rate of TAE's will provide insight into this area of research.

The investigation of TAE's on Alcator C-Mod is accomplished by employing the recently completed Active MHD Spectroscopy system. Antennas mounted inside the C-Mod vacuum vessel are driven by a high power amplifier in the TAE range of frequencies and excite modes inside the plasma. Magnetic fluctuation diagnostics provide the plasma response to this excitation. The damping rate is then calculated from the complex transfer function between the antenna current and plasma response signals.

Thesis Supervisor: Joseph A. Snipes
Title: Research Scientist

Thesis Reader: Ronald R. Parker
Title: Professor, Departments of Electrical and Nuclear Engineering

Acknowledgments

I would like to acknowledge my thesis supervisor Dr. Joseph Snipes for invaluable encouragement, support, and feedback during the process of analyzing data and also writing this thesis; Dr. Ronald Parker, my academic advisor, for his help and support throughout the past three years; my family for providing all the love and support I could possibly ask for; my brother Mike for insightful FFL analysis; and Meghann, with whom everything is possible.

Contents

List of Figures

Chapter 1

Motivation

The last three decades have seen enormous progress in the area of fusion research. Magnetic confinement devices, specifically the world leading tokamaks, have become larger and more powerful and achieved important scientific and technological breakthroughs. Conventional tokamaks in operation today have provided much of the fundamental understanding of plasmas that is absolutely necessary to reach the ultimate goal of the global fusion research program: development of commercial fusion reactors to provide inexpensive, abundant, and non-polluting energy.

The next step towards this goal involves the validation of plasma self-heating by alpha particles generated in deuterium-tritium fusion reactions, a regime known as burning plasma science. The Fusion Energy Sciences Advisory Committee (FESAC), with input from the entire fusion community, has recommended that the United States immediately undertake an effort to develop a burning plasma experiment either domestically or as part of a large-scale international tokamak collaboration termed the International Thermonuclear Experimental Reactor (ITER).[1] Thus, it is relevant to study on existing tokamaks today key areas that may prove problematic for the proposed next-step burning plasma devices.

One of the major concerns for a future burning plasma fusion experiment is the excitation of global electromagnetic modes due to interactions with fusion-born alpha

[1]FESAC website: http://www.ofes.fusion.doe.gov/More_HTML/FESAC/Dev.Report.pdf

particles. Since the birth speed of the alpha particles will be in general larger than the Alfvén velocity in a next-step experiment, wave-particle interactions will inevitably occur during the alpha particle thermalization process. Toroidal Alfvén eigenmodes (TAE's), for example, may be driven unstable by the alpha particle pressure gradient in next-step burning plasma experiments and may lead to enhanced transport of the alpha particles. The possibility of increased transport of energetic particles may impair the ability of any next-step device to achieve high fusion gain and also may cause excessive damage to the reactor first wall.

Measurement of the damping rate of these TAE modes in the absence of instability drive due to alpha particles therefore becomes an important exercise. By varying the plasma configuration, results from this experiment may be used not only to verify theoretical models but also to determine which configurations maximize mode damping rates and more effectively prevent possible instabilities. Furthermore, damping rates must be calculated for modes with medium to high toroidal mode numbers because these are predicted to be the most unstable TAE modes in the large tokamaks envisioned for a burning plasma experiment such as ITER.

1.1 Approach

In order to study the damping rate of TAE modes relevant to a future burning plasma experiment, a new diagnostic system was designed and built for the Alcator C-Mod tokamak at MIT's Plasma Science and Fusion Center (PSFC). The Active MHD Spectroscopy system consists of two antennas mounted to the C-MOD vacuum vessel wall, power amplifiers, RF filters, an impedance matching network, and a function generator. This diagnostic is designed to excite high n ($\sim$20) stable TAE's present in C-Mod at high B_{tor} by producing a small magnetic field perturbation ($\sim$0.5 G at the $q = 1.5$ surface). Excitation of modes will occur when the driving frequency of the antennas approaches the dominant TAE resonant frequency in the plasma. The plasma response to this excitation is then captured by magnetic fluctuation coils spaced around the C-Mod vacuum vessel both toroidally and poloidally. By relat-

ing the synchronously detected complex transfer function between the Active MHD antennas and plasma to an equation containing complex poles and residues using a best-fit algorithm, damping rates of the stable TAE modes may be calculated. This technique will also yield information regarding the toroidal mode number of the excited mode if data from several different magnetic pick-up coils are fit simultaneously.

1.2 Thesis Layout

This thesis will be ordered as follows. Chapter 2 will introduce the basic topics of controlled nuclear fusion, the tokamak confinement scheme, and how toroidal Alfvén eigenmodes arise in this device. Chapter 3 will discuss the design and implementation of the Active MHD Spectroscopy system used to excite the TAE modes under consideration. The results from TAE excitation experiments and numerical calculations will be presented in Chapter 4. Finally, Chapter 5 contains the conclusion and suggestions for additional study of the topic. Source code is provided for reference in Appendix A.

Chapter 2

Background

Worldwide energy consumption today is close to 400 quadrillion BTU and expected to rise rapidly as both population and gross domestic product (GDP) increase in developing nations.[1] Energy production globally is predicted to keep pace with demand for at least the first half of the 21st century by relying on existing and yet-to-be discovered fossil fuel reserves. Projections indicate that a global energy deficit, however, will arise around 2050 as demand continues to increase and fossil fuel resources are exhausted. Since growth in national GDP, as well as the maintenance of public health and education, is inextricably linked to the availability of energy, the possible deleterious consequences of a global power shortage are difficult to understate. Concurrently, continued emission of greenhouse gases such as carbon dioxide due to combustion of fossil fuels is expected to double the concentration of carbon in the earth's atmosphere relative to pre-industrial levels by 2100.[2] Global climate change, including a rise in mean surface temperatures, is only one possible dramatic repercussion from sustained human reliance on fossil fuels for primary energy production. Thus it is absolutely imperative that both the United States and the world community have alternative energy sources in place at that time to lessen the severe economic ramifications of an energy shortfall and environmental consequences of increasing anthropogenic carbon emissions. The inescapable conclusion is that expanded and novel energy sources,

[1] U. S. Energy Information Agency webpage: http://www.eia.doe.gov/emeu/iea/tablee1.html
[2] WEA report: http://stone.undp.org/undpweb/seed/wea/pdfs/chapter9.pdf

not just increased energy efficiency or changes in energy regulation, must be instituted both domestically and abroad within the next few decades. Furthermore, these energy sources must be large in magnitude, carbon-free, abundant, inexpensive, and geographically independent. One such source currently under intense domestic and international development that meets all the above criteria is nuclear fusion.

2.1 Fusion

Fusion involves the combining of ions from light elements together to form ions of heavier elements with a corresponding release of energy. Since the binding energy per nucleon in the nucleus decreases with increasing atomic number up to Z $\sim$ 26, all elements up to iron may be fused in an exothermic fusion reaction. The energy released in this type of fusion event is in the form of kinetic energy of the reaction products. The fusion reaction of greatest interest involves the hydrogenic isotopes deuterium and tritium and is illustrated in Figure 2-1.

The fusion reaction rate per unit volume between two different species is given by

$$R = n_1 n_2 \langle \sigma v \rangle$$

where n_i is the density of the i^{th} reacting species and $\langle \sigma v \rangle$ is the product of reaction cross-section and velocity averaged over a Maxwellian velocity distribution. This equation indicates that the fusion process can only be accomplished at highly elevated temperatures- such as the stellar interiors where the gravitational forces are tremendous- because the probability of interaction between positively charged ions is negligible at energies lower than about one kilo-electron volt (1 keV) due to Coulomb repulsion. The deuterium-tritium fusion reaction has the largest reaction rate at the temperatures of interest as shown in Figure 2-2. For this reason, "DT" is considered the fuel for any first-generation fusion reactors.

At these temperatures, atoms are ionized and a plasma containing ions and electrons is formed. The resulting plasma must then be confined in a volume for a certain length of time in order to reach these temperatures and produce fusion reactions. On

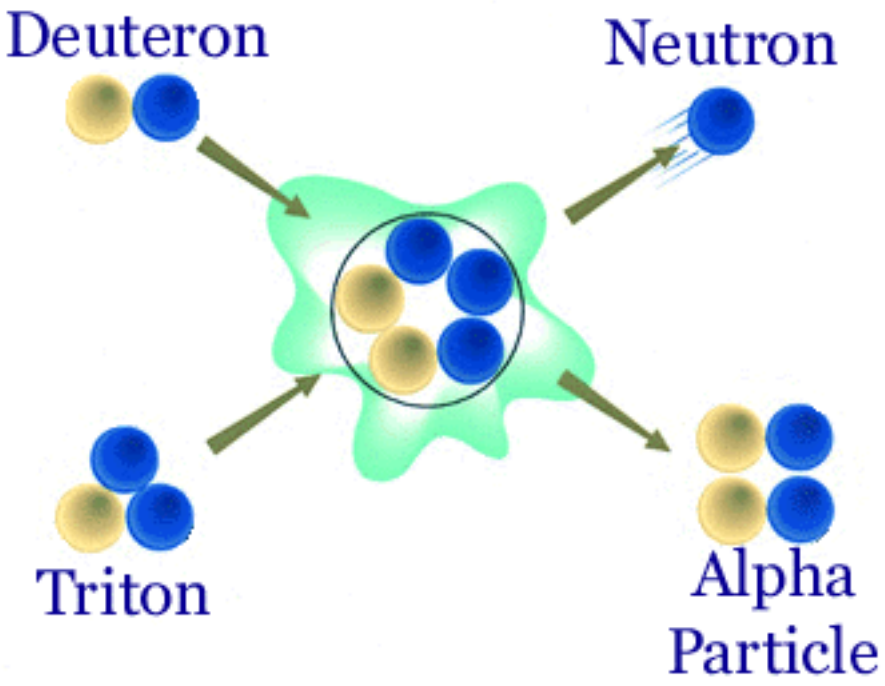

Figure 2-1: Fusion reaction between a deuteron and a triton, producing a neutron, a triton, and kinetic energy

earth, where stellar gravitational forces cannot be recreated, the conditions of confinement necessary for fusion to take place are produced by two different methods: magnetic confinement and inertial confinement. Recent advances and construction of new facilities has increased interest in the latter type, but magnetic confinement concepts received the bulk of funds and efforts during the first 50 years of fusion research. Over that period, numerous magnetic confinement schemes in many different geometries have been proposed.

The governing principle of magnetic confinement fusion is simple: since charged particles follow magnetic field lines in helical orbits, ions and electrons can be confined by these field lines indefinitely, unless acted upon by outside forces. Furthermore, it is essential that these magnetic field lines either end on themselves after a finite number of circular traversals or otherwise remain within the plasma confining volume even after the number of traversals becomes arbitrarily large. Particles travelling

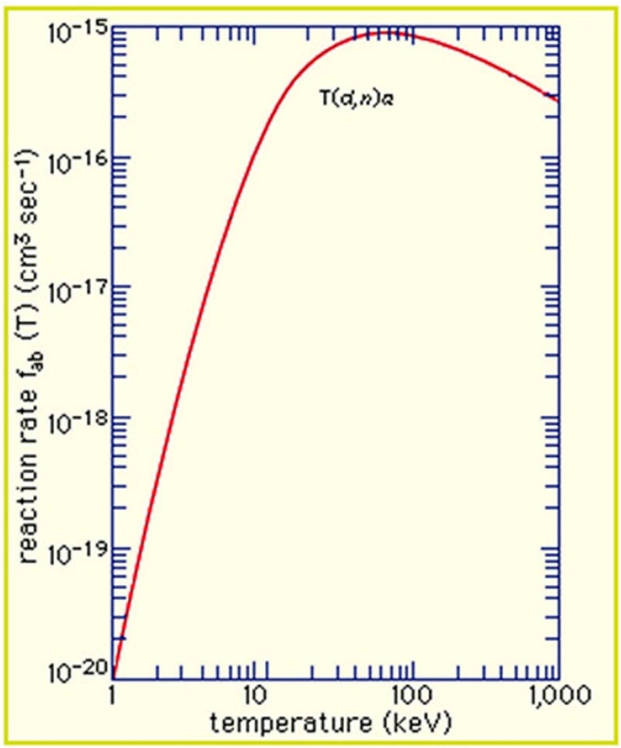

Figure 2-2: Maxwellian averaged reaction rate for DT fusion as a function of temperature in keV

along open field lines, however, are lost from the plasma volume. This requirement necessitates the use of toroidally- or spherically-shaped experiments to eliminate such end-losses from linear devices. The most successful of these devices to be invented is the tokamak.

2.1.1 The Tokamak

The tokamak concept was first proposed by the Russian scientists Tamm and Sakharov in the early 1950's. The term"tokamak" itself is derived from the Russian words "toroidalnaya, kamera, magnitnaya" meaning "toroidal magnetic chamber." Central to the operation of the tokamak (see Figure 2-3 for an illustration) is the superposition of both a poloidal and toroidal magnetic field to produce magnetic field lines that wrap around the device with a helical trajectory. External conductors ring the toroidal vacuum vessel and produce the toroidal field, while a central solenoid

structure maintains a time-varying ohmic heating field. This changing poloidal field induces a toroidal electric field that generates plasma current toroidally and hence a poloidal magnetic field. In this way, a tokamak can be considered a transformer in which flux created by the central solenoid (the primary) is linked to the plasma (the secondary), allowing current to flow through the plasma [1]. Still more current-carrying conductors run in the toroidal direction and serve to shape and control the position of the plasma through the generation of additional poloidal fields.

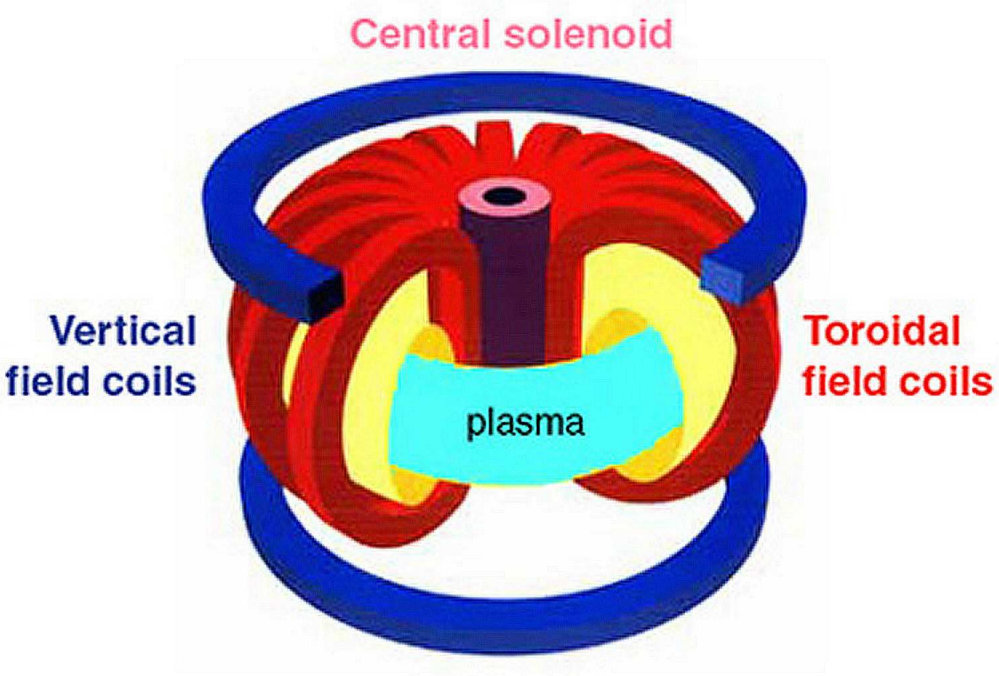

Figure 2-3: Basic illustration of a tokamak toroidal magnetic confinement device showing the central solenoid, toroidal and vertical field coils, and the confined plasma

The superposition of toroidal, poloidal, and vertical magnetic fields allows a tokamak to combine the excellent stability and equilibrium properties of a general screw-pinch configuration without the associated particle end-losses of such a linear device. In modern tokamaks, the plasma shape is not simply circular but rather elongated in the vertical direction. This holds advantages for confinement and achievement of higher plasma pressure [2]. The physical aspects of a non-circular tokamak plasma

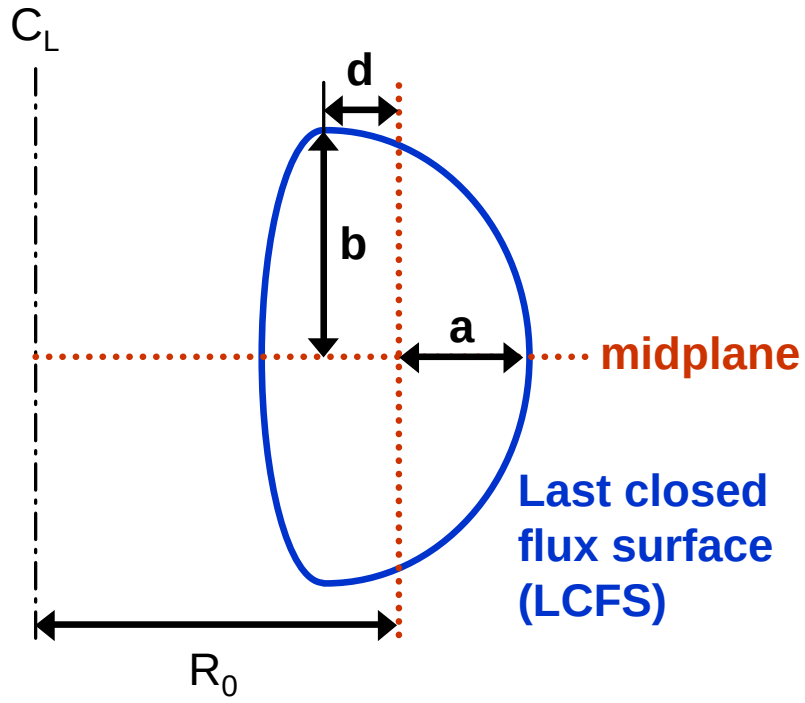

Figure 2-4: Cross section of a non-circular tokamak plasma depicting important physical characteristics

cross-section (see Figure 2-4) may be characterized by the major radius (R_0), minor radius (a), magnetic field strength at R_0 on the midplane (B_0), inverse aspect ratio ($\epsilon = \frac{a}{R_0}$), elongation ($\kappa = \frac{b}{a}$), and triangularity ($\delta = \frac{d}{a}$).

A tokamak plasma is held in equilibrium because the outward forces due to the pressure gradient and expansion of a current loop are countered by the inwardly directed $\vec{J} \times \vec{B}$ forces. The contours of constant pressure, known as magnetic flux surfaces, are nested toroidal surfaces. Plasma is thus confined inside the region where all flux surfaces are closed, that is, all magnetic field lines close on themselves after a certain number of transits around the vacuum vessel toroidally (this is true except at irrational surfaces where field lines **never** close on themselves). Heating of these confined plasma particles by resistive dissipation and other means allows the tokamak to attain the high temperatures and densities needed for fusion reactions to take place. Outside of the last closed flux surface, or separatrix (shown in Figure 2-4), plasma particles are free to travel along open field lines which typically end on

material surfaces inside the vessel. Excessive particle heat loading is detrimental to tokamak performance since sputtering of heavy, cold neutral atoms from these surfaces increases the impurity content of the plasma, effectively reducing the fuel ion density and increasing energy loss due to radiation. Divertor configurations combined with the use of low atomic number refractory materials have been developed and employed successfully in tokamaks around the world.

2.1.2 Tokamak Performance

In the decades since the first tokamaks were developed in the Soviet Union and shown to have performance superior to other existing magnetic confinement devices, many more have been constructed around the world. Physical size as well as magnetic field strength have both increased substantially with corresponding improvements in overall performance. One way to quantify the performance of a fusion device is to calculate the product of plasma density $\times$ confinement time, $n\tau_E$, the merit of which was first described by J. D. Lawson [3] in his pioneering work on the requirements for a fusion power plant. This calculation leads to the aptly named Lawson Criterion

$$n\tau_E \geq 0.6 \times 10^{20} \quad [\mathrm{s/m^3}]$$

which is minimized at the optimum plasma temperature of $T \simeq 20$ keV. The Lawson Criterion represents the condition for fusion "breakeven" where the supplied auxiliary power is equal to the total energy loss from the plasma. However, Lawson failed to account for the heating of an ignited plasma by α-particles (discussed below) in which case the more relevant figure of merit becomes $n\tau_E T$, the product of plasma density $\times$ energy confinement time $\times$ plasma temperature. This is the so-called "fusion triple product" and it may be shown that

$$n\tau_E T > 3 \times 10^{21} \quad [\mathrm{keV \cdot s/m^3}]$$

is required to achieve ignition in a plasma. The fusion gain Q, defined as the ratio of fusion power output to input power, equals 1 at breakeven. Several main thrusts of fusion research today focus on raising the three components of the fusion triple

product to eventually achieve high Q in order to operate a commercial fusion reactor economically. As seen from Figure 2-5, the fusion triple product has been increasing steadily as larger devices have been built to reflect better understanding and technological advances.

The next step envisioned to advance tokamak performance even further is a burning plasma experiment in which the plasma is heated by particles created from fusion reactions. Consider, again, the deuterium-tritium fusion reaction illustrated in Figure 2-1. The reaction products were shown to be a neutron with 14.1 MeV energy and an alpha particle at 3.5 MeV energy. The alpha particle, being positively charged, will be confined by the magnetic fields of the tokamak while the neutron escapes from the plasma immediately. By remaining in the plasma, the alpha particle is free to give up its energy to the surrounding particles as it thermalizes during collisional processes, thereby effectively heating the plasma and partially compensating for natural energy losses via conduction and radiation. In the next-step burning plasma experiment, the fusion gain Q will be $\geq$ 5 - 10, representing the first achievement of net energy production from a fusion process. Understanding plasma physics in the realm of burning plasmas is crucial to optimal construction of a successful burning plasma experiment that will, it is hoped, lead directly to a demonstration electricity-generating fusion reactor.

2.1.3 Inhibiting Optimal Tokamak Performance

However, there are several possible mechanisms that may limit the optimum performance in a next-step burning plasma device. Among the most worrisome problems is the possible interaction of the fusion-born α-particles with waves that are present in the plasma. If the α-particles are ejected before complete thermalization on the background ion species, the overall performance of the fusion plasma may be limited such that Q remains less than 1. This interaction will be revisited after the development of the MHD description of a plasma in the next section.

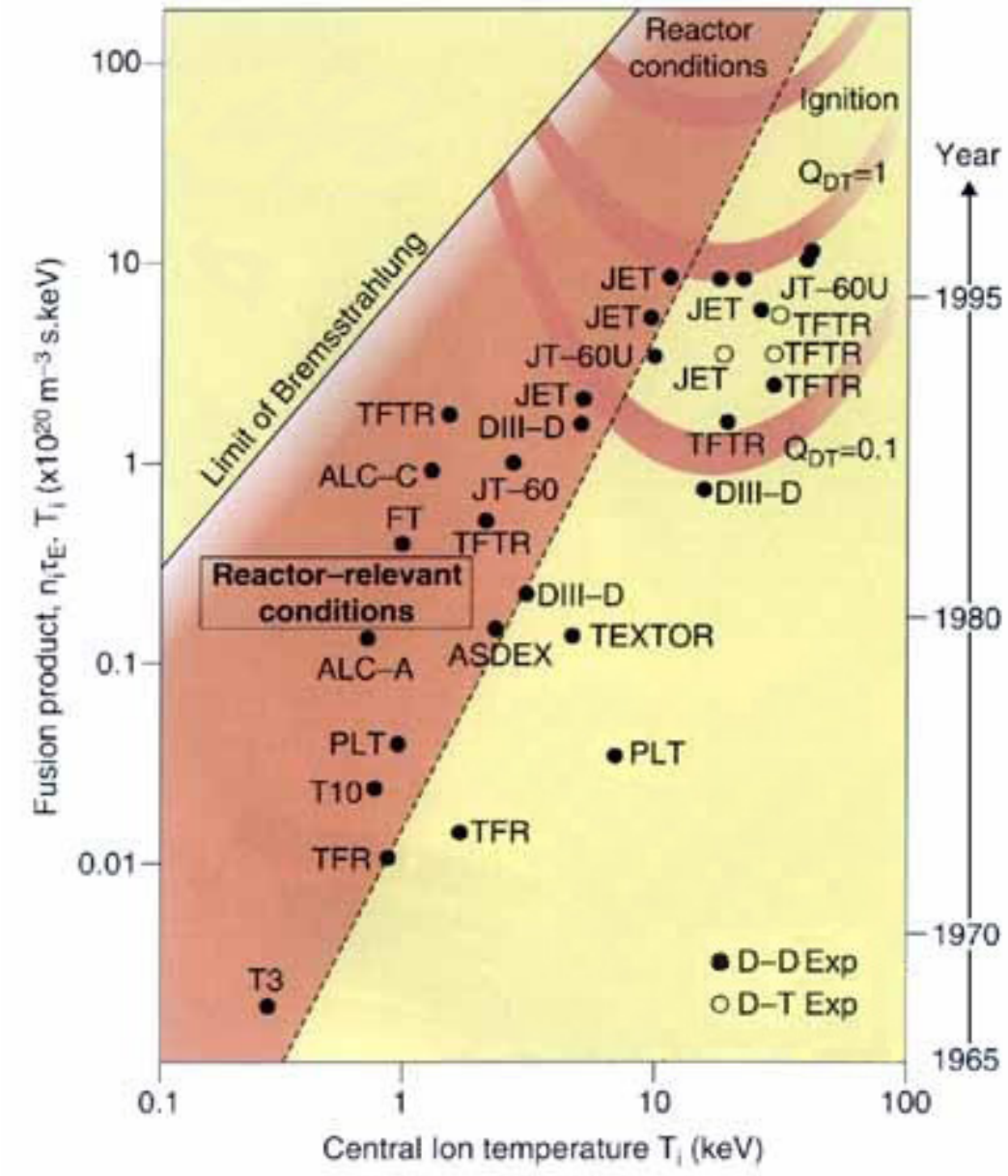

Figure 2-5: Improvement in fusion triple product $n\tau_E T$ as a function of central ion temperature. Data points are labeled with machine name

2.2 MHD Description of Plasmas

Any method for completely describing a plasma and the processes that take place inside must treat the plasma self-consistently. Electric charge density (ρ_c) and current density $\left(\vec{J}\right)$ are sources for Maxwell's equations, which define the electric $\left(\vec{E}\right)$ and magnetic $\left(\vec{B}\right)$ fields present. These fields in turn determine the distribution of the plasma species in both real space ($\vec{r}_i$) and velocity ($\vec{v}_i$) space. The distribution functions, consequently, yield equations for the electric charge density and current density, completing the self-consistent loop. The most basic description of a plasma involves examining the motion of individual particles when subjected to electric and magnetic fields, ignoring the change in the fields due to particle motion. While this approach may yield information regarding the various single particle drifts, it is oftentimes more informative to treat a confined plasma as a conducting fluid immersed in a magnetic field. In this macroscopic approach, known as magnetohydrodynamics (MHD), the identity of the individual plasma particles is neglected and only the motion of fluid elements is investigated (see [2] for complete treatment). The fluid is then described by the charge density, current density, and velocity field such that

$$\rho_c(r) = \sum_j q_j n_j = e(Zn_i - n_e)$$

$$\vec{J}(r) = \sum_j q_j n_j \vec{v}_j = e(Zn_i\vec{v}_i - n_e\vec{v}_e)$$

and these quantities should be considered as averages over all the particles that comprise a fluid element. A sufficient requirement for the validity of the MHD model is that both the ions and electrons in the plasma be collision dominated, which is the usual requirement for the applicability of fluid models. If there are sufficient collisions, a given particle remains reasonably close to its neighbors over the time scales of interest. In this case, the division of the plasma into small fluid elements provides an adequate description of the fluid behavior. Furthermore, these fluid elements are macroscopically large so that this averaging is statistically relevant, but microscopically small such that differential calculus may be applied. However, the MHD description of a plasma may have validity even when the conditions of a colli-

sion dominated plasma do not apply. A more complete discussion of the conditions necessary in order for the MHD model to remain valid is presented in the next section.

2.2.1 Ideal MHD Equations

The ideal MHD equations are essentially the fluid moments of a general kinetic model, coupled with Maxwell's equations and a few general assumptions in order to obtain closure of the system. The basic governing equations for each species α are thus given below

$$\frac{\partial f_\alpha}{\partial t} + \vec{u} \cdot \nabla f_\alpha + \frac{q_\alpha}{m_\alpha}\left(\vec{E} + \vec{u} \times \vec{B}\right) \cdot \nabla_u f_\alpha = \left(\frac{\partial f_\alpha}{\partial t}\right)_c$$

$$\nabla \cdot \vec{E} = \frac{\rho_c}{\epsilon_0}, \quad \nabla \times \vec{E} = -\frac{\partial \vec{B}}{\partial t}$$

$$\nabla \cdot \vec{B} = 0, \quad \nabla \times \vec{B} = \mu_0 \vec{J} + \frac{1}{c^2}\frac{\partial \vec{E}}{\partial t}$$

where the first equation is the Boltzmann equation showing the two forces that act on the fluid particles: the long-range Lorentz force and the short-range force due to collisions. The Boltzmann-Maxwell set of equations above presents a very detailed, comprehensive description of plasma behavior. However, the completeness of this set of non-linear partial differential equations corresponds directly to the inherent complexity in solving them. By taking the mass, momentum, and energy moments of the Boltzmann equation above, the resulting moment equations may be written, but the complete system of equations is not closed due to the presence of higher moments in each succeeding moment equation (velocity, pressure, heat flux, etc). In order to obtain a simplified set of ideal MHD equations that is tractable, it is necessary to introduce approximations and certain asymptotic orderings to eliminate very high-frequency, short-wavelength information from the complete model. First, Maxwell's equations are transformed to the low-frequency limit by allowing $\epsilon_0 \to 0$. Since displacement current is proportional to ϵ_0, this means that electromagnetic waves of interest must have phase velocities much less than the speed of light and that the characteristic thermal velocities must be non-relativistic

$$\frac{\omega}{k} \ll c, \quad v_{the,i} \ll c$$

The net charge is also proportional to ϵ_0 so this restricts the model to focusing on plasma behavior with characteristic frequencies much less than the plasma frequency and characteristic length scales much larger than a Debye length

$$\omega \ll \omega_{pe}, \quad a \gg \lambda_D$$

Furthermore, Poisson's equation states that the charge density is proportional to ϵ_0, so this implies that

$$n_e = n_i = n \text{ (for Z = 1)}$$

which is known as the quasineutrality approximation. For any low-frequency macroscopic charge separation that tends to develop, electrons have adequate time to respond in order to create an electric field that maintains the plasma in local quasineutrality. Next, electron inertia is neglected in the electron momentum equation by allowing $m_e \to 0$. This condition implies that the phenomena being described by the equations occur on a much slower time scale than the time scale on which electrons reach equilibrium. Consequently, more restrictions are placed on the frequency and characteristic length scale

$$\omega \ll \Omega_e, \quad a \gg \rho_{Le}$$

Now one may define the appropriate fluid variables for the mass density, center of mass fluid velocity, current density, and total pressure

$$\rho_m = n(m_i + m_e) \approx n m_i$$

$$\vec{u} = \frac{n_i m_i \vec{v_i} + n_e m_e \vec{v_e}}{n_i m_i + n_e m_e} \approx \vec{v_i} + \frac{m_e}{m_i}\vec{v_e} \approx \vec{v_i}$$

$$\vec{J} = n_i q_i \vec{v_i} + n_e q_e \vec{v_e} \approx ne(\vec{v_i} - \vec{v_e})$$

$$p = p_e + p_i$$

In addition, the assumption that the plasma be collision-dominated requires that

$$\frac{v_{th,i}\tau_{ii}}{a} \sim \frac{v_{th,e}\tau_{ee}}{a} \ll 1$$

where τ_{xy} is the characteristic time for collisions between species x and species y. Using these approximations, the single fluid MHD equations along with the corresponding low-frequency Maxwell's equations are reproduced below

$$\nabla \cdot \vec{B} = 0$$

$$\frac{d\rho_m}{dt} + \nabla \cdot (\rho_m \vec{u}) = 0$$

$$\nabla \times \vec{E} = -\frac{\partial \vec{B}}{\partial t}$$

$$\rho_m \left(\frac{d\vec{u}}{dt} \right) = \vec{J} \times \vec{B} - \nabla p$$

$$\nabla \times \vec{B} = \mu_0 \vec{J}$$

$$\frac{d}{dt}(p\rho^{-\gamma}) = 0$$

It should be noted that in fusion-grade plasmas, the high collisionality assumption is **never** valid. Despite this contradiction that would somehow seem to cast doubt on the predictions made by ideal MHD theory, the MHD model is often still reliable.

2.2.2 Linearized MHD Equations

The equations of ideal MHD given above are nonlinear but can be made more amenable to analysis by linearizing them to identify classes of waves and instabilities. This approach is known as "normal mode analysis" based on the consideration of perturbations to an equilibrium in the form of plane waves. Thus, a non-linear equation may be linearized by assuming that any dynamical variable consists of an equilibrium, zero-order quantity along with a small, time- and space-varying perturbation of the form

$$Q(\vec{x}, t) = Q_0 + Q_1(\vec{x}, t)$$

$$Q_1(\vec{x}, t) = Q_1 \exp[i(\vec{k} \cdot \vec{r} - \omega t)] \qquad \text{where} \quad \frac{|Q_1|}{|Q_0|} \ll 1$$

Applying this formulation in the case of the MHD equations, we find that the four variables are given by

$$\vec{B}(\vec{x}, t) = \vec{B}_0 + \vec{B}_1(\vec{x}, t)$$

$$\vec{\rho}(\vec{x}, t) = \vec{\rho}_0 + \vec{\rho}_1(\vec{x}, t)$$

$$p(\vec{x}, t) = p_0 + p_1(\vec{x}, t)$$

$$\vec{u}(\vec{x}, t) = \vec{u}_1(\vec{x}, t)$$

so that $B_0, \rho_0,$ and $p_0,$ are uniform in space and time and there is no equilibrium flow if we take $u_0 = 0$. Separating the variables into 0^{th} and 1^{st} order terms, MHD

equilibrium is given by

$$\nabla p_0 = \vec{J}_0 \times \vec{B}_0$$

$$\nabla \times \vec{B}_0 = \mu_0 \vec{J}_0$$

$$\nabla \cdot \vec{B}_0 = 0$$

It is clear that equilibrium in a straight cylindrical plasma is achieved by balancing the outwardly directed pressure gradient force with the inwardly directed component of the $\vec{J} \times \vec{B}$ force. The 1^{st} order perturbation corrections to the MHD equations are known as the linearized ideal MHD equations and take the form

$$\frac{\partial \rho_1}{\partial t} + \rho_0 \nabla \cdot \vec{u}_1 = 0$$

$$\rho_0 \frac{\partial \vec{u}_1}{\partial t} = \frac{1}{\mu_0} \left[\left(\nabla \times \vec{B} \right) \times \vec{B} \right]_1 - \nabla p_1 \quad (\text{where } [\,]_1 \text{ denotes } 1^{st} \text{ order quantity}) \tag{2.1}$$

$$\frac{\partial \vec{B}_1}{\partial t} = \nabla \times (\vec{u}_1 \times \vec{B}_0) \tag{2.2}$$

$$p_1 = \left(\gamma \frac{p_0}{\rho_0} \rho_1 \right) = c_s^2 \rho_1$$

2.3 Ideal MHD Modes

There are three different types of ideal MHD waves whose dispersion relationships may be found by solving the linearized ideal MHD equations obtained above: shear Alfvén, compressional Alfvén, and magnetoacoustic waves. These modes are important because some of the most unstable perturbations in a plasma involve Alfvén waves. The dispersion relationship for the ordinary equation is found by further refining Equation 2.1 above and by making use of the well-known vector identity

$$\left(\nabla \times \vec{B} \right) \times \vec{B} = \vec{B} \cdot \nabla \vec{B} - \nabla \left(\frac{\vec{B} \cdot \vec{B}}{2} \right)$$

in which case the resulting first order term may be written

$$\left[\left(\nabla \times \vec{B} \right) \times \vec{B} \right]_1 = \left(\vec{B}_0 \cdot \nabla \right) \vec{B}_1 + \left(\vec{B}_1 \cdot \nabla \right) \vec{B}_0 - \nabla \left(\frac{2\vec{B}_0 \cdot \vec{B}_1}{2} \right)$$

Applying $\frac{\partial}{\partial t}$ to both sides Equation 2.1 yields

$$\rho_0 \frac{\partial^2 \vec{u}_1}{\partial t^2} = \frac{1}{\mu_0}\left[\left(\vec{B}_0 \cdot \nabla\right)\frac{\partial \vec{B}_1}{\partial t} + \left(\frac{\partial \vec{B}_1}{\partial t} \cdot \nabla\right)\vec{B}_0\right] - \nabla \frac{\partial}{\partial t}\left(p_1 + \frac{\vec{B}_0 \cdot \vec{B}_1}{\mu_0}\right) \tag{2.3}$$

Making use of Equation 2.2 from the previous section and another well-known vector identity

$$\frac{\partial \vec{B}_1}{\partial t} = \nabla \times (\vec{u}_1 \times \vec{B}_0) = \left(\vec{B}_0 \cdot \nabla\right)\vec{u}_1 + \vec{u}_1\left(\nabla \cdot \vec{B}_0\right) - (\vec{u}_1 \cdot \nabla)\vec{B}_0 - \vec{B}_0(\nabla \cdot \vec{u}_1)$$

which reduces to

$$\frac{\partial \vec{B}_1}{\partial t} = \left(\vec{B}_0 \cdot \nabla\right)\vec{u}_1$$

assuming fluid incompressibility, $\nabla \cdot \vec{u}_1$, with zero equilibrium flow, $\vec{u}_0 = 0$. Substitution into Equation 2.3 above yields a wave-like equation

$$\frac{\partial^2}{\partial t^2}\vec{u}_1 = \frac{\left(\vec{B}_0 \cdot \nabla\right)^2}{\mu_0 \rho_0}\vec{u}_1 - \frac{1}{\rho_0}\nabla \frac{\partial}{\partial t}\left(p_1 + \frac{\vec{B}_0 \cdot \vec{B}_1}{\mu_0}\right)$$

After taking the divergence of the entire equation and again making use of the incompressibility assumption, the result becomes

$$\nabla^2\left[\frac{\partial}{\partial t}\left(p_1 + \frac{\vec{B}_0 \cdot \vec{B}_1}{\mu_0}\right)\right] = 0$$

so that outside the plasma region the solution must be

$$\frac{\partial}{\partial t}\left(p_1 + \frac{\vec{B}_0 \cdot \vec{B}_1}{\mu_0}\right) = \text{Constant}$$

in which case

$$p_1 + \frac{\vec{B}_0 \cdot \vec{B}_1}{\mu_0} = \text{Constant}$$

Finally, for a homogeneous medium the ordinary Alfvén wave dispersion relation is obtained after transformation to Fourier-Laplace space [4]

$$\mathbf{D} \cdot \vec{v} = 0 \Rightarrow \mathbf{D} = \mu_0 \rho_0 \frac{\partial^2}{\partial t^2} - \left(\vec{B}_0 \cdot \nabla\right)^2 = 0 \Rightarrow \omega^2 = \frac{\left(\vec{k} \cdot \vec{B}_0\right)^2}{\mu_0 \rho_0}$$

Now consider the case when the equilibrium magnetic field is constant in time but contains spatial variation perpendicular to the plane in which the field lines lie. In Cartesian geometry

$$\vec{B}_0(x) = \vec{B}_{0y}(x)\,\hat{y} + \vec{B}_{0z}(x)\,\hat{z}$$

Under these circumstances, the governing relation remains valid but the local variation of Alfvén wave velocity gives rise to a singularity in the hydrodynamic wave equation at the point where the wave phase velocity is equal to the local Alfvén velocity. This leads to the development of a continuous spectrum of Alfvén wave frequencies instead of the discrete modes (eigenmodes) found above for $B_0 =$ constant [5, 6] . In this case, the wave equation has non-trivial solutions for

$$\omega^2 = \omega_A^2(x) = \frac{\left(\vec{k} \cdot \vec{B}_0(x)\right)^2}{\mu_0 \rho_0} \equiv v_A^2(x) k^2 \cos^2\theta$$

$$\text{where } v_A(x) = \frac{|\vec{B}_0(x)|}{\sqrt{\mu_0 \rho_0}}$$

and θ is the angle between the equilibrium magnetic field and the direction of wave propagation. Correspondingly, ω^2 may take on all values of the local Alfvén frequency between the minimum and maximum of ω_A^2, which defines the shear Alfvén continuum of frequencies.

In cylindrical geometry, these continuum modes are heavily damped. A wave launched externally to the plasma by a driving source (such as an antenna) will experience a singular turning point at the plasma layer where its frequency matches exactly the local Alfvén frequency, and the wave energy will be dissipated by resonant wave absorption. It is this local resonant absorption process that has led some to propose the use of Alfvén waves as a plasma heating technique [7, 8].

2.3.1 Alfvén Eigenmodes

Since the preceeding analysis assumed an infinite, unbounded geometry, it is insightful to consider instead a bounded, cylindrical $\left(\epsilon \equiv \frac{a}{R_0} \to 0\right)$ plasma with a nonzero equilibrium current. In this configuration, it is entirely possible for discrete modes to exist with frequencies just below the minimum in the shear Alfvén continuum. These modes are known as global Alfvén eigenmodes (GAE) and were first identified during Alfvén wave heating experiments on the TCV tokamak in Lausanne [9]. At a surface inside the plasma, it is possible for two GAE modes with different poloidal mode numbers, m and m', to have the same frequency if their parallel wave vectors

are equal but opposite in sign

$$k_{\parallel m} = -k_{\parallel m'}$$

These degenerate modes do not interact but a crossing point in the q profile arises where the mode frequencies are equal as shown in Figure 2-6.

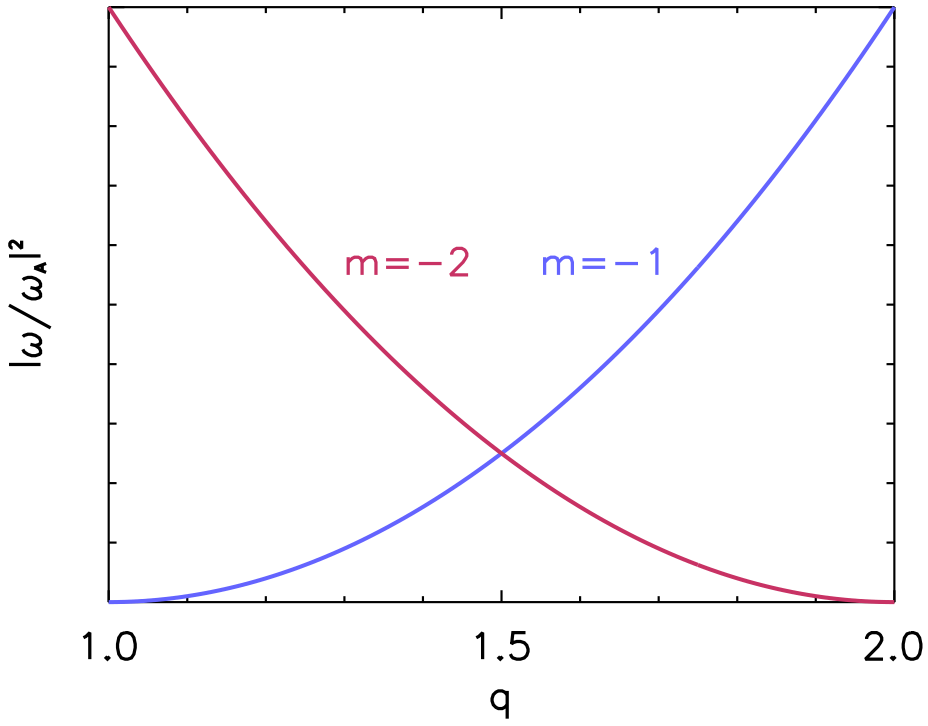

Figure 2-6: Mode frequency degeneracy produces a crossing point in the q profile at q = 1.5 for $m = -1, m' = -2$, and $n = 1$

Since these discrete GAE's lie outside the Alfvén continuum they may not be subject to resonant damping on the continuum, as is the case for shear Alfvén waves propagating in cylindrical geometry. However, toroidal calculations show that all GAE modes with $n \geq 1$ have frequencies much too close to the lower edge of the continuum $\left(\Delta\frac{\omega^2}{\omega_A^2|_{min}} < 1\%\right)$ and immediately damp on the continuum, depositing large amounts power near the plasma surface [9].

To study Alfvén eigenmodes in a tokamak, it is necessary to include a finite aspect ratio ($\epsilon \ll 1$) as a perturbation to cylindrical equilibrium. Toroidicity affects the

discrete cylindrical GAE's as the modes are now coupled together through poloidal harmonics. The consequence of this coupling in toroidal geometry is that a gap in the frequency spectrum appears at the crossing point of the previously non-interacting modes, as depicted in Figure 2-7 [10, 11]. As a result, the gaps act in such a way as

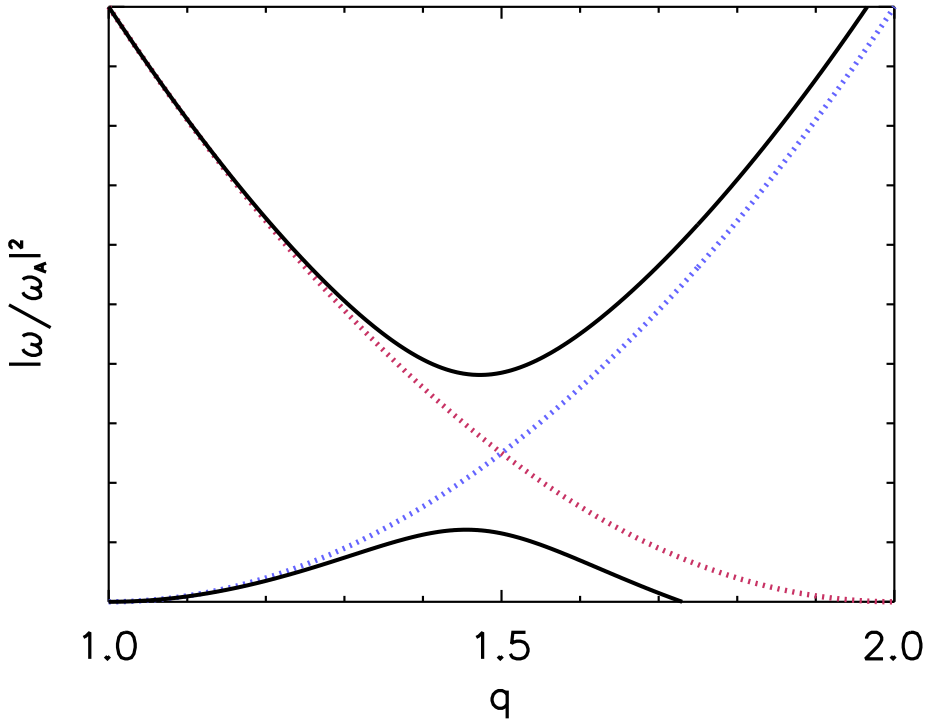

Figure 2-7: Coupling of poloidal harmonics in toroidal geometry eliminates the frequency degeneracy shown previously for GAE modes

to "break up" the continuous Alfvén spectrum into bands and effectively limit the possible frequencies at which the cylindrical modes may propagate.

However, global solutions with *discrete* eigenvalues lying inside of the continuum gaps may also exist in toroidal geometry. At the crossing point where the cylindrical GAE modes are degenerate and the poloidal mode numbers differ by one

$$m + nq_r = \mp\frac{1}{2}$$

Since the parallel wave vector may be expressed as

$$k_{\|} = \frac{1}{R}\left(n \pm \frac{m}{q_r}\right)$$

with n the toroidal mode number, the frequency of these gap modes is then given by

$$\omega = \omega_{TAE} = \frac{v_A}{2q\left(r_0\right)R} = \frac{\omega_A}{2} \Rightarrow \frac{\omega_{TAE}}{\omega_A} = \frac{1}{2}$$

where TAE stands for toroidal Alfvén eigenmode. A TAE mode existing in the gap created by the coupling of two poloidal modes is shown in Figure 2-8 [12, 13].

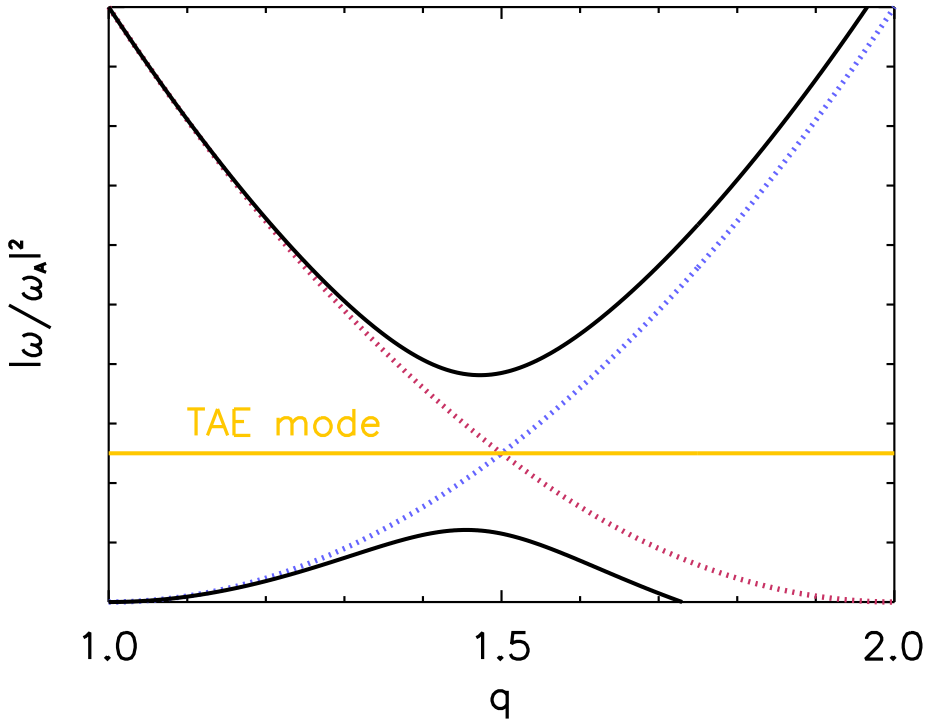

Figure 2-8: Toroidal Alfvén eigenmodes propagate through the gap created by the coupling of poloidal harmonics in toroidal geometry

A TAE mode may be present in a gap of the Alfvén continuum whenever the poloidal mode numbers of the interacting modes differ by one (other modes are possible for mode numbers differing by two or greater). If all the gaps in the Alfvén continuum line up appropriately, it is possible for TAE modes to span the entire

radial extent of the plasma. Sophisticated numerical codes have been developed to reconstruct the Alfvén continuum when many poloidal mode interactions give rise to multiple gaps through which TAE modes may propagate. An example produced by the numerical code CSCAS is illustrated in Figure 2-9.

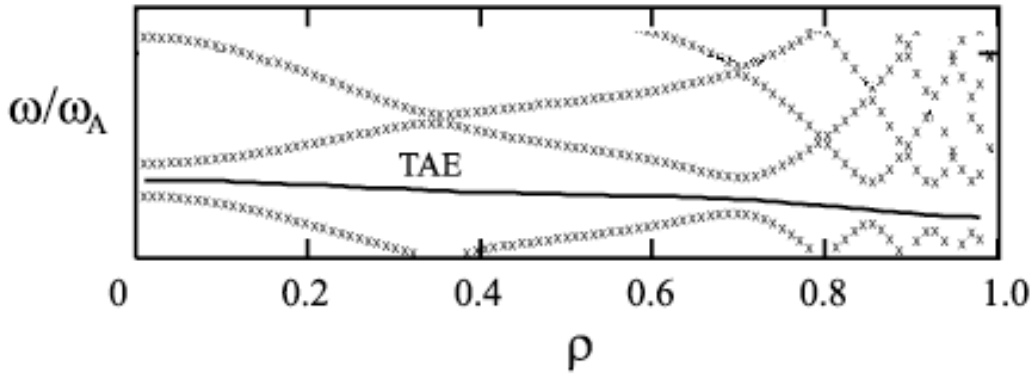

Figure 2-9: The numerical code CSCAS calculates the interaction of many poloidal harmonics for $n = 2$ to produce gaps that allow TAE's to span the entire radial extent of the plasma [14]

2.3.2 TAE's as Instabilities

TAE's are particularly susceptible to instability because they are gap modes and thus avoid damping on the Alfvén continuum. These modes may be driven unstable by tapping the free energy associated with the gradient in the pressure profile of energetic particles in resonance with the modes, such as background ions in the tail of a distribution [15, 16]. In the case of first generation fusion reactors operating with deuterium-tritium (D-T) plasmas, the fusion born α-particles represent another such class of energetic particles. The α-particle birth energy of 3.5 MeV corresponds to a velocity of $v_\alpha = 1.3 \times 10^7$ [m/s] and is usually greater than the typical Alfvén speed in the plasma. As they slow by thermalization on background particles, untrapped α-particles interact with TAE modes via inverse Landau damping. Unstable TAE modes may produce a high level of magnetic field fluctuation, enough to make the α-particle loss time much less than the α-particle slowing down time. In this circum-

stance, TAE modes effectively increase transport of the fusion-born α-particles and eject them from the plasma before complete thermalization on background species occurs. This situation is deleterious to fusion reactor operation since incomplete thermalization lowers the fusion gain and could possibly lead to quenching of the fusion burn altogether.

Opposing the destabilization of TAE modes provided by the free energy in the pressure profile are several important damping mechanisms. First, coupling of TAE's to the Alfvén continuum described in section 2.3 provides a strong dissipative apparatus [17]. Continuum damping occurs when the frequency of the mode approaches too closely or even intersects the boundary of the continuum. Second, a propagating TAE mode may dissipate energy by coupling to a kinetic TAE mode (KTAE) in the gap region [18], a process known as kinetic damping. Third, collisional damping of trapped electrons represents the dominant electron damping mechanism [19, 20]. Last, ion Landau damping provides another mechanism for dissipating energy and limiting the unstable growth rate of the modes [21]. Each particular damping mechanism may be dominant, depending on the toroidal mode number of the excited TAE and specific plasma conditions [22]. Thus, the unstable growth rate of a TAE mode may be written

$$\gamma = \gamma_{drive} - \sum \gamma_{damp}$$

where the summation over γ_{damp} represents the total damping due to all possible damping mechanisms.

2.3.3 Experimental Studies

Increased transport of energetic particles in the core was first observed during TFTR supershot operation in D-T plasmas [23], but similar results may be inferred from data obtained from standard D-D plasmas. Small magnetic field oscillations are observed by magnetic pick-up coils (Mirnov coils) and associated with TAE modes. Since the fusion reaction rate was shown to be dependent on plasma species density and temperature, sawtooth crashes in the observed neutron emission rate correlate well

with these TAE oscillations, indicating that energetic particles are being transported out of the plasma core by TAE modes [24]. The correlation between the two signals is presented in Figure 2-10. In addition, damage to the vacuum vessel wall in TFTR was

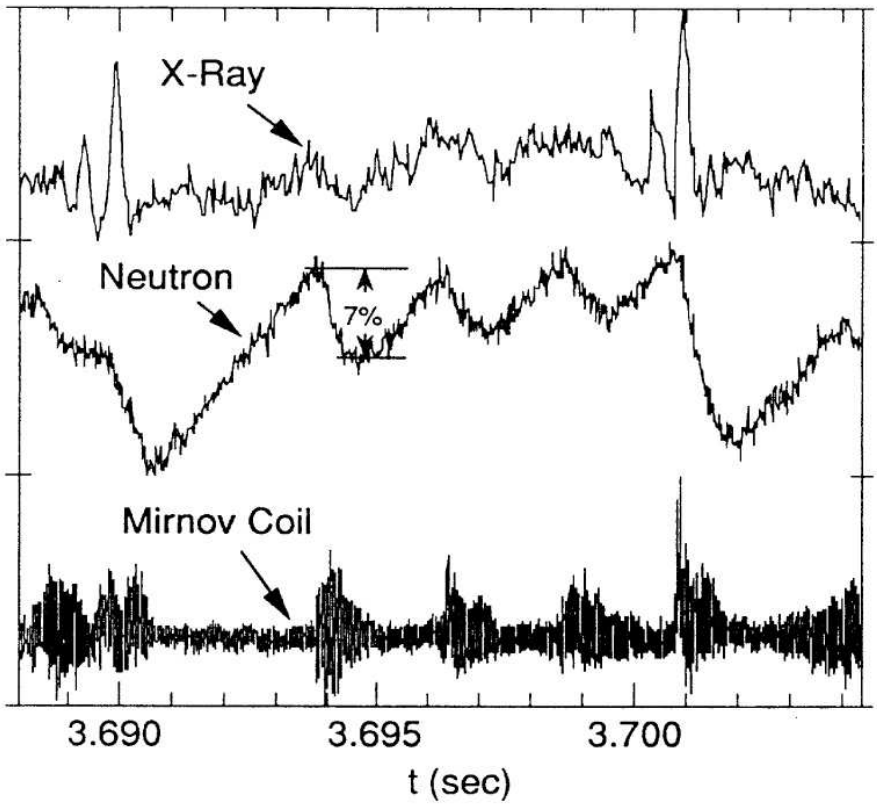

Figure 2-10: Magnetic fluctuations attributed to TAE modes are observed on magnetic pick-up coils and correlate well with sawteeth in the neutron emission rate [24]

observed after high power ICRF operation into D-D plasmas [25]. Energetic particles were ejected from the plasma through magnetic ripple loss mechanisms and caused localized melting of stainless steel debris shields near the bottom of the vacuum vessel.

Excitation of low n number, stable TAE modes in the JET tokamak in England has also been accomplished by the use of external antennas [26]. This was the first study conducted to excite stable, low toroidal mode number TAE modes in the absence of significant instability drive γ_{drive} from fast particle interactions and therefore provide evaluation of mode damping rates for different plasma configurations. A total of eight

saddle coils were installed in the JET vacuum vessel, located 90° apart toroidally to provide several possible phasing scenarios. By actively controlling the output of the power amplifier in real time, the excitation frequency is swept narrowly across the range of frequencies where TAE's are expected according to measurements of magnetic field and density. A single TAE mode is then tracked and the damping rate calculated as a function of time by synchronously detecting the plasma response and antenna excitation (see Figure 2-11). The observed damping rate for discharges

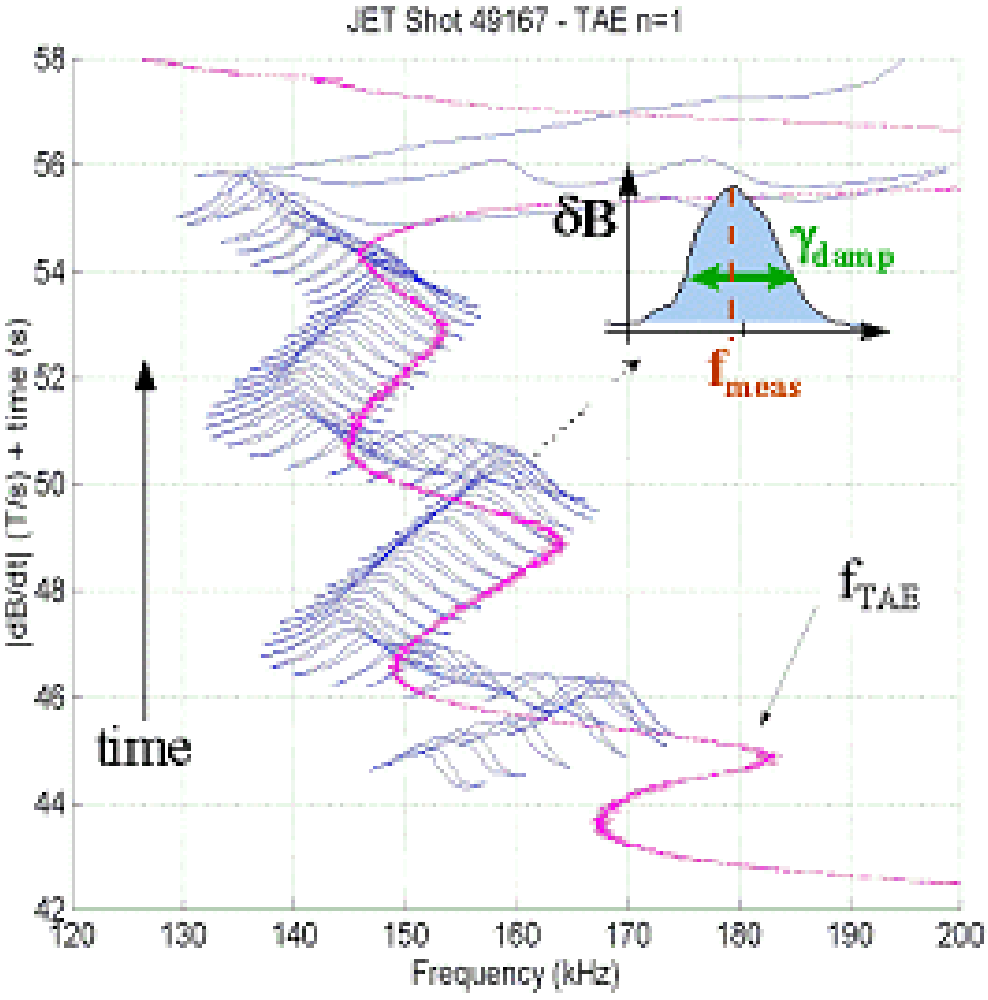

Figure 2-11: Active tracking of a single TAE mode during experimental studies on the JET tokamak [26]

with similar configurations was found to depend most sensitively on the profile of $g(r) = \left[q(r)\,\rho(r)^{-1/2}\right]$ [27]. When g(r) is relatively flat, the gaps in the Alfvén

continuum are aligned and TAE damping on the continuum is minimized. Damping rates were found to be low in this case, on the order of $\sim$.6%. However, when the profile of g(r) was more peaked, continuum gaps were not aligned as well and higher continuum damping contributed to an overall damping rate of $\sim$5%. Recent studies have focused on determining the dependence of the damping rate on plasma parameters such as elongation and triangularity [28].

The experimental work outlined in Chapter 4 of this thesis is meant to extend the studies detailed above to a regime that is more similar to that expected for a next-step burning plasma device. Alcator C-Mod is uniquely configured for this task since it features a high toroidal field and plasma discharges with high electron densities. In the next chapter, the system designed to excite TAE's and calculate their damping rates on C-Mod will be described in detail.

Chapter 3

The Active MHD Spectroscopy System

The Active MHD Spectroscopy system is a new diagnostic on Alcator C-Mod first installed in June 2002 and initially operated in October 2002. Although the Active MHD Spectroscopy system to date has mainly been employed to study the damping rate of stable Alfvén eigenmodes on C-Mod, it has many other possible uses as a diagnostic system. Because the frequency of toroidal Alfvén eigenmodes is inversely proportional to the safety factor, q, the diagnostic system may give useful information on the q profile during a plasma discharge. This data may then be used to further constrain EFIT calculations and allow better reconstructions of the plasma flux surfaces. Furthermore, by exciting lower frequency MHD modes and monitoring their growth rate in real time, the plasma equilibrium may be held close to the marginal stability of these modes. Longer duration plasmas at high β may then be attained by allowing the modes to remain close to the stability limit but not exceed it. This may be accomplished by using the Active MHD diagnostic to provide a feedback signal for systems that control the plasma equilibrium, such as the lower hybrid current drive system to be installed on Alcator C-Mod in 2003.

There are two main subsystems that comprise the Active MHD Spectroscopy system: the excitation side and the data acquisition side. Not surprisingly, the excitation side is responsible for exciting certain modes in the plasma by creating small magnetic

field perturbations. This side is made up of the Active MHD antennas, RF filters, transmission lines, impedance matching circuit, power amplifier, function generator, and associated CAMAC modules. The data acquisition side is concerned with receiving the response of the plasma to external perturbations imposed by the excitation side of the Active MHD diagnostic. Magnetic fluctuation coils, amplifiers, and fast digitizers are contained within this subsystem. Eventually, the two subsystems will work in tandem to form a true "active" diagnostic system. Plasma response captured by the data acquisition side in real time will be used as a feedback signal to control the output from the excitation side. In this way, any mode that one desires to excite and analyze may be "tracked" by instantaneously altering the frequency of the output signal to match the frequency of the excited mode as the plasma conditions evolve in time throughout a discharge.

3.1 Excitation Side

Excitation of stable MHD modes inside the plasma is accomplished by creating a small magnetic field perturbation at the exact frequency of the mode. This small magnetic field is produced by a current flowing in antennas placed inside the vacuum vessel- the Active MHD antennas.

3.1.1 Active MHD Antennas

The design requirements for the Active MHD antennas were numerous for two reasons. First, as detailed above, there are a few possible uses for the Active MHD Spectroscopy system. In addition to driving medium to high toroidal mode number TAE modes, the system might also be used as a large magnetic pick-up coil to measure high frequency plasma oscillations. The antennas must then be isolated electrically from C-Mod machine ground potential to enable their use as magnetic pick-up coils. Furthermore, the antennas must be located very close to the plasma last closed flux surface (LCFS), but not inside it, because the magnitude of magnetic oscillations decays exponentially with distance from the plasma edge. Second, complications in the

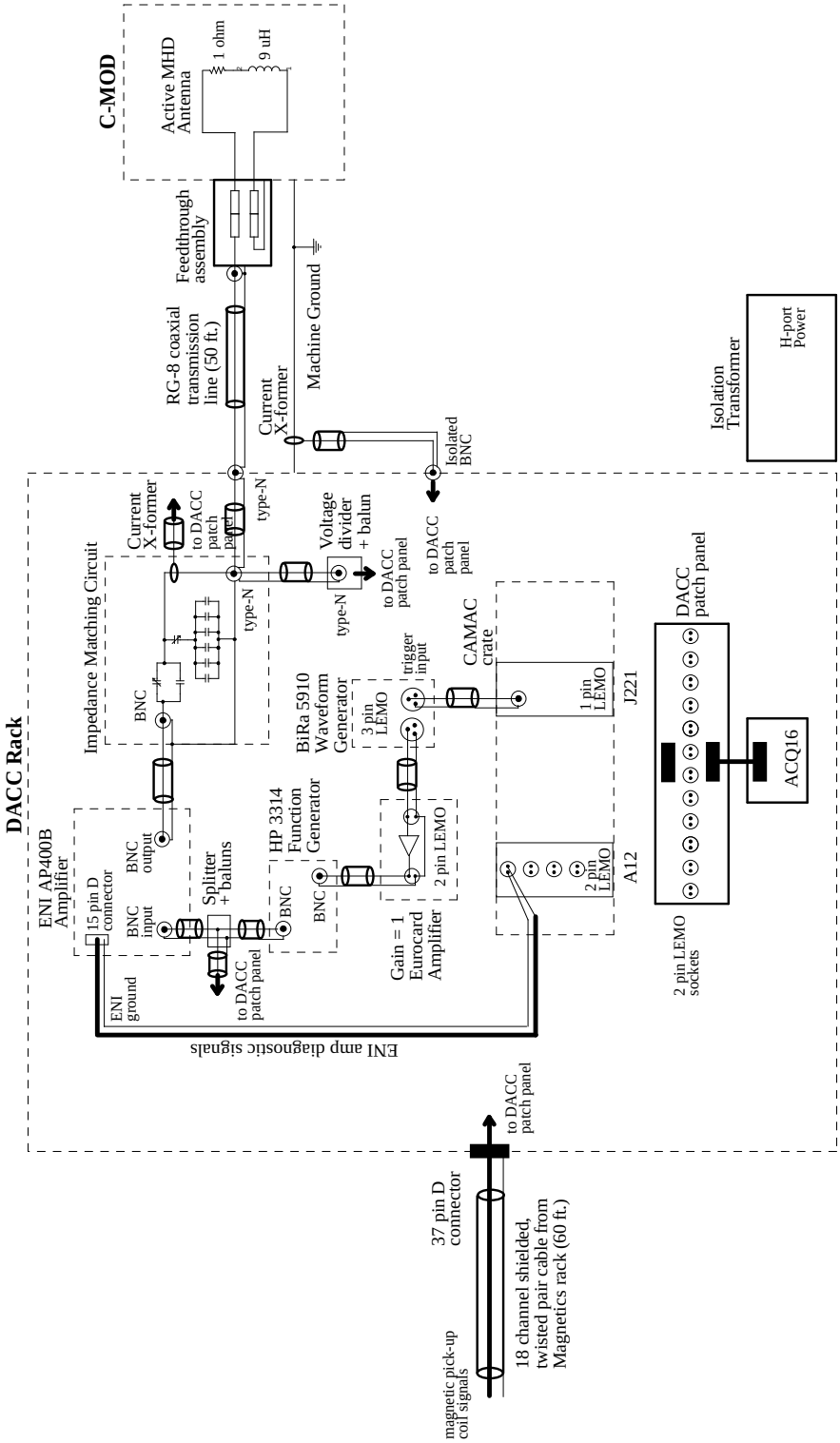

Figure 3-1: Schematic of Active MHD Spectroscopy system

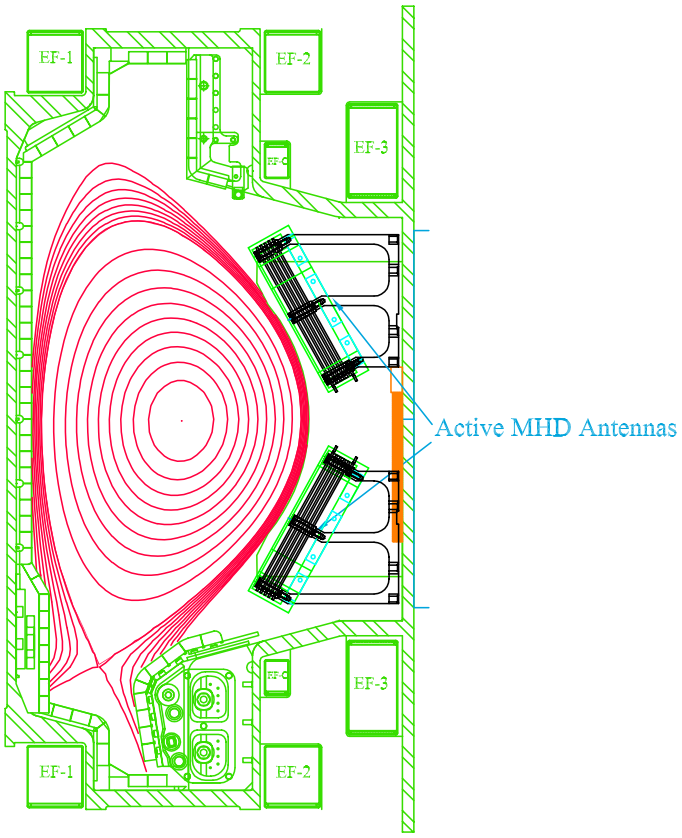

Figure 3-2: Poloidal cross-section of Alcator C-Mod showing placement of Active MHD antennas very near the plasma last closed flux surface

design due to the physical location of the antennas inside the vacuum vessel were of primary importance. The antennas are mounted to the vacuum vessel wall between G and H port, on the H port side of the GH limiter, approximately 2 cm from the LCFS at the point of closest approach. This location necessitates the use of shielding designed to tolerate the large heat fluxes produced by both electron cyclotron discharge cleaning (ECDC, located at H port) and the plasma itself. Because the antennas must be located within a few centimeters of the LCFS, a tremendous amount of heat is conducted from the plasma to the antenna surfaces. Last, the antennas must be constructed to withstand considerable $\vec{J} \times \vec{B}$ forces generated in the event of a 2 MA disruption. Without proper design, the antennas could be ripped off the wall and torn apart.

Taking into consideration all of the above constraints, a prototype was built and completed in April 2001. Subsequent modifications were made to this initial design and finally two antennas were constructed and installed in April 2002 (see Figure 3-3 for a diagram of the upper antenna). The antennas are mirror images of one another along the horizontal midplane surface. Each antenna is based on a Bitter plate magnet design in which stainless steel plates are stacked on top on one another with insulating material placed between the plates. Each plate is really a rectangular loop 15 $\times$ 25 cm in size with conductor cross-section .6 $\times$ .3 cm. The sharp edges of the plates are filed and buffed down after the machining process to form rounded edges. This design reduces the potential for arcing to occur from the sharp edges of a conducting surface. Neighboring "turns" are cut and then welded together to form a spiraling path in which current flows. Stainless steel washers flame-spray coated with a layer of alumina ceramic act as insulators between each turn of the antenna. The welded Bitter plates are mounted to the antenna frame with six stainless steel bolts coated with ceramic to provide electrical isolation. The antenna frame is made of 1.6 $\times$ 1.6 cm stainless steel with six posts of increasing height to provide a tilt to the antenna when mounted to a vertical wall. This design allows the antennas to roughly match the curvature of the plasma surface and remain relatively close to the plasma at all points over the antenna area. Six bolt holes in the antenna frame mate with studs located on the vessel wall in order to secure the antennas in place. The frame was also partially reinforced by welding extra stainless steel material to the side of the frame at the location of the bolt holes.

It is important that the perturbed magnetic field generated by the Active MHD antennas during system operation be small in magnitude compared with the equilibrium magnetic field of the tokamak. Imposing fields that are not negligible may alter the tokamak equilibrium, stimulate extraneous particle transport, or produce nonlinear wave effects [27]. Simulations incorporating the rectangular antenna geometry and finite turn separation were used to calculate the profile of the perturbed magnetic field normal to the antenna surface at a certain perpendicular distance from the antenna. These simulations show that the maximum field produced is $\sim$.5 G at the

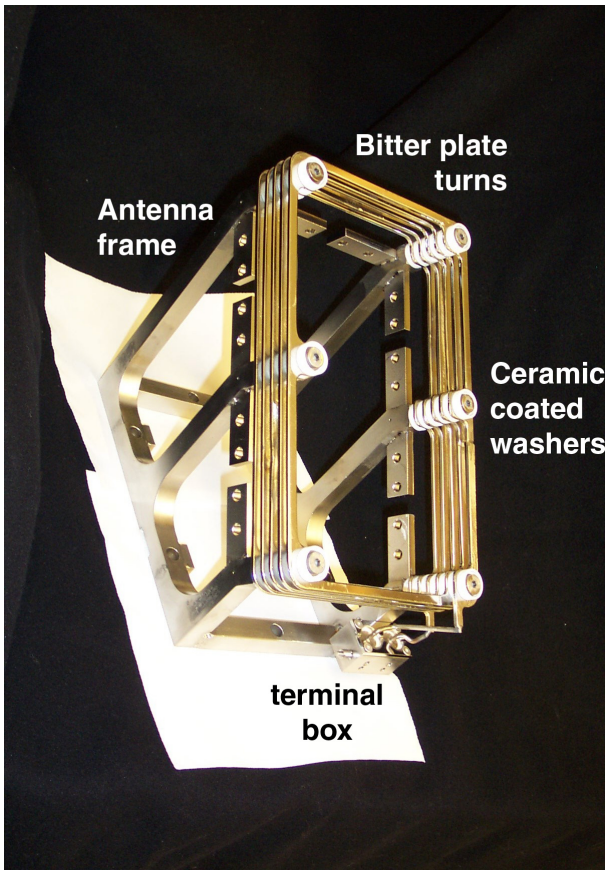

Figure 3-3: Upper Active MHD antenna showing conductor turns mounted on antenna frame

$q = 1.5$ surface in the plasma, nominally 12 cm distant from the antenna (see Figure 3-4). The ratio of perturbed field to equilibrium field is thus $\sim 10^{-5}$ and negligibly small. The profile of the perturbed field may also be used to calculate which toroidal mode numbers are most likely to be excited by the Active MHD Spectroscopy system. Performing a simple one-dimensional calculation by taking into account the toroidal extent of each antenna relative to the total circumference of the plasma indicates that all mode numbers up to approximately 40 are excitable. The probability of excitation, however, is peaked at $n = 0$ and falls slowly up to $n \approx 40$. Therefore all mode numbers up to 40 may be expected in TAE excitation experiments with lower n number modes having the greatest probability of excitation. Future plans call for installation of an additional pair of Active MHD antennas at a location on the opposite side of the machine. In this case, the peak in excitation probability may be shifted towards

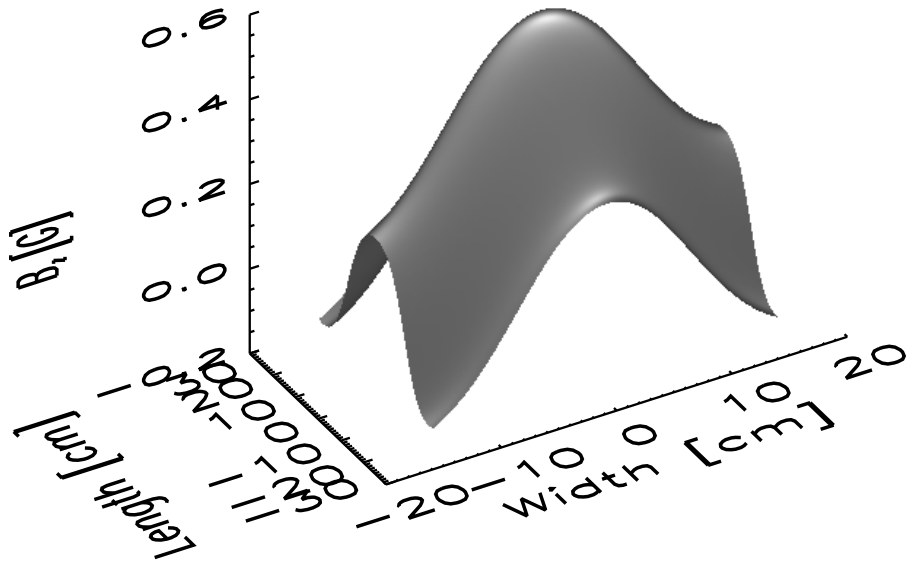

Figure 3-4: Theoretical perpendicular magnetic field profile produced by an Active MHD antenna assuming 10 A of current

either even- or odd-n number modes by alternate phasing of the antenna pairs.

In order to protect the underlying antenna components from tremendous heat flux due to the plasma and ECDC radiation, the entire antenna (excluding the frame) is covered by boron nitride (BN) tiles. Boron nitride is a soft, chalky material that is highly refractive and used in many instances as a plasma-facing component. Each antenna contains 21 tiles that were baked for three days at 1100°C to remove excess hydrogen trapped inside the tiles during the manufacturing process. The tiles are mounted on tabs that were welded to the antenna frame. Shoulder bolts with wave washers hold the tiles firmly in place, and extreme care must be exercised during the torquing procedure to avoid fracture of the BN tiles due to excess compression. Figure 3-5 depicts the covering of the Active MHD antennas by boron nitride tiles.

The terminal box for the leads of each antenna is bolted to the frame near the vessel midplane. Stainless steel conductor was welded to each of the turn leads and bent to enter a small cylinder inside the terminal box. Each cylinder is surrounded by ceramic insulator to avoid shorting the antenna turns to the frame. At the other

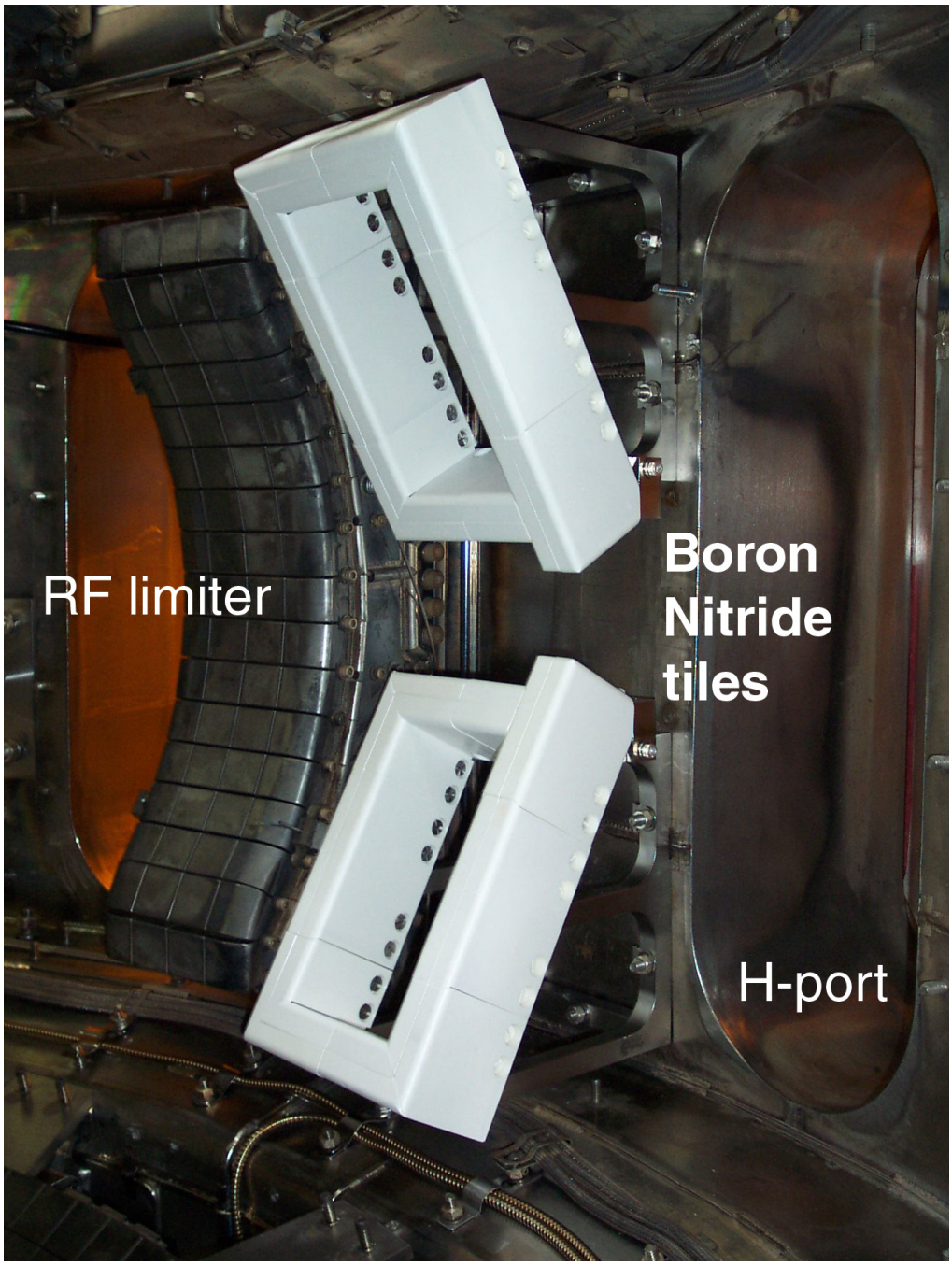

Figure 3-5: Upper and lower Active MHD antennas covered with boron nitride tiles and mounted in the C-Mod vacuum vessel

end of each cylinder, a copper wire is held in place by setscrews. The copper wires are covered with ceramic beads for insulation and are then formed into a twisted pair surrounded by a stainless steel sleeve. This sleeve is held in place against the

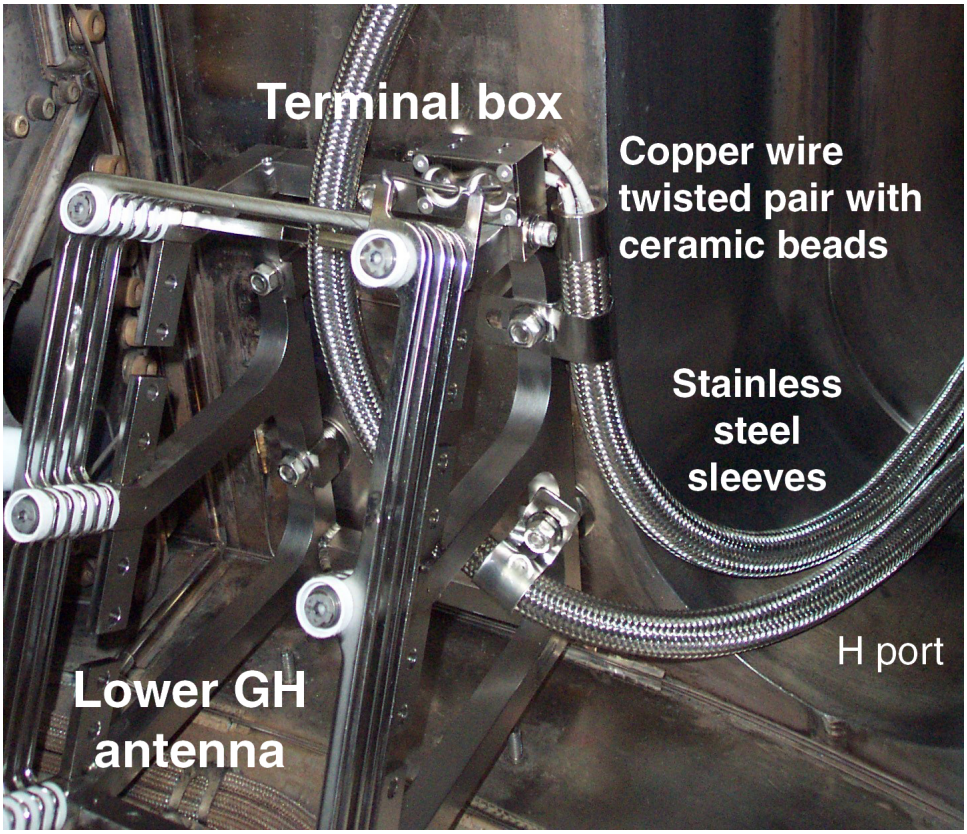

Figure 3-6: Mounted lower Active MHD antenna (without boron nitride tiles) showing placement of external connections

vacuum vessel wall with clamps attached to the antenna frame. Sleeves from the upper and lower antenna then carry the twisted pair leads out through H port where they are then connected to the leads of the vacuum feedthroughs. There are two 15 A, 15 kV feedthroughs at H port corresponding to the upper and lower antennas. Each feedthrough has two pins and passes through a mini-conflat flange bolted to the C-Mod structure. On the air side of the feedthrough, the two pins are encased in a cylindrical aluminum support structure that serves to mate the feedthrough pins with leads from the coaxial connector. One side of an antenna may be grounded to the machine at its support structure. The cable that grounds the Active MHD rack to the

machine is also attached to the support structure, and this ground cable is held close to the Active MHD transmission lines by tie wraps to prevent the introduction of signal noise due to large ground loops. A five-foot length of RG8 cable runs from the type N input connector of the feedthrough assembly to the type N output connector of the RF filters.

3.1.2 RF Filters

The first tests performed in the cell with the network analyzer in July 2002 included only the 50 ft RG8 coaxial transmission lines. After the tests were completed, the transmission lines were subsequently left open-circuited and connected to the feedthrough assembly during plasma operation the next run day. It was then observed that the neutron detectors in the cell became saturated because of the presence of RF interference. Once the cables were disconnected and aluminum foil placed around the feedthrough assembly, as was done on run day 1020719, the neutron detector saturation effect disappeared, effectively determining that the Active MHD system was radiating RF into the cell via the coaxial cables. Correlation between the two signals is shown in Figure 3-7 and it is clear that the raw neutron detector signal on 1020702 is saturated compared with that on 1020719.

Since the Active MHD antennas are located on the G side of H port, the problem was caused by coupling between the antennas and the 4-strap ICRH antenna at J port. RF signal was picked up by the open-circuited Active MHD antennas and transmitted along the transmission line out into the cell. Tests were performed in the lab with a mock-up J-port antenna placed near a prototype Active MHD antenna on the floor of the RF lab. Using the network analyzer, the S_{12} scattering parameter was calculated and the maximum coupling, occurring near the ICRF minority heating frequency of 80 MHz, was found to be greater than -30 dB. Further testing involved pulsing the RF into vacuum and using a network analyzer to measure the coupling between the two antennas. In this case the maximum attenuation measured was approximately -23 dB at 70 MHz. Assuming that 2 MW power output from the J-port antenna is coupled to the Active MHD antennas, this attenuation would correspond to $\sim$10 kW

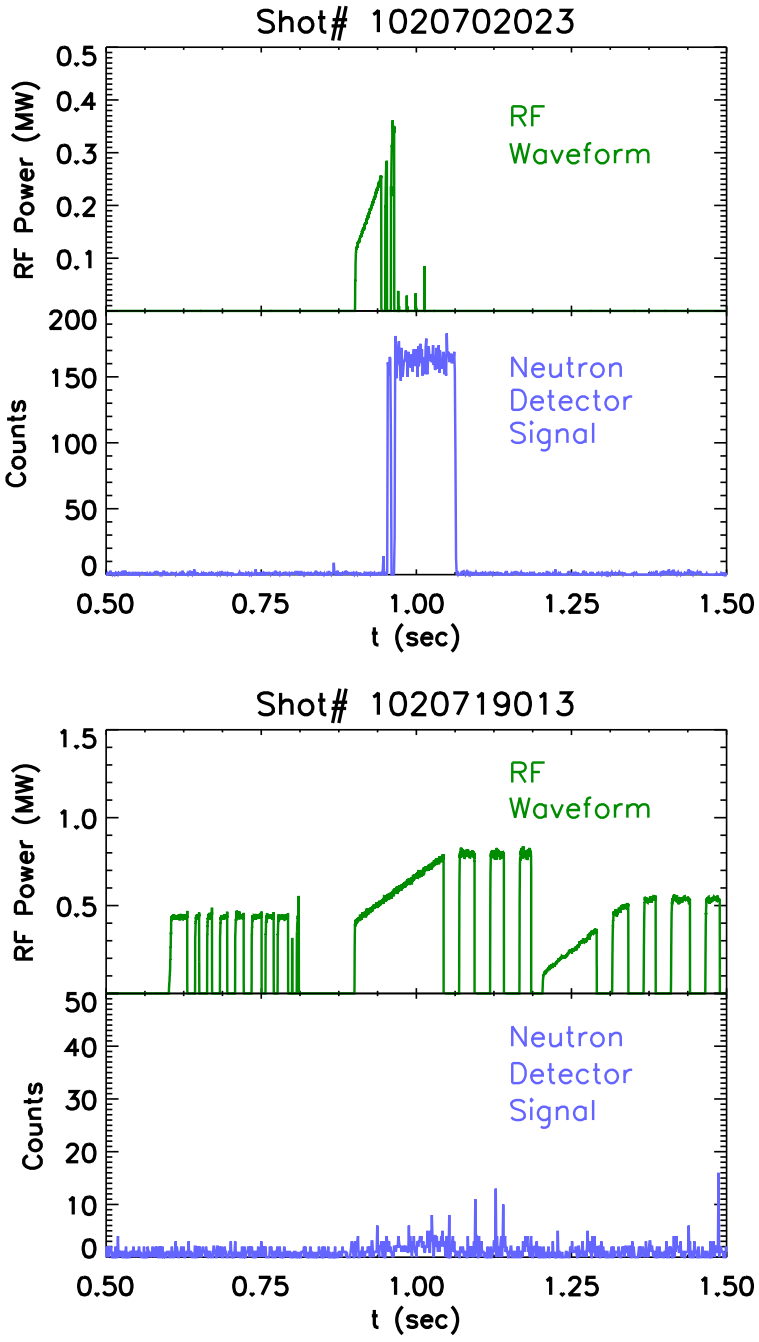

Figure 3-7: Saturated neutron detector signal is seen on 1020702 (top) when transmission lines were left open-circuited in the cell. Time delay is due to high detector discriminator voltage level. Normal neutron detector signal on 1020719 (bottom) after transmission lines were disconnected from Active MHD antennas

of RF signal transiently induced in the Active MHD antenna. Not only would RF signal be radiated from the transmission lines into the cell, RF currents flowing in the circuit could then easily damage the power amplifiers in the Active MHD rack.

The solution to this problem was the inclusion of high power, low-pass RF filters close to the output of the feedthrough. These filters effectively eliminate the RF signal transmitted from the Active MHD antennas and prevent damage to the power amplifiers driving the low frequency signal. A total of four commercial filters from Henry Electronics[1] with a power rating of 10 kW were ordered. Each filter is made up

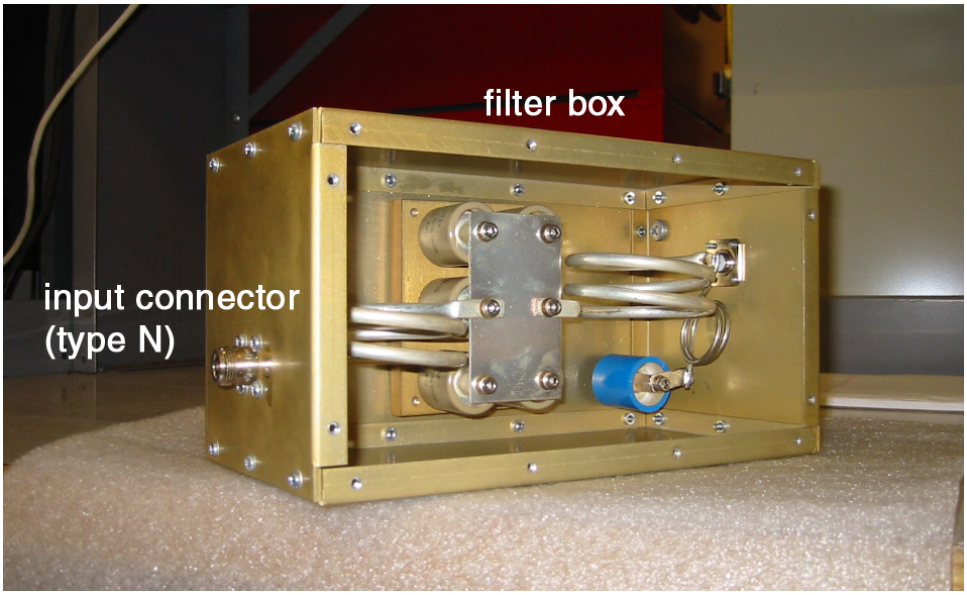

Figure 3-8: 10 kW low-pass filter from Henry Electronics

of high voltage inductors and capacitors rated for high power applications. Standard input and output connectors are type N coaxial but may be changed to other types quite easily, such as the robust 7-16 coaxial connector. The RF filter is represented by the circuit diagram in Figure 3-9, although the values of the individual elements are not explicitly stated.

It is essential that the filters have negligible attenuation at the low frequencies of interest being driven by the Active MHD system (< 1 MHz), but also significant attenuation of the RF signal in the range of frequencies transmitted by the ICRF

[1]Radiodan website: http://www.radiodan.com/Henry/Amp_specs/10kw_lpf.htm

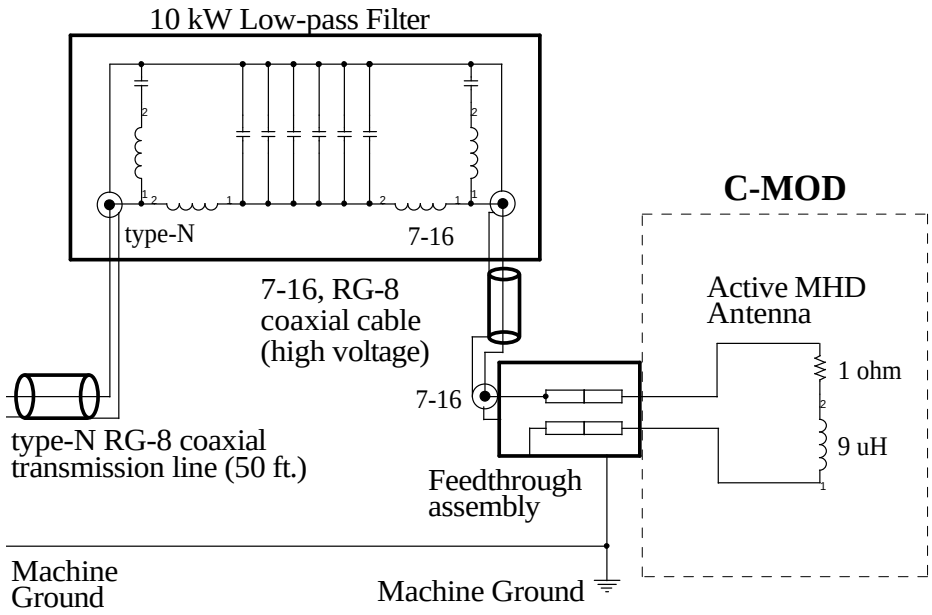

Figure 3-9: Circuit diagram of RF filter and its physical location in the Active MHD system

antennas (40 - 80 MHz). Subsequent tests conducted with the network analyzer show that the filters indeed possess the desired properties in both frequency ranges. Furthermore, tweaking one of the inductors by altering the separation between coil turns led to even greater attenuation in the ICRF frequency band. The graph in Figure 3-10 shows excellent pass band characteristics up to 30 MHz and a sharp drop-off thereafter with attenuation of more than 80 dB at 70 MHz. Unfortunately, signal attenuation then decreases with frequency above 70 MHz, a result that is not unexpected when dealing with real filters. Attenuation by the filter is approximately 65 dB at 80 MHz, enough to sufficiently minimize the induced RF signal carried on the Active MHD transmission line.

It has been demonstrated that these filters adequately protect the sensitive electronics in the Active MHD rack and also prevent radiation of RF signal into the cell during ICRF antenna operation. With the filter in place on run day 1021107 and the ICRF system functioning at $\leq$ 3.5 MW, there was no radiation leakage observable in the cell during C-Mod operation. One filter has been installed at the input of

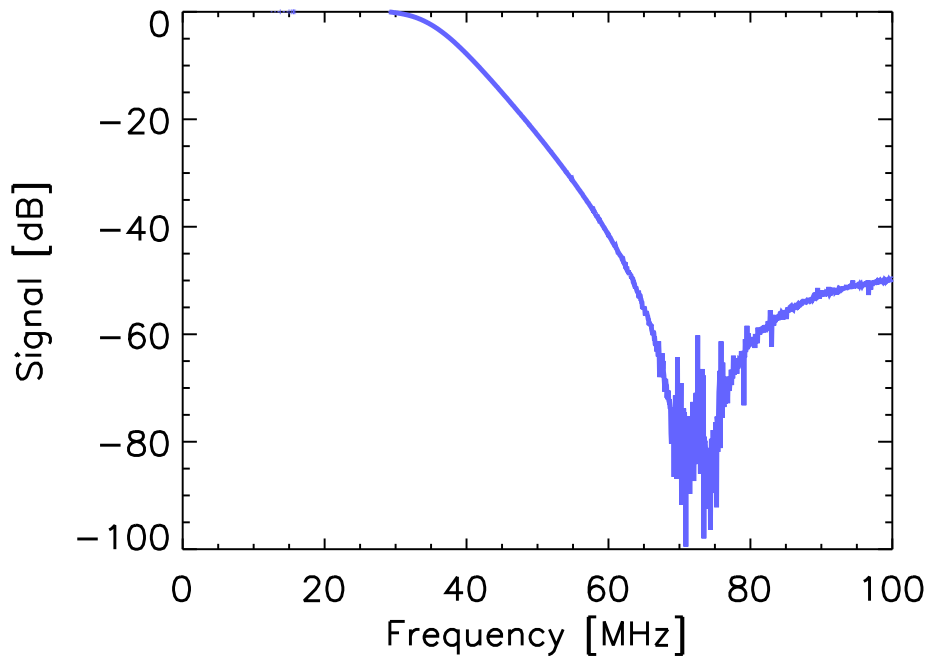

Figure 3-10: Signal attenuation by the low-pass RF filters is negligible in the pass band (< 30 MHz) and substantial in the ICRF range of frequencies (40 - 80 MHz)

each antenna, connected to the antenna feedthrough with a 5 ft RG8 coaxial cable as shown in Figure 3-9. A 50 ft RG8 coaxial transmission line connects the RF filter input to the output of the impedance matching circuit that is located in the Active MHD rack in the northwest corner of the cell.

3.1.3 Impedance Matching Circuit

One of the main impediments to effective operation of the Active MHD diagnostic system is matching the high output impedance of the commercial amplifier, nominally 50 Ω resistive, to the relatively low inductive impedance of the Active MHD antennas. Maximum current in the Active MHD antenna- corresponding to the largest attainable magnetic field perturbations- flows when there is negligible reflection between the amplifier and the antennas. This will only occur when the amplifier "sees" a purely resistive antenna impedance of ∼50 Ω at its output. However, at the intermediate frequencies expected to be driven by the Active MHD system for TAE

excitation experiments (typically 400 - 900 kHz), the antennas are almost completely inductive in nature, exhibiting the characteristic properties of a ∼9 μH inductor in series with a 1 Ω resistor, as shown in Figure 3-11. Deviation from linear impedance increase with frequency near 1 MHz is due to the presence of a resonance in the antenna impedance at approximately 4 MHz. In order to effectively match the two

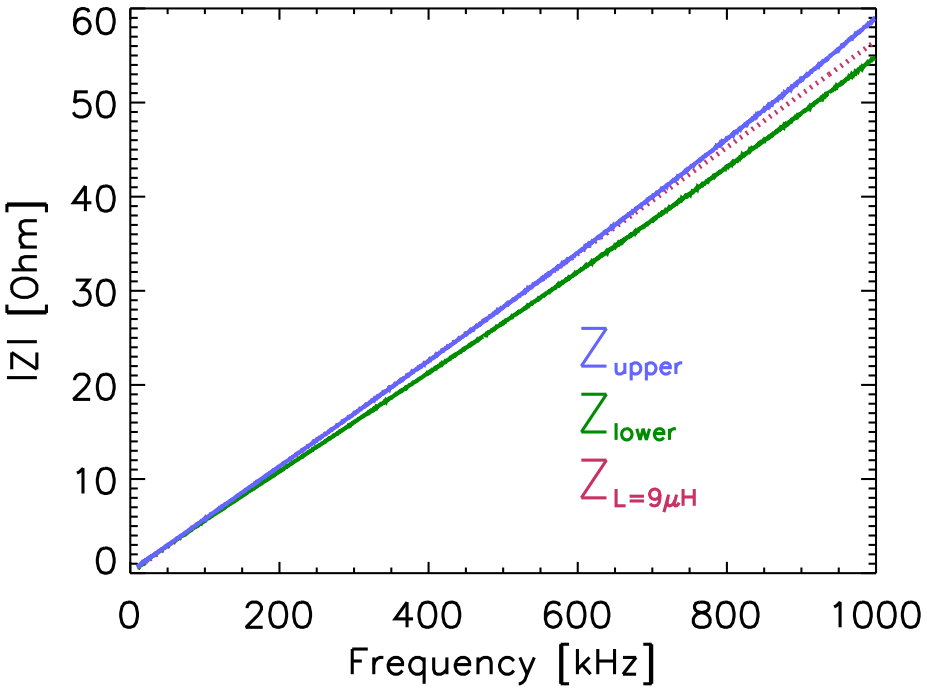

Figure 3-11: Magnitude of the complex antenna impedance from 10 kHz - 1 MHz

different impedances, an impedance matching circuit was designed and fabricated at the PSFC. It consists of capacitors whose values are specifically chosen to tune out the inductive components of the Active MHD antennas at a particular frequency and present a purely resistive impedance of 50 Ω to the amplifier. In order to provide a small range of frequencies at which the system may be successfully tuned, variable capacitors were also included in the design of the impedance matching unit. The illustration in Figure 3-12 shows the complete circuit diagram and placement within the Active MHD system.

Initial experiments with the Active MHD system specified constant antenna ex-

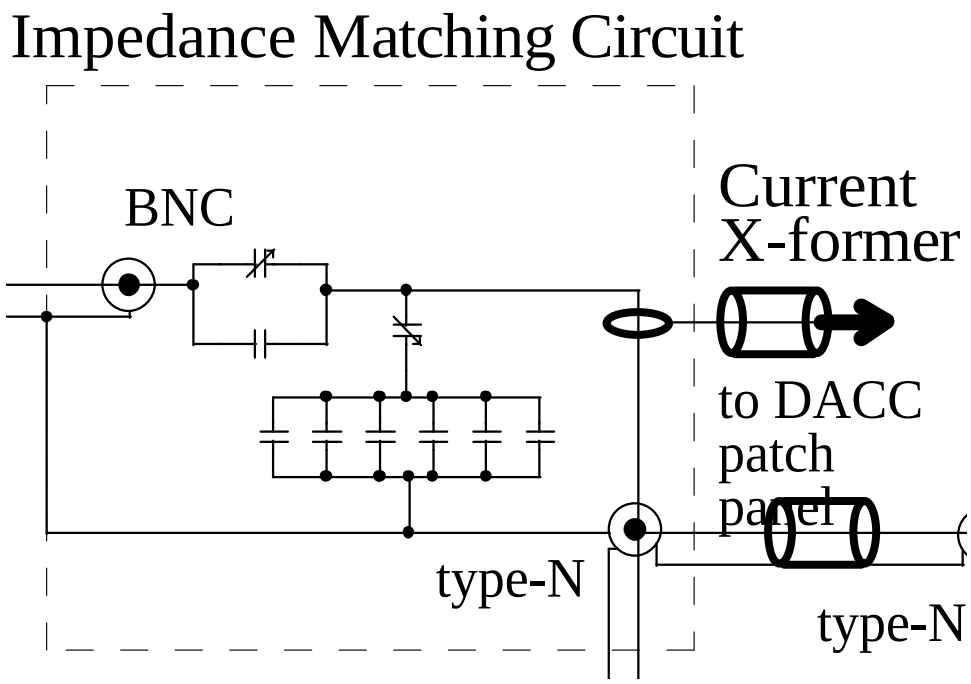

Figure 3-12: Circuit diagram for the impedance matching unit

citation at 420 kHz in order to facilitate impedance matching. By transmitting at constant frequency, it is possible to tune the system before plasma operation to achieve maximum current and power delivered to the antennas. The fixed capacitors shown above were chosen before installation of the impedance matching circuit to create a perfect match at 420 kHz given the impedance of the antennas at this frequency. Finer tuning once the unit is installed is accomplished by adjusting the "series" and "parallel" variable capacitors as depicted above. A digital oscilloscope may be employed to examine the amplitude of a test signal at 420 kHz as the variable capacitors are precisely tuned in order to establish the best possible match at the frequency of interest. The forward and reverse power measured at the amplifier is shown in Figure 3-13 during actual system operation, illustrating the fact that reverse power is small compared to the forward power driven into the antennas and thus the matching unit is performing adequately. Note also that, unlike ICRF heating, impedance matching is not affected by the presence of the plasma.

As previously stated, future experiments involving the Active MHD Spectroscopy

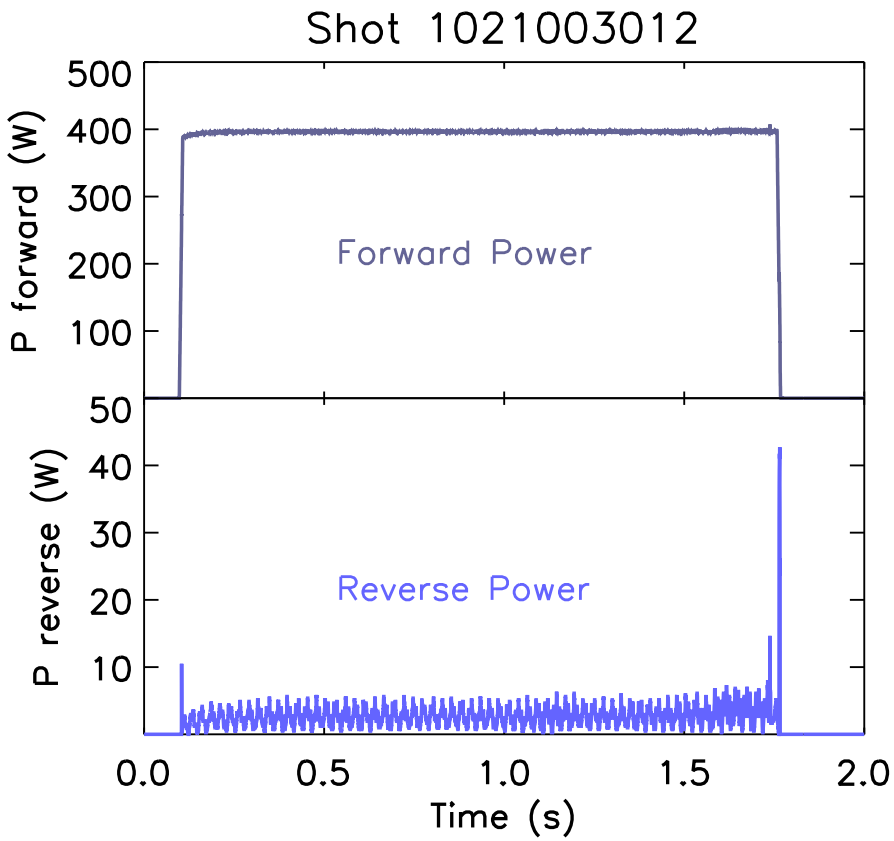

Figure 3-13: Forward and reverse power output of the Active MHD system on run day 1021003

system will utilize active tracking of eigenmodes in the plasma and thus will necessitate changing the driving frequency in real time in response to a feedback signal from the data acquisition side of the system. The impedance matching unit will then be modified to include active adjustment of the variable capacitors in order to maintain tuning as the frequency is swept higher and lower. It is also worth noting that for excitation of lower frequency MHD modes (typically 1 - 50 kHz), the reactive component of antenna impedance is negligible compared to the resistive component (see Figure 3-11) and an impedance matching circuit is not necessary to ensure maximum antenna current and amplifier power.

3.1.4 Amplifiers

Unquestionably one of the most important components contained in the excitation side of the Active MHD Spectroscopy system is the amplifier, a component that like the antennas faces numerous design requirements. The amplifier must be high power, that is, capable of delivering up to 20 A of current into each antenna at a voltage level approaching 1 kV. It is also essential that the amplifier provide excellent response in a broad range of frequencies from 1 kHz - 900 kHz. This is due to the multiple applications envisioned for the Active MHD system and therefore multiple frequency ranges of interest: 1 - 10 kHz for low frequency MHD modes, 100 - 400 kHz for excitation of TAE modes in the current-rise portion of a C-Mod discharge, and 450 - 900 kHz for excitation of TAE modes in the flat-top portion of the discharge. Furthermore, since the diagnostic system must be capable of eventually sweeping at a high rate over each band detailed above, the amplifier must have a fast response to changes in the frequency of the input signal. Finally, remote operation of the amplifier via an electronic trigger is also essential.

Extensive work was carried out prior to system installation in order to locate a suitable amplifier available on the commercial market. Unfortunately, there are few applications for amplifiers in this frequency range and this fact consequently limited the available options to a few possible models. The ENI AP400B amplifier was chosen ultimately because its frequency range overlapped quite well with the required range for TAE excitation experiments. Specifications for the ENI AP400B (shown in Figure 3-14) amplifier are as follows

- Gain flatness of ± 1.5 dB over frequency range of 80 kHz - 2.7 MHz
- Up to 400 W output power into a 50 Ω matched load
- 50 Ω output impedance
- Externally controllable via 15 pin rear connector
- Rise time of $< .1$ ms in pulsed operation

Figure 3-14: ENI AP400B commercial amplifier, capable of delivering 400 W into a 50 Ω matched load

Tests conducted prior to system operation showed that the amplifier did indeed function optimally when provided with a 50 Ω matched load over the rated frequency range. This further indicates the necessity of using the impedance matching system to cancel the reactive impedance at the amplifier output. The 15 pin rear connector provides an input for start and stop commands, as well as desired forward power output. In addition, the rear connector provides outputs related to several important amplifier diagnostics such as forward and reverse power level for convenient monitoring of the system. An internal potentiometer determines signal amplitude in volts per watt of power. Several TTL outputs are also available to specify when the overheat or maximum voltage conditions have been met. Overall, the ENI AP400B amplifier operated exquisitely during initial experiments with the Active MHD Spectroscopy system.

However, because the minimum frequency of amplification attainable with the ENI AP400B amplifier is greater than the range of frequencies necessary for exciting low

frequency MHD modes, an alternate solution was sought. Concurrent to experimental studies on stable TAE modes, a high power amplifier capable of spanning the entire frequency range of interest was designed and built by William Burke at the Plasma Science and Fusion Center. The MHD amplifier is essentially a power MOSFET design and operates with two distinct frequency bands: 4 - 80 kHz for low frequency operation and 310 - 940 kHz for higher frequency TAE excitation studies. A built-in "high/low" range switch may be adjusted to change frequency ranges between shots. As previously stated, in the low frequency range no matching circuit is required because the reactive component of the antenna impedance is small. At the higher frequency end, a single series capacitor is necessary for matching the antenna load to the output impedance of the MHD amplifier at one specific frequency, and the value of this capacitor must be determined before system operation in order to finely tune the excitation frequency. Tests conducted with the MHD amplifier driving the Active MHD antennas in vacuum produced a current of 25 A at 10 kHz using a $\pm$100 V regulated power supply. The MHD amplifier drove the Active MHD antennas on run day 1021107 with exceptional results, as shown in Figure 3-15.

A high power, $\pm$125 V power supply designed at the PSFC is nearing completion and should be incorporated into the system during the next C-Mod run campaign. With this power supply in place, the amplifier should easily provide 25 A of current into both antennas simultaneously throughout the frequency range of interest. Simultaneous excitation of both the upper and lower antennas will provide additional flexibility as to which modes may be selectively excited by the Active MHD system.

3.1.5 Function Generator

The signal input to the amplifier is produced by an HP 3314A function generator. This specific model function generator is capable of producing sine, square, triangle, or custom waveforms with frequencies from .001 Hz to 19.99 MHz. An essential feature on the HP 3314A is that the output frequency may be externally modulated over a range of +10% to -100% of the programmed frequency through the voltage controlled oscillator (VCO) input. Applying a signal to this VCO input will allow the

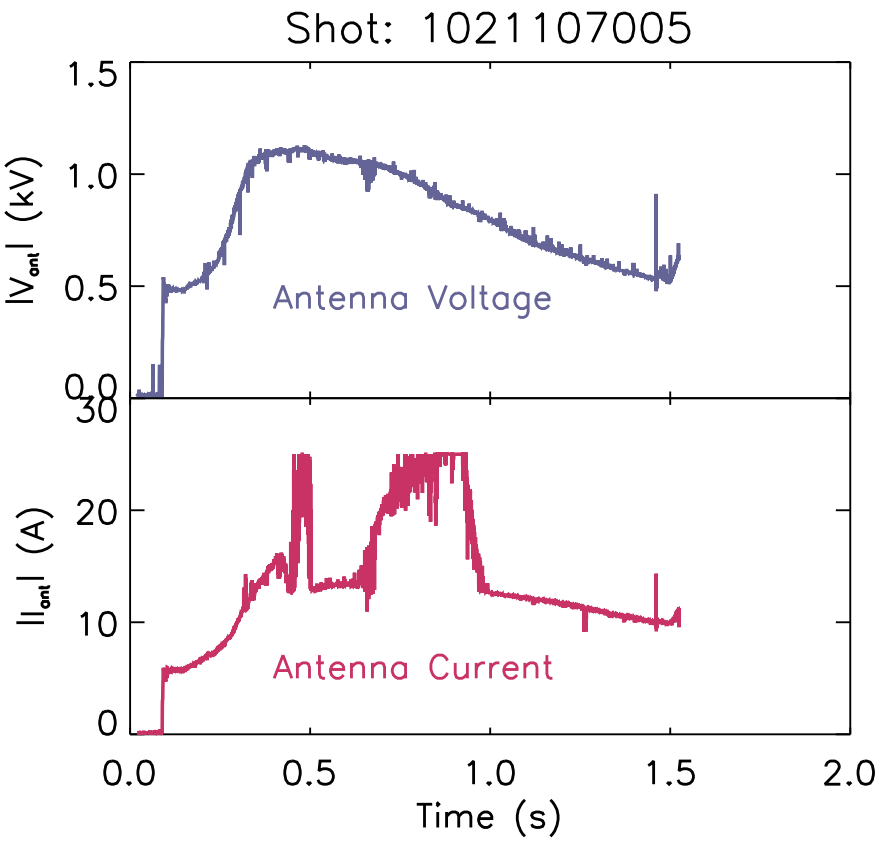

Figure 3-15: Diagnostics indicate that up to 25 A of current at >1 kV was driven by the MHD amplifier on 1021107

Active MHD diagnostic system to perform frequency sweeps within a broad range to actively track TAE modes in the plasma in real time, an application that is planned for future operation.

3.1.6 CAMAC Modules

At the lowest level of system operation are the CAMAC modules responsible for timing, triggering, and controlling the output frequency of the function generator. TDI commands issued either manually or specified by an operator in the Alcator C-Mod "MAGNETICS" tree control the use of these modules. The actual components reside in a standard CAMAC crate at the bottom of the Active MHD Data Acquisition and Control (DACC) rack in the cell. An MPB decoder receives an initialization com-

mand from the CAMAC server and sends a trigger on channel 0 to a 2-pin LEMO Jorway 221 timing module. The Jorway 221 module runs on a 1 MHz external clock and in turn triggers the ACQ16 and ACQ32 digitizers (see section 3.2.3) as well as a 3-pin LEMO BiRa 5910 waveform generator. The BiRa 5910 module transmits arbitrary waveforms specified (point-by-point) by the system operator to be transmitted to other system components. Channel 1 of the BiRa is a gate for the ENI AP400B amplifier: an output of 10 V is sent to the amplifier rear connector and represents a full output power of 400 W. Frequency sweeps are achieved by transmitting a time-varying waveform on channel 2 that modulates the frequency output of the function generator when connected to its VCO input. Assorted cables that were specially ordered complete the excitation side of the Active MHD Spectroscopy diagnostic by connecting all system components together.

3.2 Data Acquisition Side

Assuming that the excitation side of the Active MHD Spectroscopy system is effective at generating current in the antennas at the prescribed frequency, the data acquisition side is responsible for measuring both the plasma response and the electrical characteristics of the system itself. This data must then be stored in digital form at a high sampling rate for further analysis at a later time. These tasks are accomplished by magnetic fluctuation coils inside of the vacuum vessel, current and voltage monitors at the output of the power amplifier, and fast digitizers contained in the DACC.

3.2.1 Magnetic Fluctuation Coils

One of the simplest diagnostic methods performed on plasmas is the measurement of magnetic field perturbations at the plasma edge. Magnetic fluctuation coils, also known as magnetic pick-up coils, are universally employed to study these perturbations. This approach is based on Faraday's Law, which states that a magnetic field varying in time will induce a voltage in a loop of wire through which magnetic flux

passes, such that

$$V = NA\frac{\partial B}{\partial t}$$

where N is the number of loops and A is the cross-sectional area of each loop. The magnetic field perturbations at the coil location will have a defined frequency ω and phase φ so that B may be written as

$$B \propto \exp\left(i\omega t + \varphi\right)$$

and thus $V \propto NA\omega$. In actuality, there are magnetic perturbations in the plasma at many different frequencies so that the actual signal induced in the coil is the sum of the signals due to all time-varying fields. Bandpass filtering may be used to analyze plasma activity in a certain frequency range of interest.

In a toroidal confinement device such as a tokamak, the phase of each coil signal is dependent on the coil location in both the poloidal $\left(\hat{\theta}\right)$ and toroidal $\left(\hat{\phi}\right)$ planes. Because of the specific geometry, any wave must have an integral number of wavelengths in the poloidal and toroidal directions; that is, mode wavelength is quantized. Quantization allows the phase to be written as

$$\varphi = m\theta + n\phi$$

where m and n are the poloidal and toroidal mode numbers, respectively. It is therefore necessary to install magnetic fluctuation coils at various poloidal and toroidal locations to access information about the phase of the excited mode. Figure 3-16 below shows a poloidal cross-section of the Alcator C-Mod vacuum vessel and the locations of magnetic pick-up coils with similar values of toroidal angle ϕ.

The array of pick-up coils forming an arc on the outboard side of the machine has been placed underneath tiles forming the surface of an RF limiter. It is precisely these outboard limiter coils whose signals are used to study the excitation of TAE modes by the Active MHD Spectroscopy system. Furthermore, coils are located on two different limiters in the vessel, as illustrated in Figure 3-17 below showing locations of pick-up coils in a toroidal cross-section view. In the case of modes with medium to high n numbers, such as TAE's expected to be excited by the Active MHD antennas, pick-up

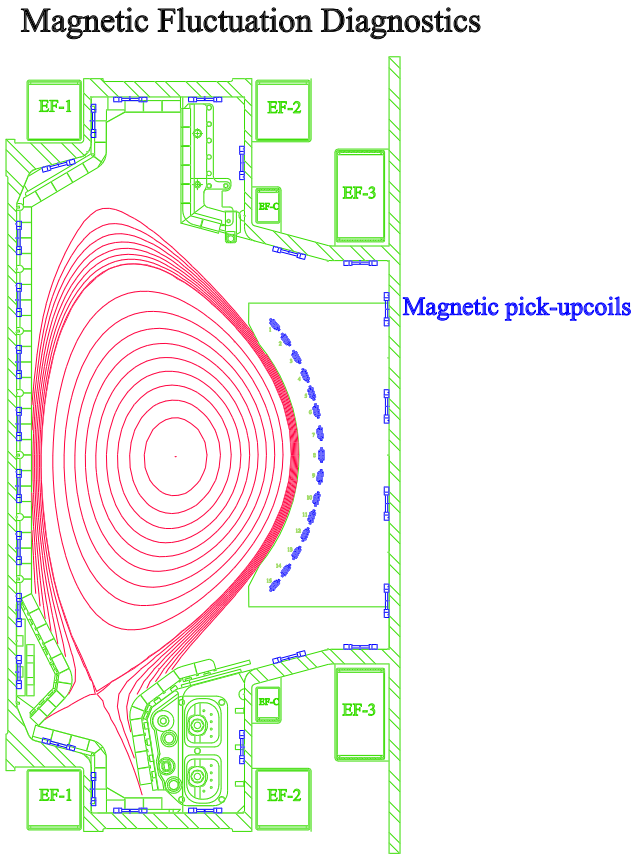

Figure 3-16: Location of magnetic fluctuation coils (in blue) spaced poloidally around the Alcator C-Mod vacuum vessel

coils spaced closely together in the toroidal direction are also required. A mode with $n = 20$, for example, has a toroidal wavelength of 28.6 cm at the plasma edge. It would be inaccurate to compare signals from coils located on the two different limiters in order to compute the toroidal mode number because the separation distance ($\sim$260 cm) is much greater than one wavelength. Fortunately, there are pick-up coils on both limiters at the same poloidal angle separated by only $\sim$4 cm for this exact purpose.

3.2.2 Current and Voltage Monitors

Measuring the current flowing in the antenna and the voltage across each antenna is also an important function of the data acquisition side of the Active MHD system. Located at the output of the impedance matching unit is a Pearson model 110 current

transformer. The transformer is disk-shaped so that a current-carrying wire may be passed through the center hole, and its output is a voltage signal that is directly proportional to the current flowing in the wire. A resistive voltage divider with a balun at its output is also attached to the output of the impedance matching unit by way of a type-N tee. Tests performed with the voltage divider indicate that the signal amplitude is attenuated by a factor of approximately 1400.

3.2.3 Digitizers

Central to the data acquisition side of the Active MHD system is the performance of signal digitization. Signals generated by the assorted pick-up coils and current and voltage monitors are carried via low-loss transmission lines to an adapter box at the top of the DACC rack. Cables run from the adapter box to a 2 pin LEMO patch panel and finally via ribbon cable to the two PCI-based digitizers located in an industrial computer crate. The digitizers are the ACQ16 and ACQ32 models manufactured by D-Tacq Solutions, Ltd.[2] The ACQ16 is a fast 16 channel, 14-bit digitizer with 128 MB of onboard system memory. For experimental studies of TAE modes, however, the ACQ16 is operated with only 12 channels at a maximum sampling rate of 2.5 MHz, providing adequate resolution for measurements of mode frequencies approaching $\sim$1 MHz. Slower digitization is provided by the ACQ32 board with 32 input channels for 16-bit sampling at 200 kHz. Low frequency signals such as the amplifier outputs specifying power output and maximum voltage condition are transmitted to the ACQ32 digitizer. All signals acquired and stored by active digitizer channels are represented in the C-Mod "MAGNETICS" tree under the ACTIVE_MHD node, SIGNALS sub node. Access to stored signal data in the C-Mod tree is then facilitated by the MDSplus software package developed at the PSFC.[3] In Chapter 4, the process of analyzing the data acquired during experimental studies employing the Active MHD Spectroscopy system will be explained in detail.

[2]D-Tacq website: http://www.data-acquisitions.co.uk
[3]MDSplus website: http://www.mdsplus.org/intro/index.shtml

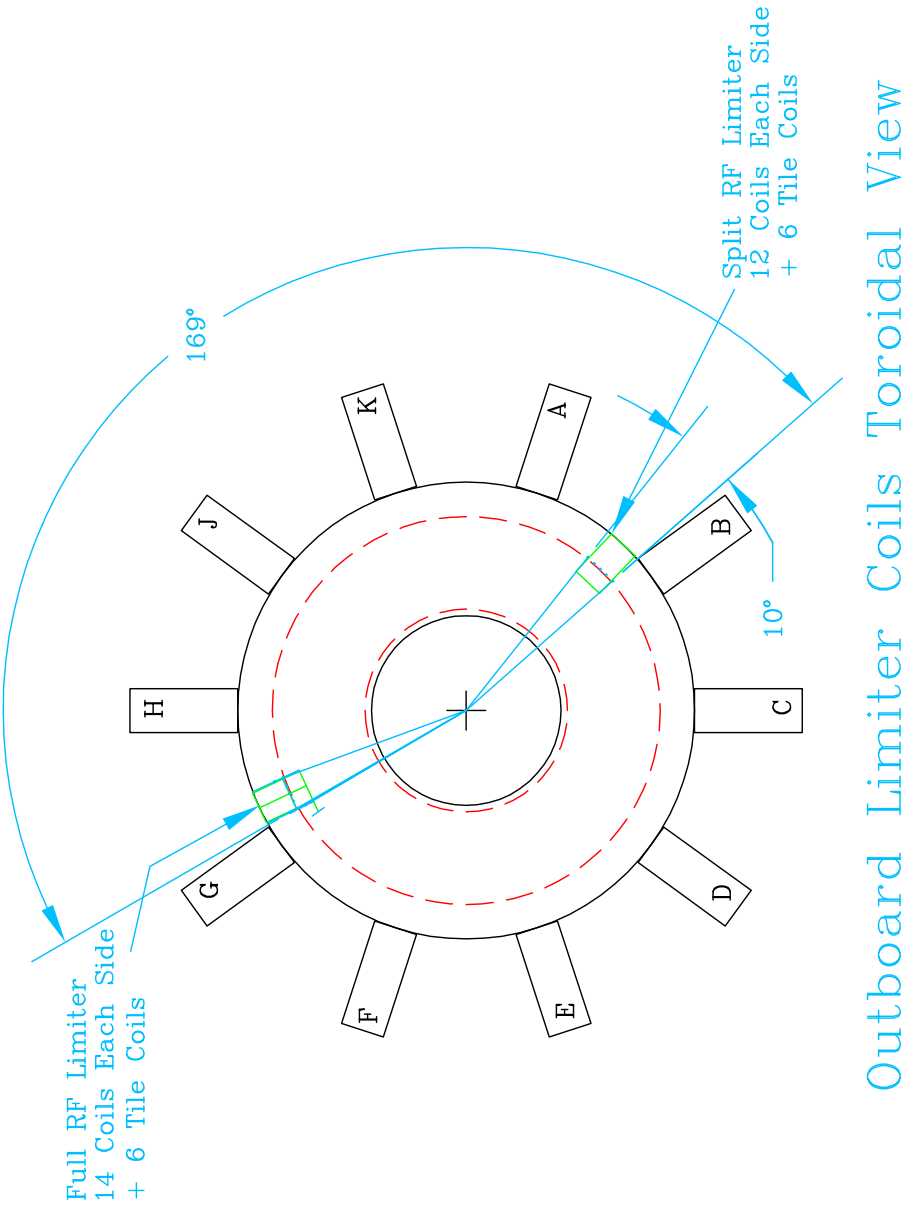

Figure 3-17: Location of magnetic fluctuation coils on the outboard limiters (in green) spaced toroidally around the Alcator C-Mod vacuum vessel

Chapter 4

Experimental Results

As outlined in Chapter 1 of this thesis, the excitation of global electromagnetic modes in a plasma, such as toroidal Alfvén eigenmodes, are of interest because of possible harmful interactions with fusion-born alpha particles in a burning plasma experiment. TAE's arising in a tokamak plasma (see section 2.3.2) were shown to have a negative effect on the fusion reaction rate if the modes are undamped and the amplitudes are allowed to grow in time. The total growth rate of a mode was given in section 2.3.2 as

$$\gamma = \gamma_{drive} - \sum \gamma_{damp}$$

where γ_{drive} is the unstable growth rate due to all driving mechanisms, such as the presence of a radial pressure gradient in the fast particle distribution. Measuring the damping rate of TAE's in the absence of fast particles, and hence any instability drive, yields an estimate of γ_{damp}. Uncovering the dependence of γ_{damp} on the physical aspects of a plasma- such as density, q profile, triangularity, and elongation- may allow plasma equilibrium to be tailored to maximize the damping rate and avoid possible harmful instabilities.

Experiments investigating active excitation of toroidal Alfvén eigenmodes were carried out for the first time during the Fall 2002 run campaign on Alcator C-Mod. These experiments had four main objectives: excite stable eigenmodes in the plasma, verify the dependence of the resonant frequency of these modes on magnetic field and

plasma density, calculate the damping rate, and determine the toroidal mode numbers of the excited modes. Exhaustive tests were conducted prior to initial operation to ensure minimal leakage of the transmitted Active MHD signal into the cell. Excess signal in the cell has the potential to disrupt other diagnostics, such as the neutron detectors and loop voltage measurements. Precise tuning of the impedance matching circuit was most important in minimizing leakage because of signal reflection due to load mismatch.

4.1 Experimental setup

One full C-Mod run day (1021003) was allocated to perform these initial TAE excitation experiments on ohmic plasmas, and "piggybacking" of the Active MHD system was conducted on one subsequent run day (1021107).

4.1.1 Run Day 1021003

The main goals of the experimental studies on 1021003 were to characterize the TAE modes excited by the Active MHD system and identify resonances in the complex transfer function in order to calculate the damping rate and toroidal mode numbers. Resonances in the pick-up coil signals are expected when the excitation frequency of the Active MHD system approaches a resonant TAE frequency in the plasma

$$f_{ActiveMHD} = f_{TAE}$$

As previously shown, the theoretical resonant frequency of a TAE mode depends as

$$f_{TAE} = C\frac{B_{tor}}{q\sqrt{n_e}}$$

where C is not radially dependent. This equation indicates that there is a resonant frequency at every radial location in the plasma since the above quantities are in general functions of the minor radius. Assuming that $q = 1.5$ corresponds to the most effectively driven TAE mode [27, 29, 30], resonances will occur when the condition

$$\frac{B_{tor}}{\sqrt{n_e}} = \frac{1.5 f_{ActiveMHD}}{C}$$

is met. Analysis is simplified by further assuming that

$$\frac{B_{tor}}{\sqrt{n_e}} \propto \frac{B_0}{\sqrt{\bar{n}_e}}$$

where B_0 is the toroidal field at the magnetic axis and $\bar{n}_e$ is the line-averaged electron density .

Over a series of limiter discharges, the toroidal field was scanned and electron density held constant while applying constant excitation frequency to the Active MHD antennas. By maintaining constant Active MHD frequency, any plasma resonance may be more easily observed than by sweeping the frequency with an unmatched circuit, where changes in the circuit response with frequency could mask a potentially small resonance. The pre-programmed target electron density was then shifted between shots to verify the dependence of the location in time of resonant peaks in the pick-up coil signals. Limited discharges with low triangularity and moderate elongation are desired in this experiment because these configurations were shown to have lower damping rates in the experimental studies on JET [28].

The parameters of the Active MHD system for a typical shot, such as 1021003012, are shown in Figure 4-1. Before operation of the Active MHD system into plasma, the matched frequency (discussed in section 3.1.3) was determined to be 420 kHz and the output of the function generator was set to a sine wave at this frequency. The ENI commercial model was used as the primary amplifier and has a forward output of nearly 400 W. Reverse power due to load mismatch is minimal at less than 10 W due to precise tuning of the impedance matching circuit. The voltage developed across the antenna by the amplifier is $\sim$700 V and the current driven in the antenna is nearly 18 A. The duration of system excitation was $\sim$1.8 s for each discharge.

Ramping of the toroidal magnetic field during each shot occurred during the time range when electron density was held relatively constant. An example, shot 1021003007, is shown in Figure 4-2. The toroidal field reached a maximum of 6 T and then decreased linearly until the discharge was terminated. The line-averaged electron density is constant at $\sim$1.8 $\times 10^{20}$ [m^{-3}]. In this way, the frequency of TAE modes in the plasma also decreases linearly in time and passes close to $f_{ActiveMHD}$ at

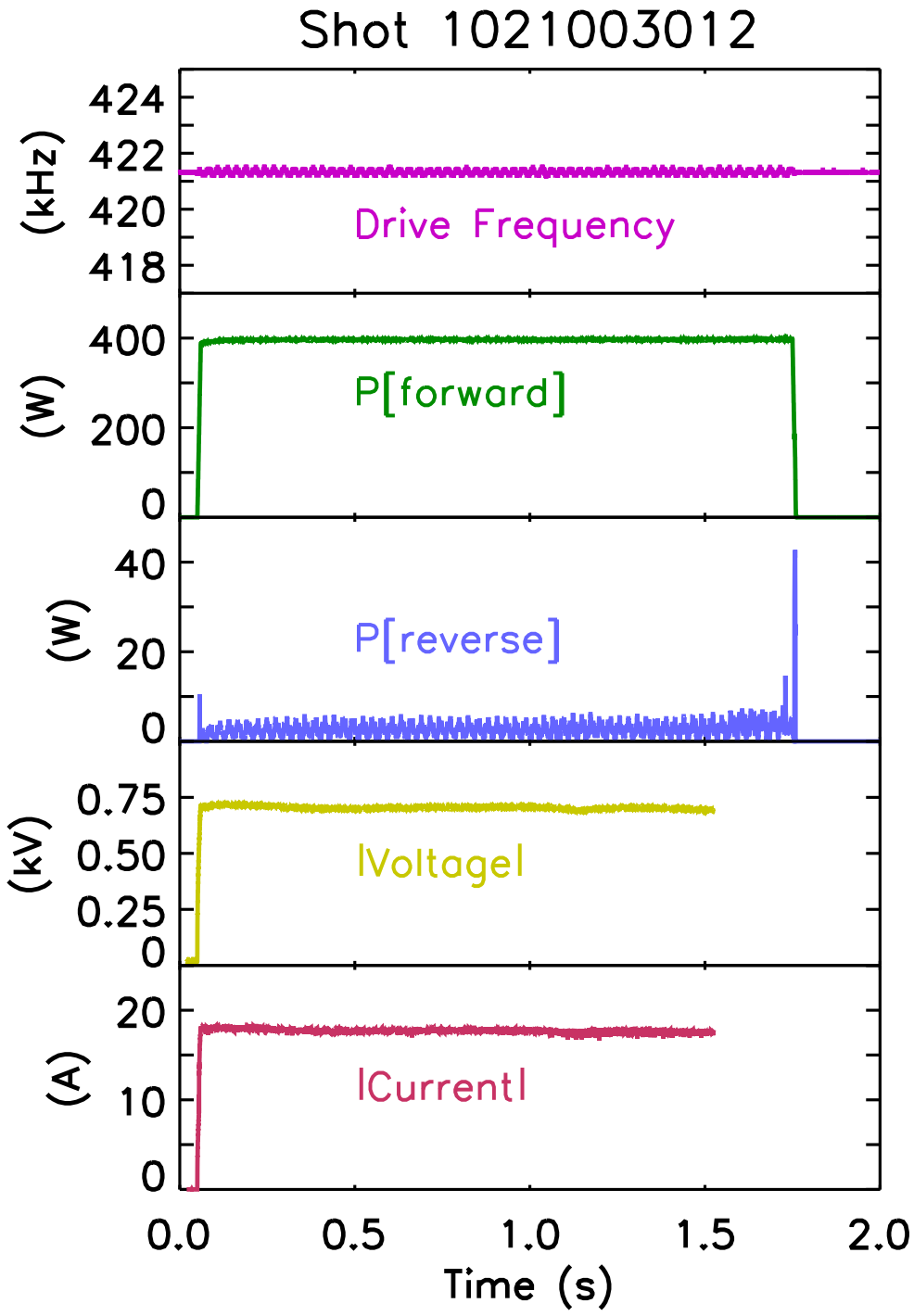

Figure 4-1: Typical parameters of the Active MHD Spectroscopy system on run day 1021003

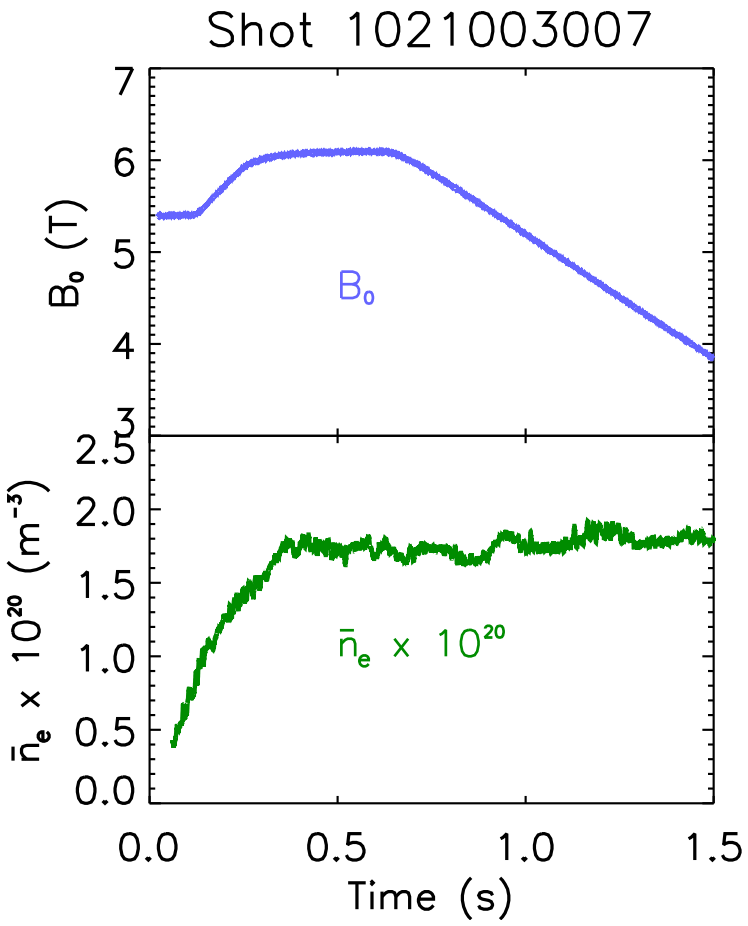

Figure 4-2: Variation of the toroidal magnetic field (top) and line-averaged electron density (bottom) during C-Mod discharge 1021003007

some time t_{res}. The location of t_{res}, and thus the peak in the pick-up coil signal, will vary between shots as the magnitude of the electron density is raised or lowered.

A few shots on this run day were dedicated to sweeping the frequency of the Active MHD system over the length of the discharge as opposed to maintaining constant fixed excitation frequency. This method is, unfortunately, inherently limited by the extremely small range of frequencies at which the tuning circuitry sufficiently "matches" the output impedance of the ENI amplifier to the complex impedance of the Active MHD antennas. Attempting to excite the system beyond the capability of the matching circuitry to tune the system would have resulted in a large amount of reflected power in the transmission line. Frequency sweeps were therefore limited to ± 10 kHz from the pre-determined matched frequency of 420 kHz.

4.1.2 Run Day 1021107

Additional "piggybacking" studies with the Active MHD Spectroscopy system took place on run day 1021107 with much the same goal as discussed in the previous section: identify possible mode resonances on multiple pick-up coil signals. The new MHD amplifier was employed for the first time and performed well during all system excitations. As discussed in section 3.1.4, impedance matching is simplified because no matching is required in the low frequency range (1 - 10 kHz) and only a single matching capacitor at higher frequencies (.3 - 1 MHz).

A total of eight shots were run with constant Active MHD excitation frequency throughout the discharge, but 29 shots were programmed with sweeping to vary the excitation frequency of the system over the length of the discharge. The toroidal magnetic field remained constant for all discharges, but the line-averaged electron density varied considerably (especially during discharges with one or more H-modes). The theoretical TAE frequency at a particular resonant surface will hence not vary linearly (as seen in shots on 1021003) but rather in a more complicated way.

4.2 Measurements

A total of 23 plasmas were obtained on run day 1021003, of which 11 showed clear resonance peaks in at least one pick-up coil signal. A resonance peak in this data is identified by taking an FFT of the pick-up coil signal between 418 and 422 kHz over nearly the full length of the discharge. The magnitudes of the various frequency components are then plotted in time and a discernible peak may be seen. In addition, the magnitude of the 420 kHz frequency component in the signal is also plotted for clarity. Invariably, the pick-up coil with the best signal response was BP03_ABK, located on the AB limiter on the other side of the machine from the Active MHD antennas. The signal from BP03_ABK for a reference plasma without Active MHD excitation, shot 1021003001, is shown in Figure 4-3.

No coherent activity in this frequency range is observed when the Active MHD system is switched off. However, this illustration is in marked contrast with that

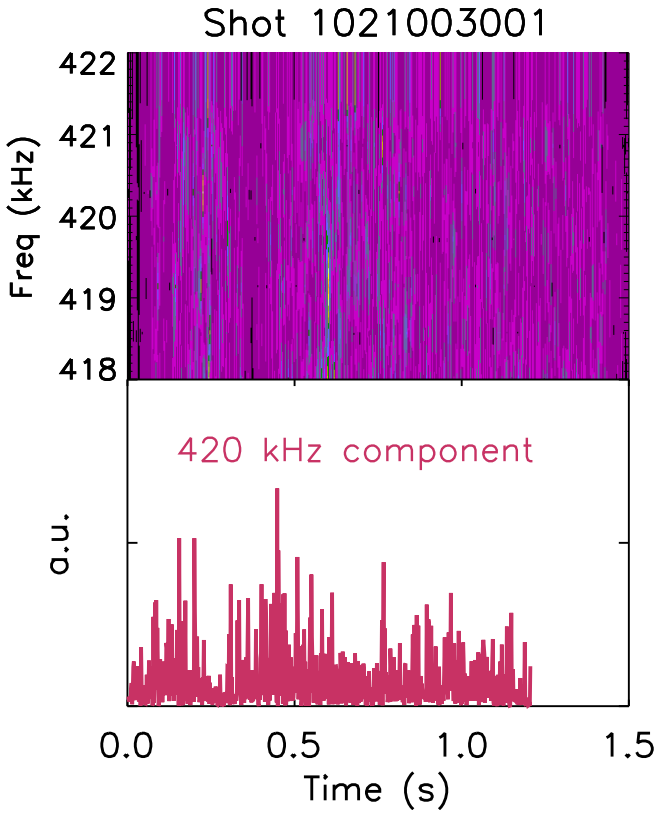

Figure 4-3: FFT spectrogram for reference shot 1021003001 with no Active MHD excitation

obtained when the Active MHD system is switched on, as in shot 1021003012. The system is functioning at full power and the plasma is driven at 420 kHz, producing the spectrogram in Figure 4-4. Coherent activity in the frequency range 418 - 422 kHz is now observed in the FFT spectrogram, and specifically nearly at 420 kHz. A resonance peak, represented by the maximum signal amplitude in this frequency component and also much higher than the background signal level, is clearly seen at 1.12 s into the discharge. Maximum signal amplitude should occur when the frequency of the excited TAE mode is close to 420 kHz. This supposition is verified in Figure 4-5, which shows that the intersection of the theoretical TAE frequency at the $q = 1.5$ surface and the Active MHD excitation frequency occurs close to 1.12 s.

As the electron density is varied between shots, this resonance peak should be observed at different times in the spectrogram. Figure 4-6 and Figure 4-7 show the spectrograms of BP03_ABK for each shot in which a resonance peak was seen.

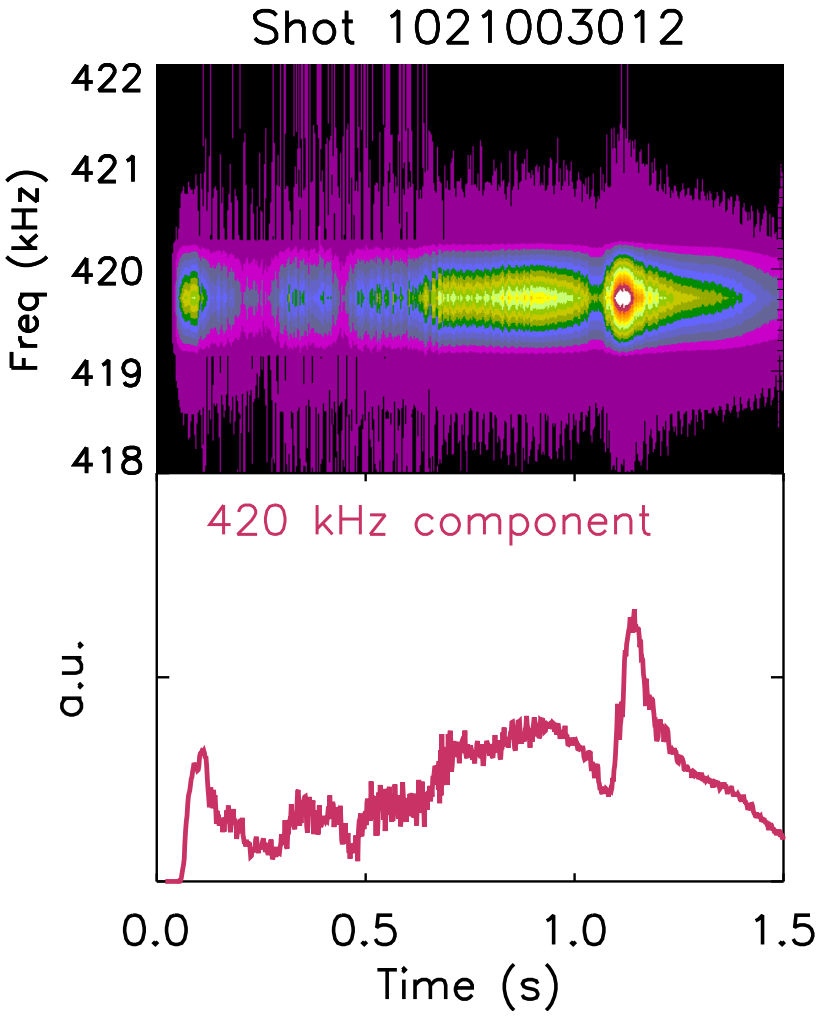

Figure 4-4: FFT spectrogram of BP03_ABK signal for shot 1021003012 with Active MHD system operating at full power (400 W)

Spectrograms of coils other than BP03_ABK produced in this manner, however, do not exhibit the same large peaks in the FFT spectrogram close to 420 kHz. There seems to be a lower level of signal compared to ambient noise level, so clear peaks that may be buried underneath are not visible in the FFT spectrogram. The reason for this phenomenon is unclear. Consider the spectrogram from coil BP6T_GHK in Figure 4-8 as a typical example.

The values of $\bar{n_e}$ and B_{tor} at the resonance time described above are also calculated to verify the dependence of t_{res} on the theoretical TAE frequency. Assuming that the mode is excited at the same q surface for each shot, the magnitude of the toroidal field at t_{res} should depend on $n_e^{1/2}$ when plotted against the electron density, according

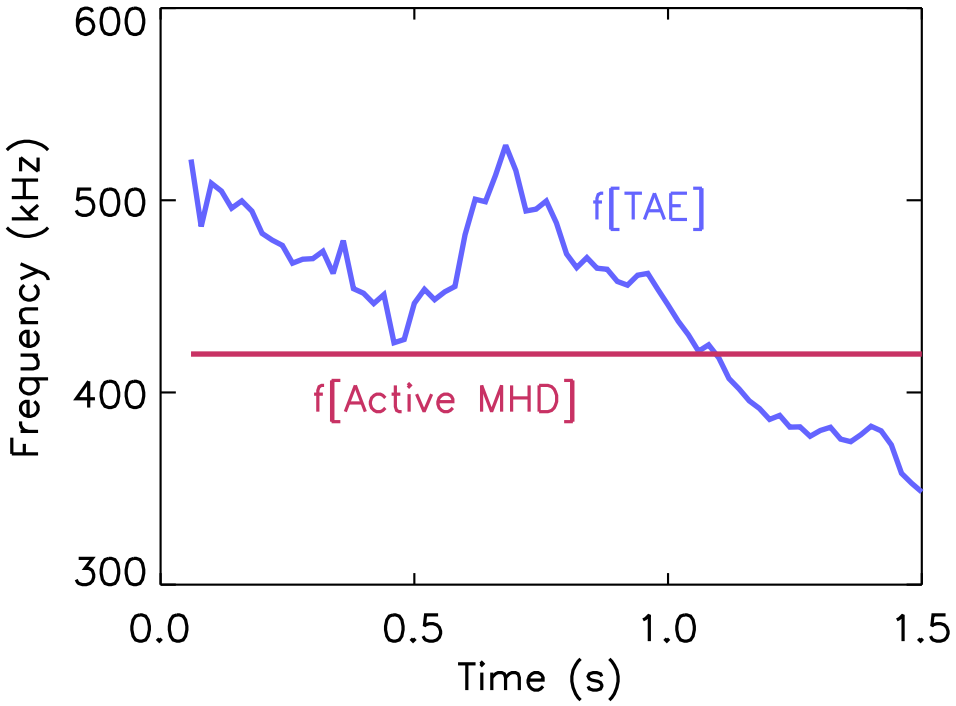

Figure 4-5: The theoretical TAE frequency for shot 1021003012 as a function of time at the $q = 1.5$ surface decreases through $f_{ActiveMHD}$ near 1.12 s

to the formula for TAE frequency (see Section 4.1.1). This is graphed in Figure 4-9 along with a least-squares fit to the data of the form $B = \alpha n_e^{1/2}$ where α is a constant. The data in Figure 4-9 show clearly that the excited modes are Alfvénic in nature, and are most certainly TAE modes. Other Alfvén eigenmodes may have frequencies

$$f = N f_{TAE}$$

where $N = 2$ (elliptically-induced Alfvén eigenmodes), 3 (non-circular Alfvén eigenmodes), etc. However, theoretical TAE frequencies as low as 420/2 or 420/3 kHz are not possible with the prescribed values of the toroidal magnetic field and line-averaged electron density.

It is possible to estimate the damping rate of the excited mode from this data alone by substituting the theoretical TAE frequency for the time base and calculating the width of the resonance peak compared to the center (resonant) frequency. Unfortunately, estimates obtained in this way will have large uncertainties because

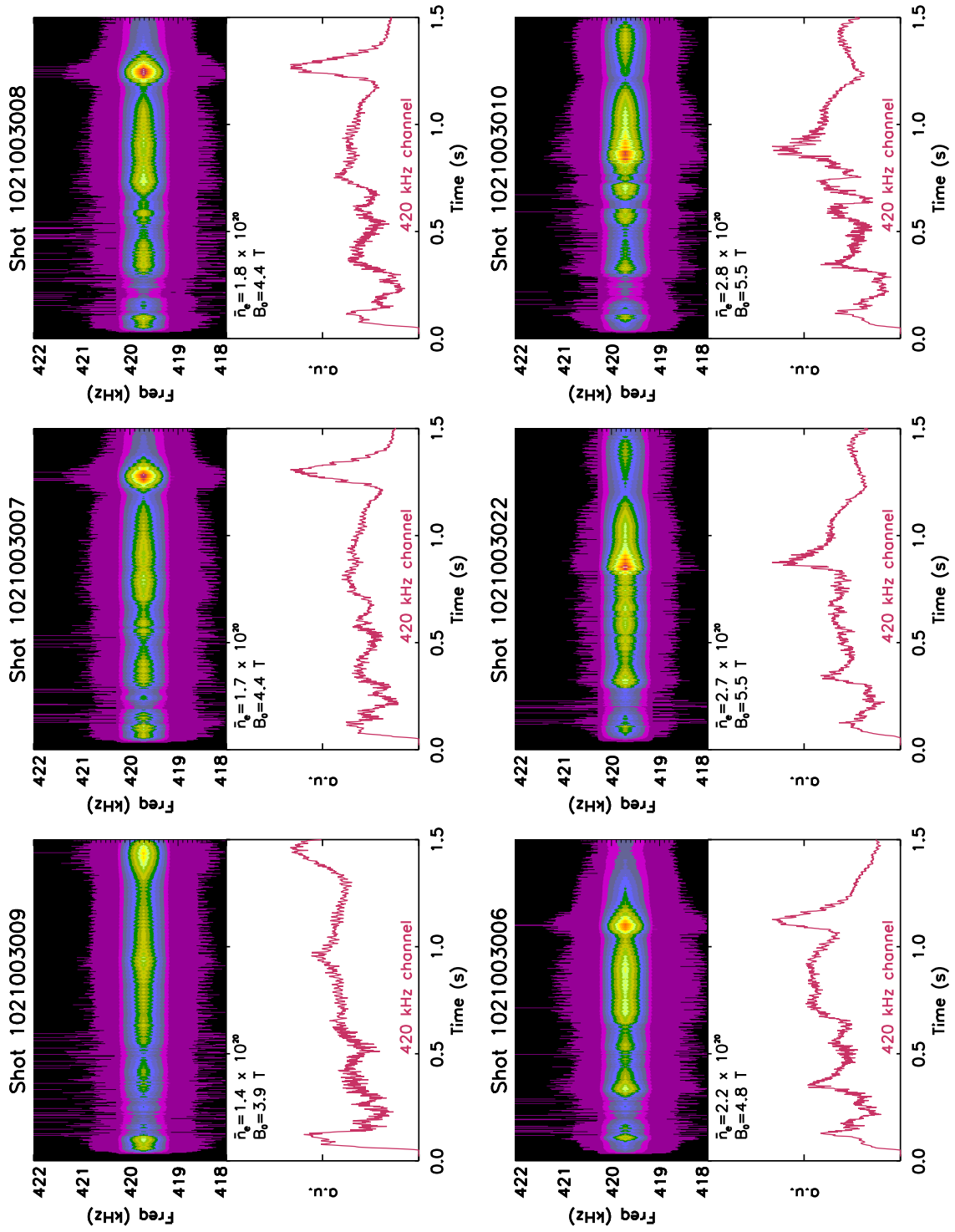

Figure 4-6: FFT spectrogram for all shots on run day 1021003 with discernible resonance peaks (1)

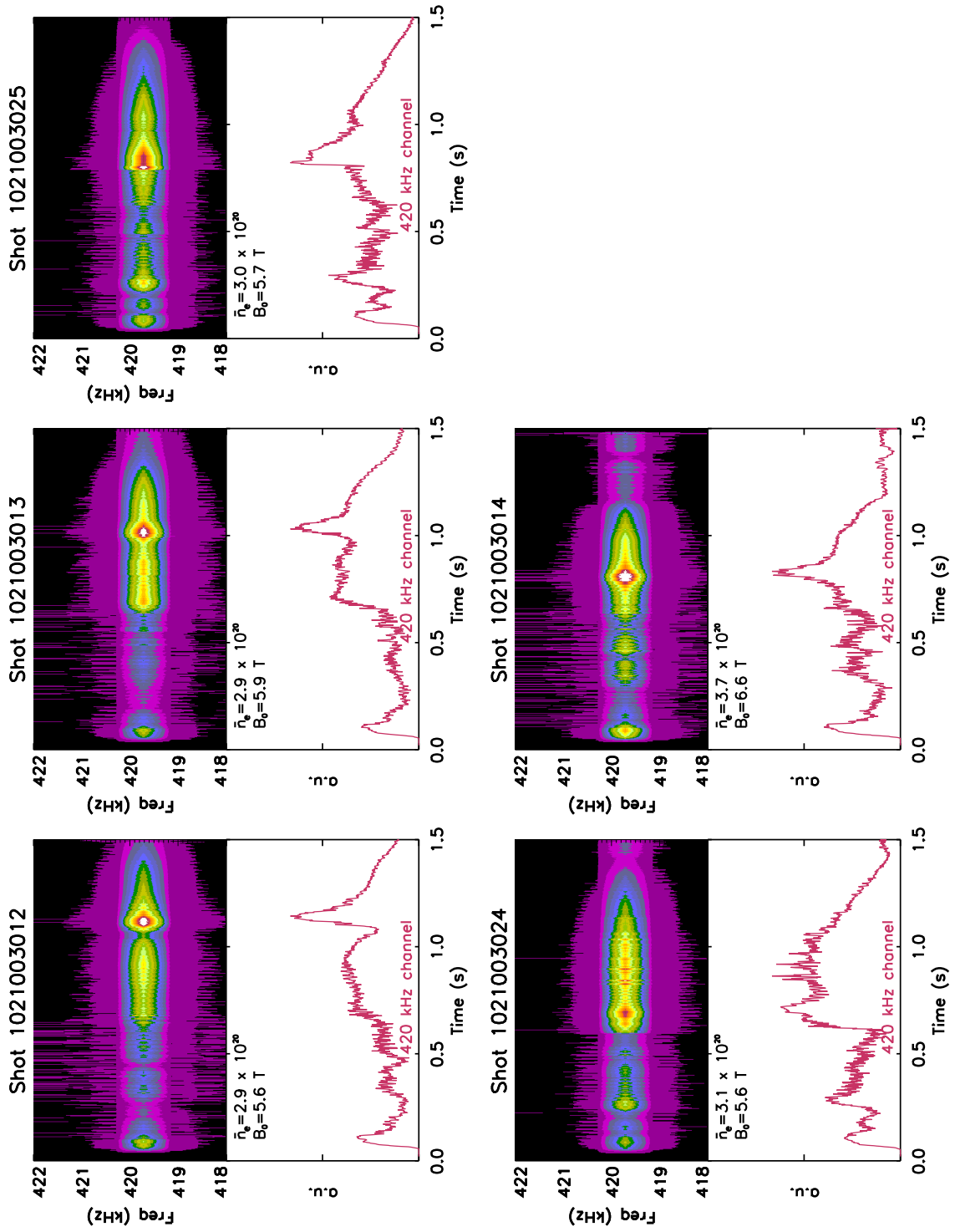

Figure 4-7: FFT spectrogram for all shots on run day 1021003 with discernible resonance peaks (2)

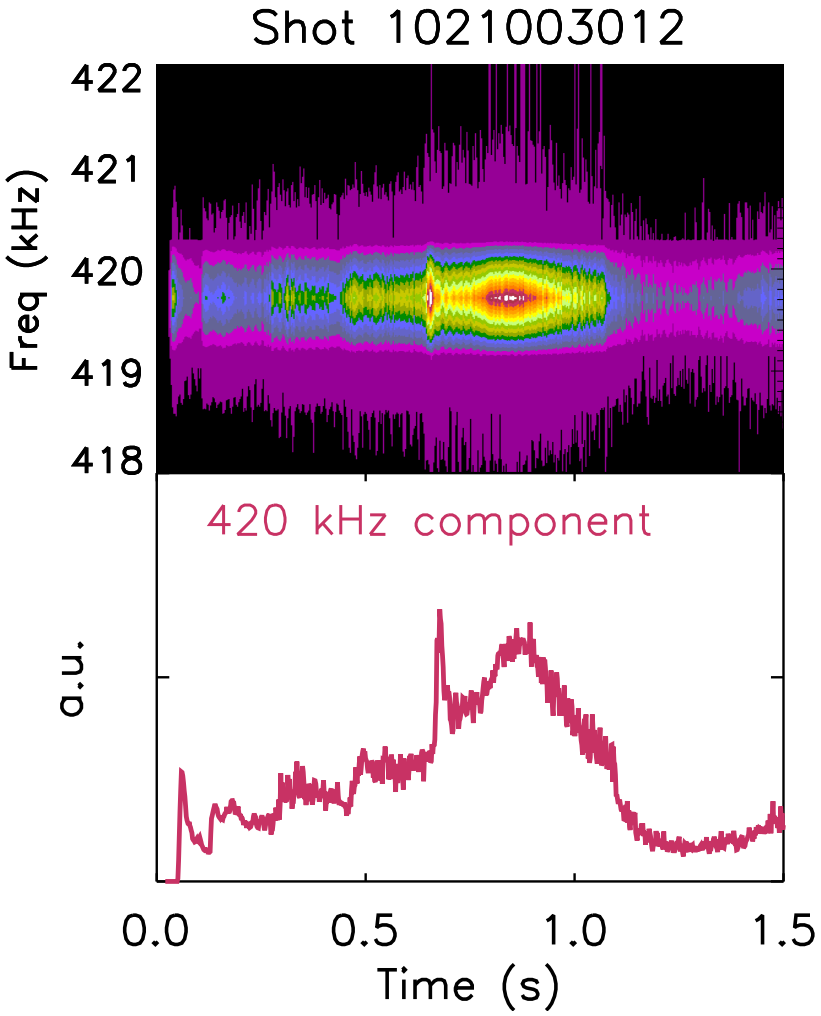

Figure 4-8: FFT spectrogram of BP6T_ABK signal for shot 1021003007 illustrating effect of low-level signal compared to BP03_ABK (see Figure 4-4)

data from only one pick-up coil (BP03_ABK) may be utilized. As shown in Figure 4-8, the FFT's of other coils do not clearly show the resonance peak seen on BP03_ABK. It is much more desirable from a statistical perspective, however, to use data from several pick-up coils simultaneously to deduce the damping rate and toroidal mode number.

4.2.1 Synchronous detection

Synchronous detection of the complex transfer function is therefore a better approach for further analysis of these signals. Rather than relying on data being present in the

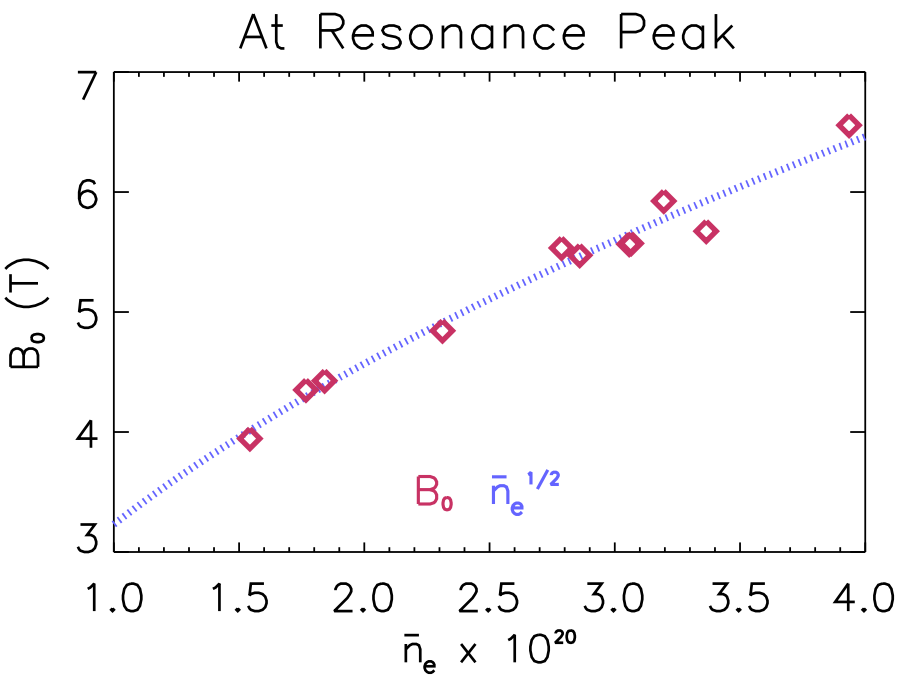

Figure 4-9: Value of the toroidal magnetic field plotted against the line-averaged electron density at the time of maximum signal amplitude (t_{res}) in the 420 kHz channel of the FFT spectrogram

raw FFT of the pick-up coil signal, synchronous detection offers a different way to uncover the resonance peaks produced by resonant TAE excitation. The method of digital synchronous detection using the software suite MATLAB is presented in Figure 4-10 and detailed as follows.

There are three signals of interest in the case of Active MHD excitation and pick-up: current flowing in the antenna, I_ant; voltage across the antenna as the reference signal, REF; and voltage on a magnetic pick-up coil, V_Bdot, which is proportional to $\dot{B}_\theta$ in the plasma. These signals are all acquired at high frequency (~2.5 MHz) using the ACQ16 digitizer and are on the same time base, t_ACQ16. The voltage signal from the pick-up coil is then filtered in the frequency range of interest using a digital Butterworth filter of order 10. Butterworth filters have the advantageous characteristic of giving maximally flat response in the pass band. Since the Active MHD system for these shots was held at a constant excitation frequency of 420 kHz,

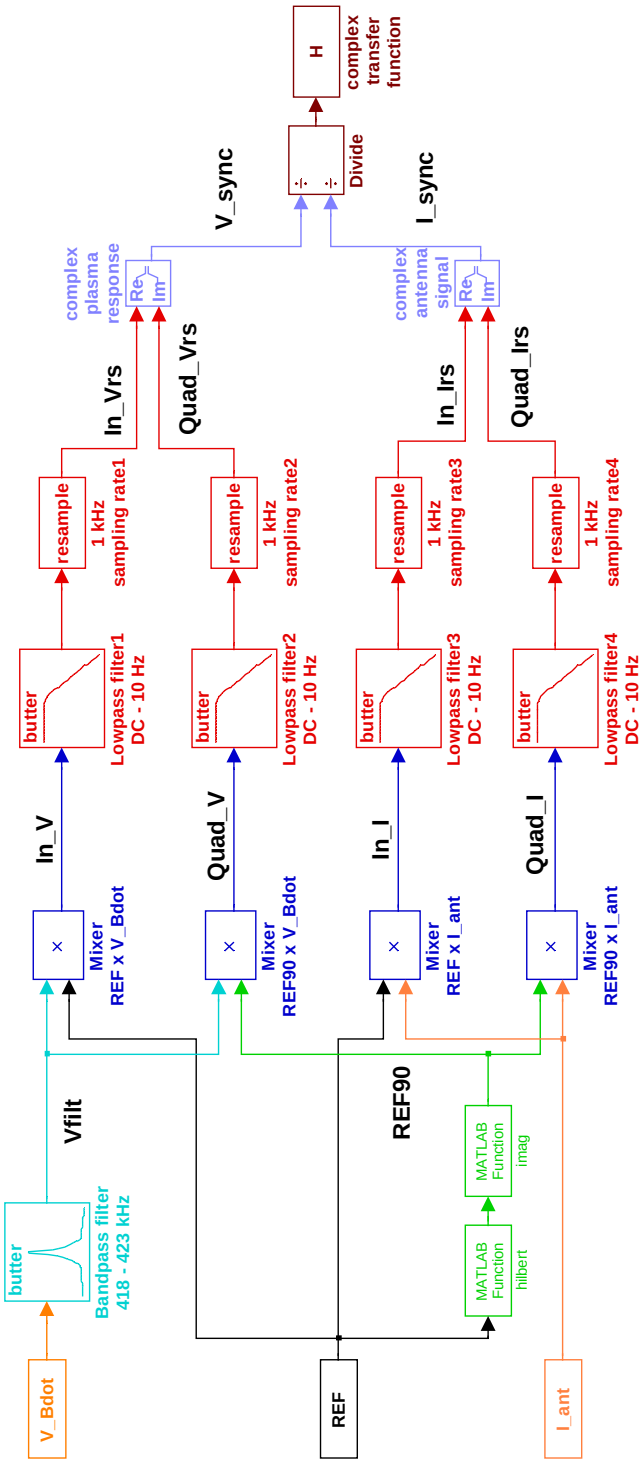

Figure 4-10: Schematic illustration of the synchronous detection algorithm written in MATLAB for analysis of pick-up coil signals

this pass band range is taken to be as narrow as possible to filter out noise and other fluctuations. A pass band of 418 - 423 kHz was chosen to eliminate all signal but that associated with TAE excitation, which includes the background coupling of the antennas themselves.

Next, a new signal called $REF90$ is created exactly 90° out of phase with REF using the HILBERT function. A digital mixer is then employed to determine the in-phase and quadrature components of both the pick-up coil signal and the antenna current. When two oscillating signals with the same frequency but different phases are multiplied together, as in the case of the digital mixer, the output will be a signal of the form

$$\sin(\omega_0 t + \varphi_1)\sin(\omega_0 t + \varphi_2) = \frac{1}{2}\left[\cos(\varphi_1 - \varphi_2) - \cos(2\omega_0 t + \varphi_1 + \varphi_2)\right]$$

which has a DC component and a high frequency component at twice the original frequency. Synchronous detection is concerned with only the DC component, so a low-pass digital Butterworth filter of order 3 is invoked to filter out all but the lowest frequency components. The cut-off frequency of this low-pass filter was chosen to be approximately 10 Hz. Four signals are obtained, each resampled at 1 kHz to reduce the size of the arrays. The synchronously detected pick-up coil signal is then simply

$$V\_sync = In\_Vrs + i * Quad\_Vrs$$

while the synchronously detected antenna current is given by

$$I\_sync = In\_Irs + i * Quad\_Irs$$

Finally, the synchronously detected, complex transfer function is then the ratio of these two signals

$$H = \frac{V\_sync}{I\_sync}$$

Synchronously detected complex transfer functions- using coil BP03_ABK for consistency- for all shots on 1021003 are presented in Figures 4-11 and 4-12, showing both real and imaginary parts. Because the frequency of the Active MHD system is fixed, output of the synchronous detection routine is actually H as a function of time.

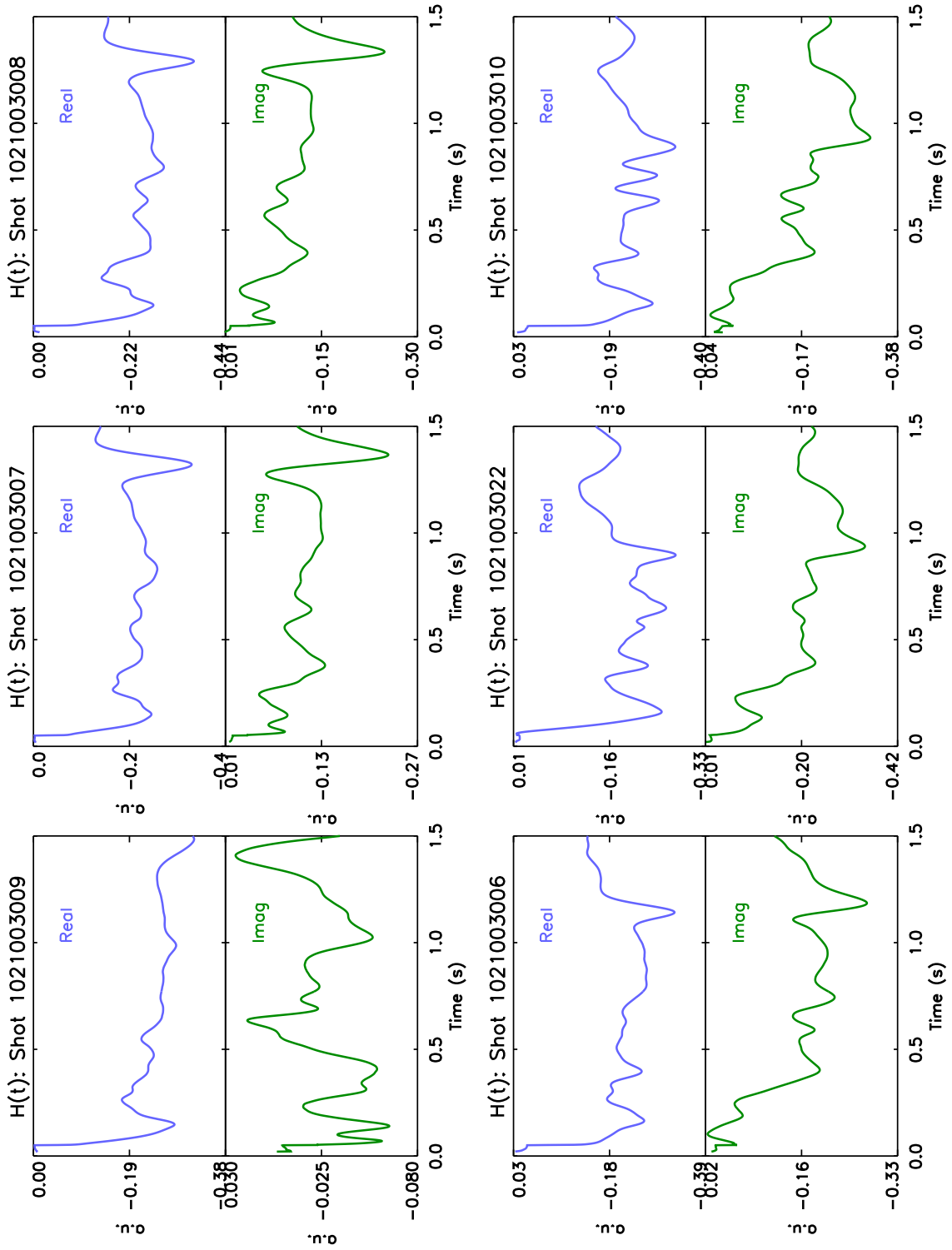

Figure 4-11: Synchronously detected signals for all shots on run day 1021003 (1)

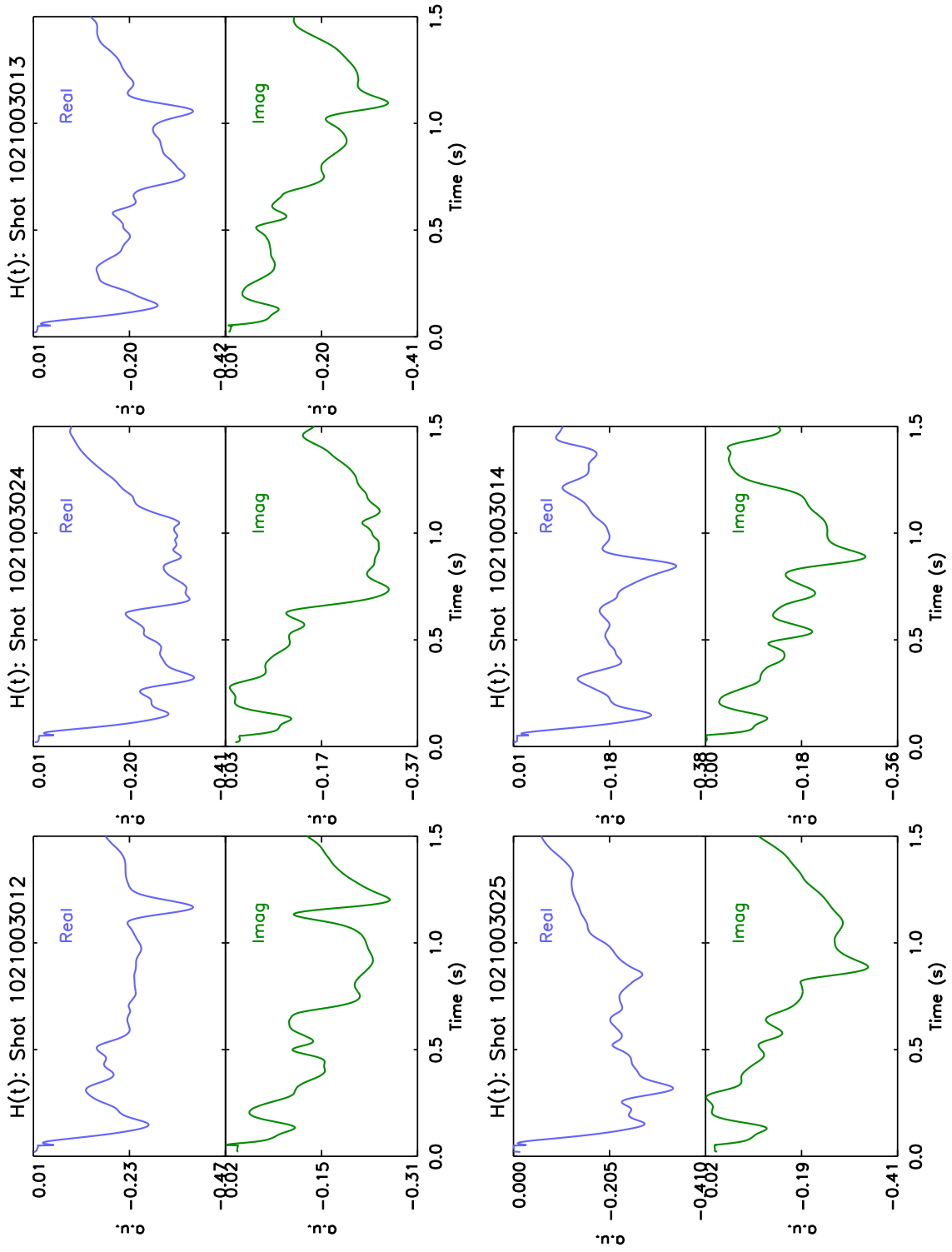

Figure 4-12: Synchronously detected signals for all shots on run day 1021003 (2)

However, as opposed to the previous approach using merely the FFT of the pick-up coil signal, synchronous detection reveals sharp fluctuations in the output at similar times on almost all magnetic pick-up coils. Consider, as a typical example, shot 1021003012, where the resonance is exhibited prominently by synchronous detection on most of the coils, not only BP03_ABK. This data is exhibited in Figures 4-13, 4-14, and 4-15.

Synchronous detection is a more robust and statistically preferable method for analyzing the data from multiple pick-up coil signals. Furthermore, a resonance is easily detected by observing where the transfer function turns in the complex plane and forms a circular shape. The resonances are distinguished on each shot by examining the synchronously detected signal from BP03_ABK around the expected resonance time and plotting the imaginary component of the signal against the real part. An iterative approach was employed until the circular shape in the complex plane was more or less observed, and the results of this analysis are shown in Figures 4-16, 4-17, 4-18, and 4-19. Clearly, shapes with varying degrees of circularness are observed on every shot except perhaps for 1021003024. For shot 1021003009, the target electron density was low enough (7.5×10^{19}) such that the TAE resonant frequency occurred very late in the discharge (close to 1.5 s). Data is not available for times exceeding 1.48 s, so half of a resonance in the form of a half circle is observed instead.

As previously shown, resonances are seen on almost all the active pick-up coils, not just BP03_ABK, using the synchronous detection algorithm. The synchronously detected signals from all eight active coils are shown in Figures 4-20, 4-21, and 4-22 for shot 1021003012 using the same frequency range as the one optimized for coil BP03_ABK above. Approximate circular shapes are clearly observed on every coil except for BP15_ABK, indicating a high level of signal coherence. There is a high probability, moreover, that coil BP15_ABK may not have been functioning properly during the experimental studies. A refined estimate of damping rates that minimizes statistical errors should now be possible because multiple coils may be analyzed simultaneously for a single discharge.

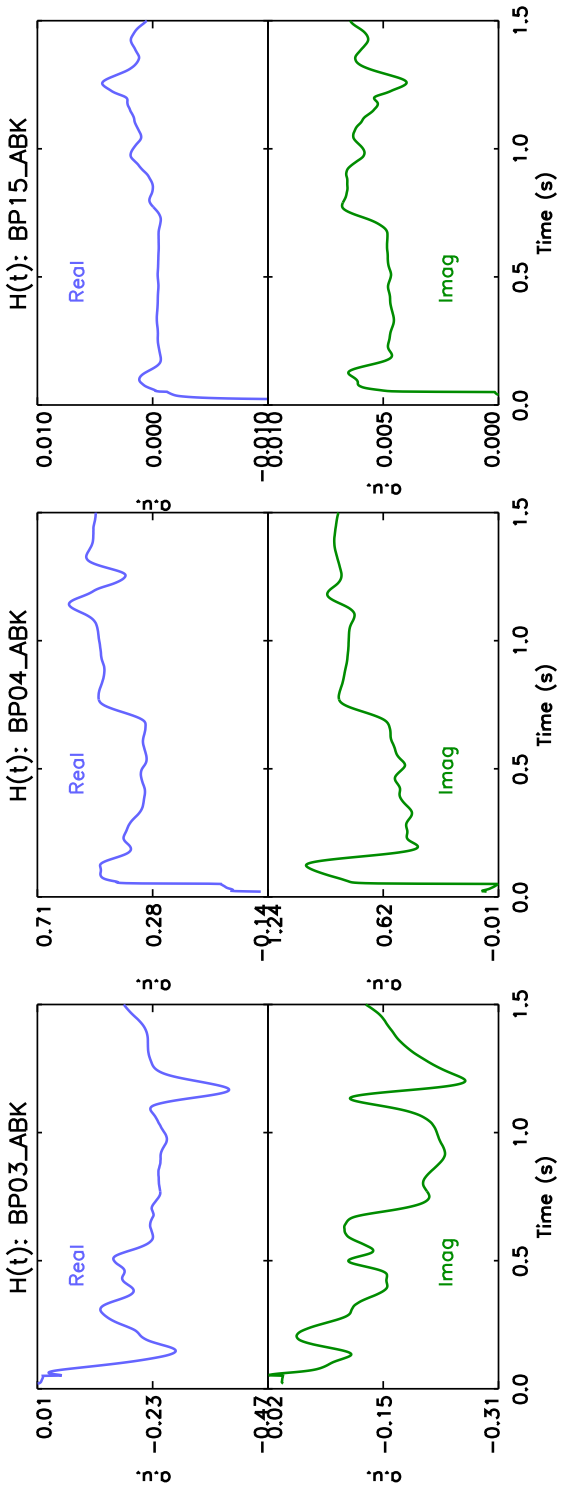

Figure 4-13: Synchronously detected signals for all coils on shot 1021003012 (1)

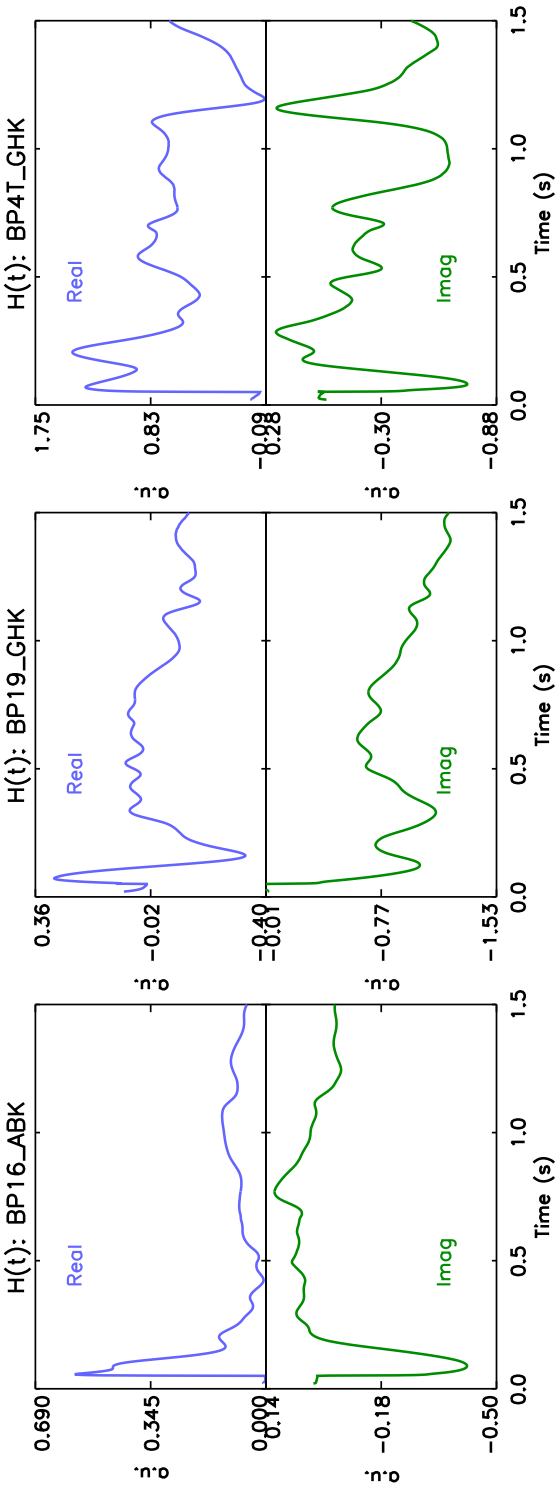

Figure 4-14: Synchronously detected signals for all coils on shot 1021003012 (2)

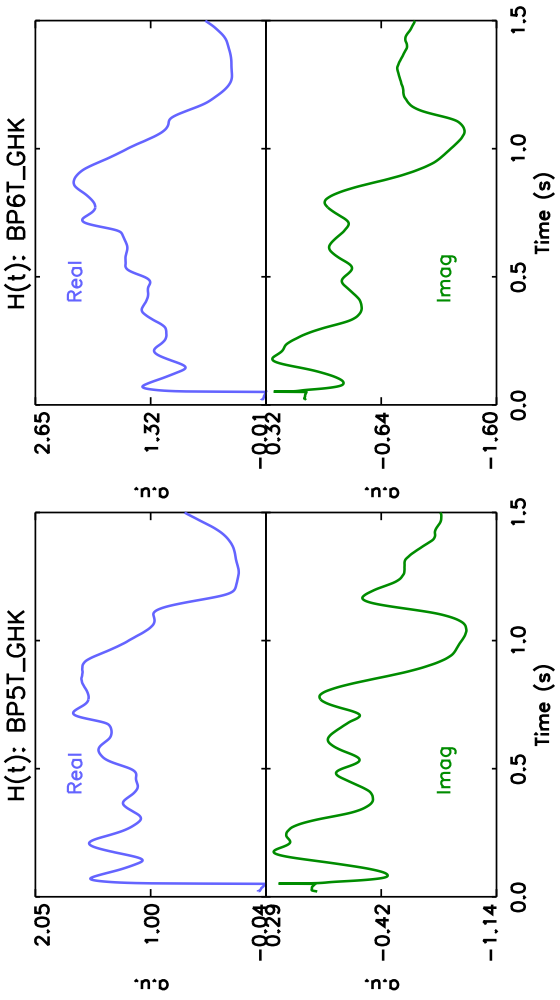

Figure 4-15: Synchronously detected signals for all coils on shot 1021003012 (3)

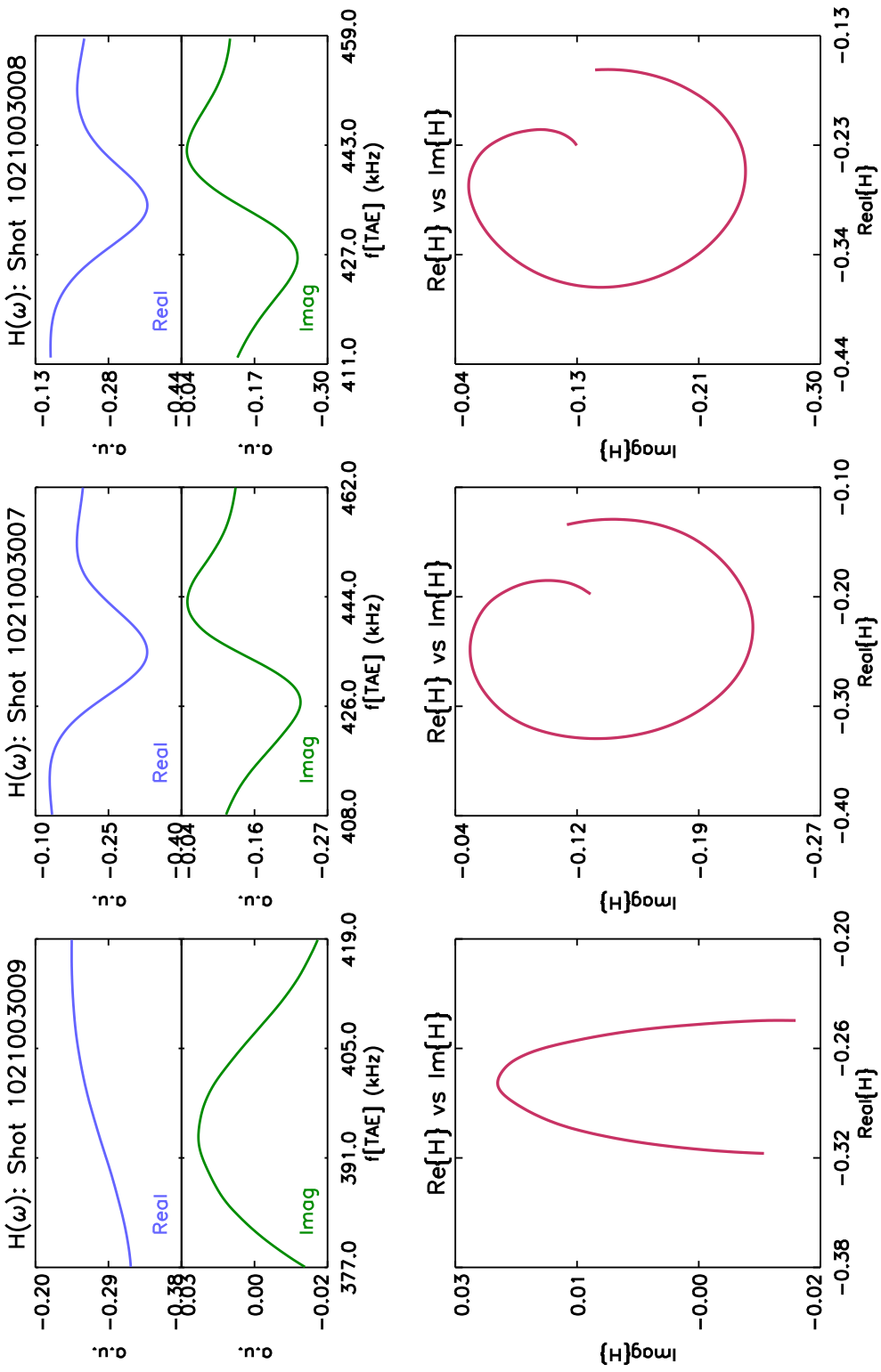

Figure 4-16: Synchronously detected signals for all shots on run day 1021003 depicting the "turning" of the transfer function in the complex plane (1)

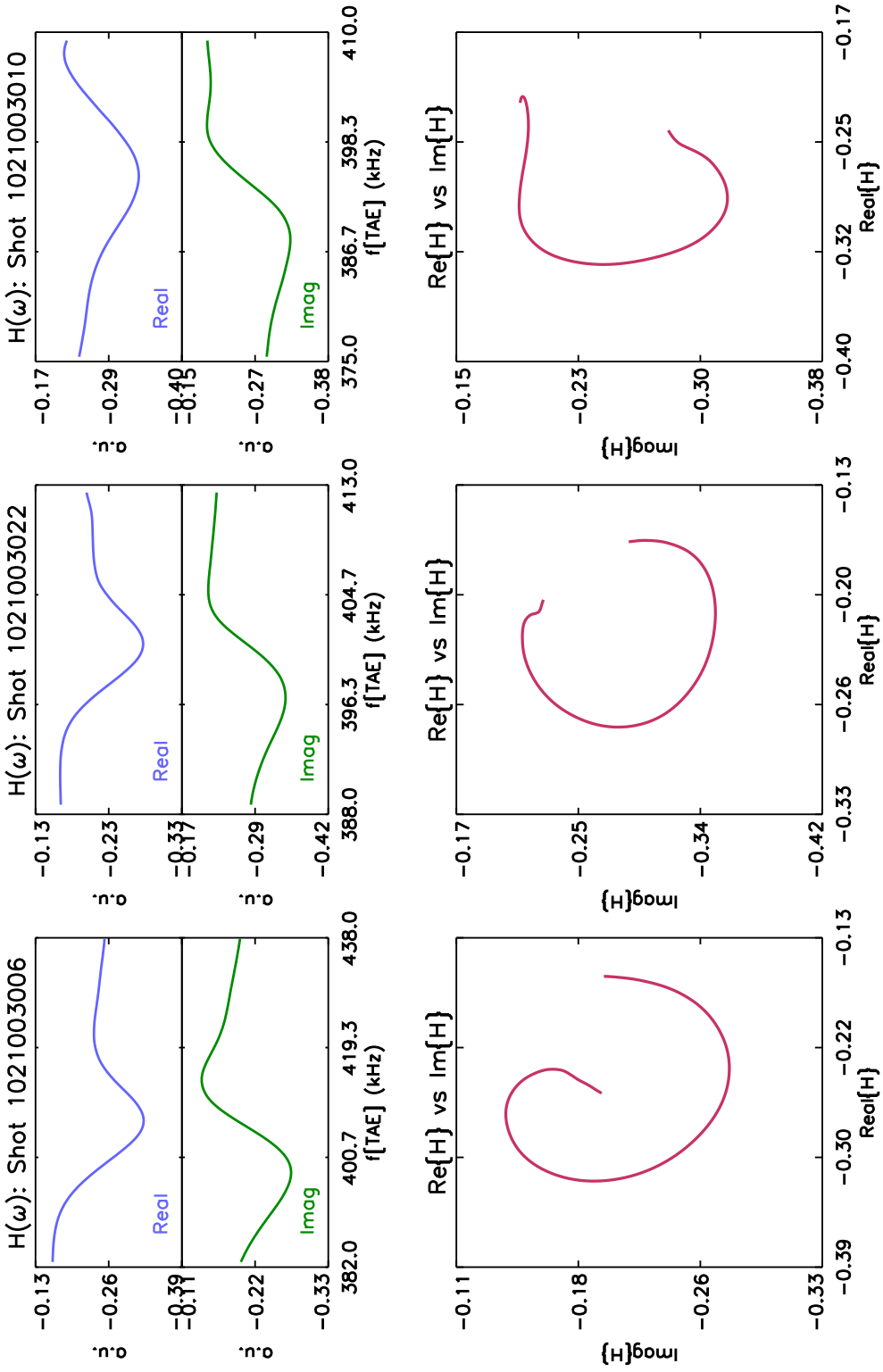

Figure 4-17: Synchronously detected signals for all shots on run day 1021003 depicting the "turning" of the transfer function in the complex plane (2)

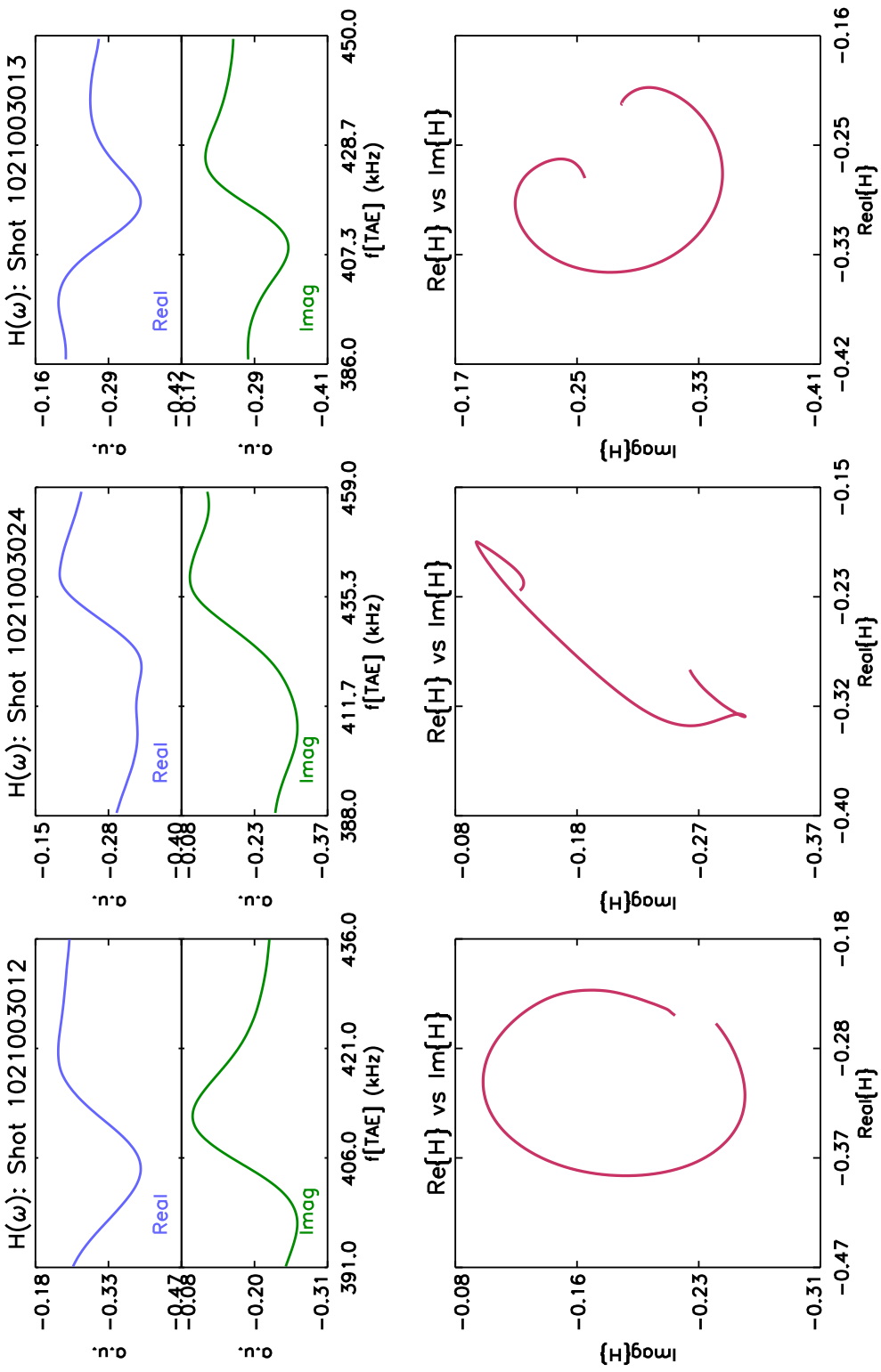

Figure 4-18: Synchronously detected signals for all shots on run day 1021003 depicting the "turning" of the transfer function in the complex plane (3)

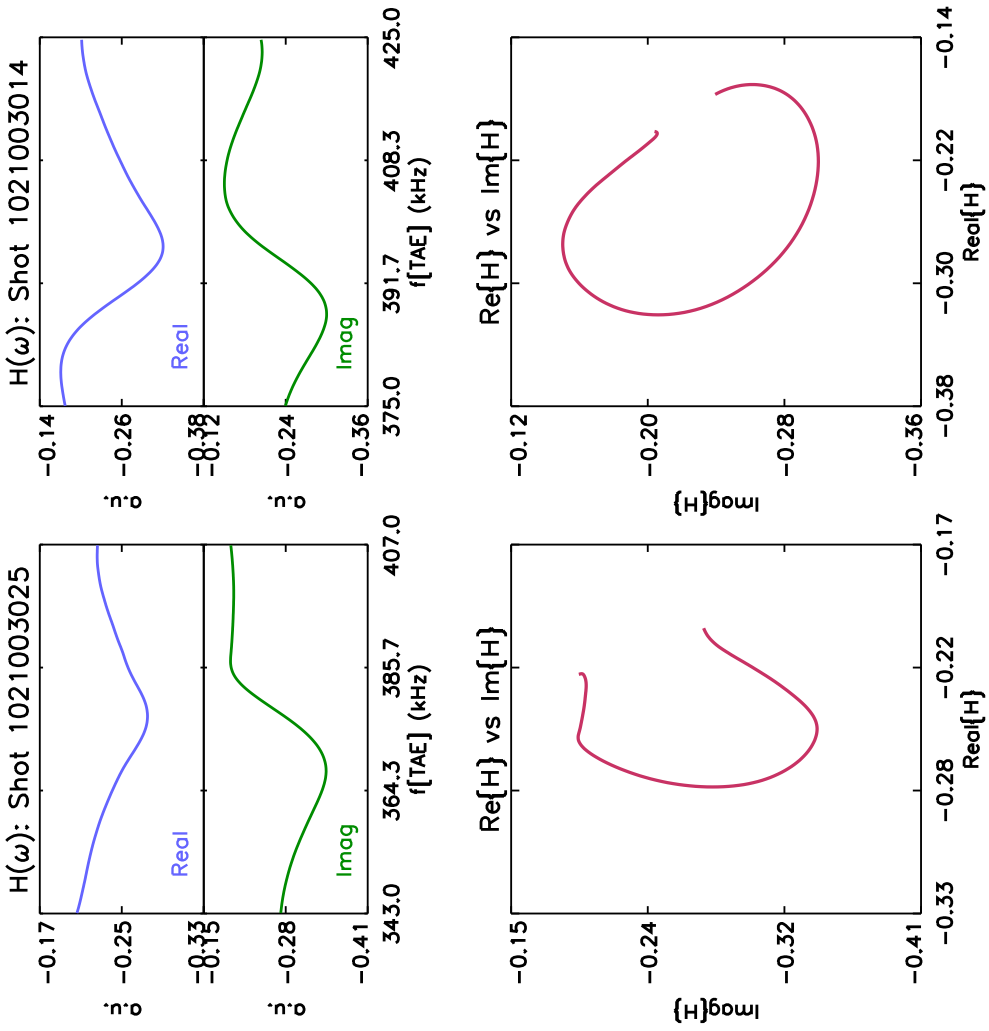

Figure 4-19: Synchronously detected signals for all shots on run day 1021003 depicting the "turning" of the transfer function in the complex plane (4)

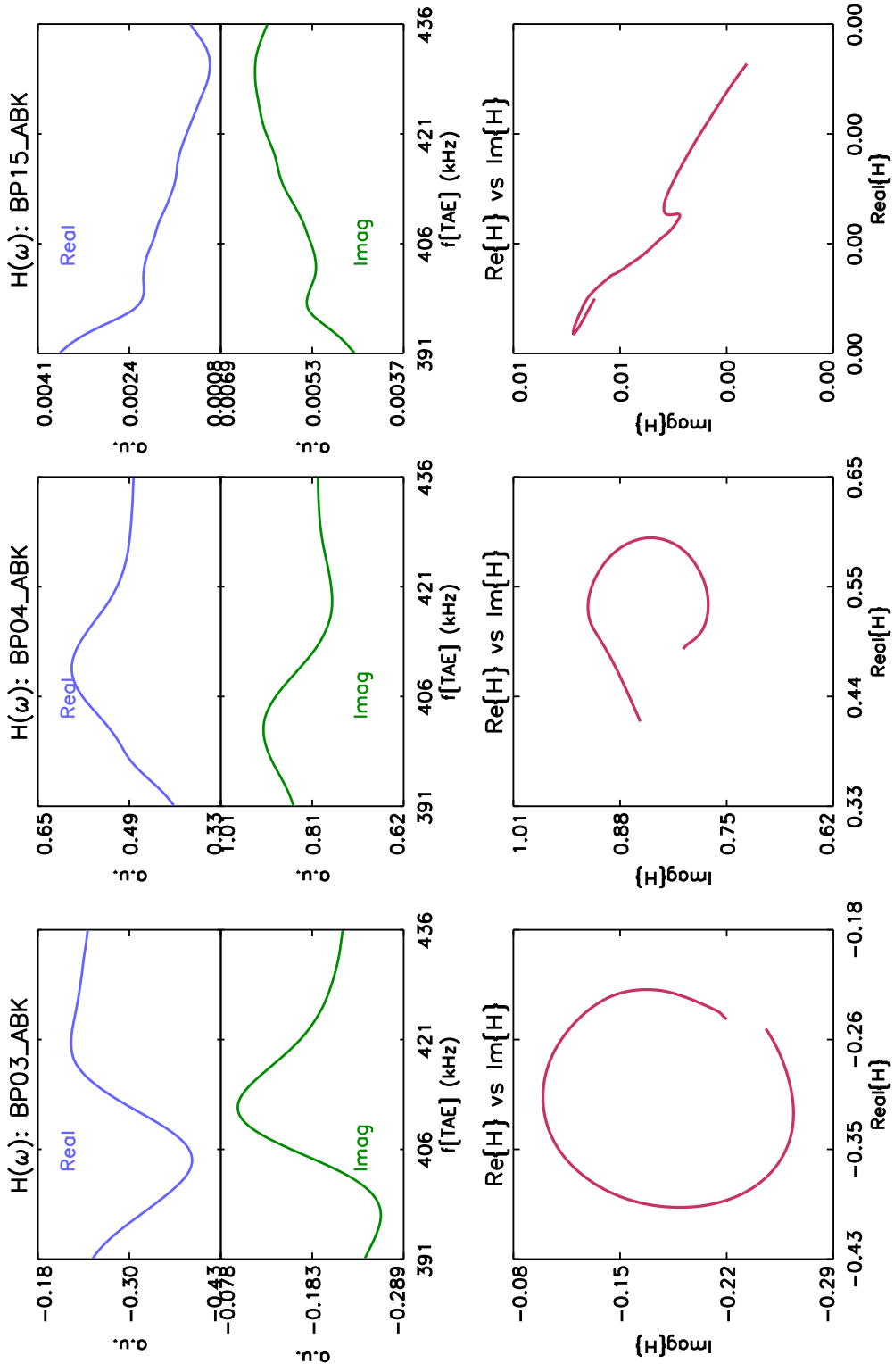

Figure 4-20: Synchronously detected signals for all coils on shot 1021003012 depicting the "turning" of the transfer function in the complex plane (1)

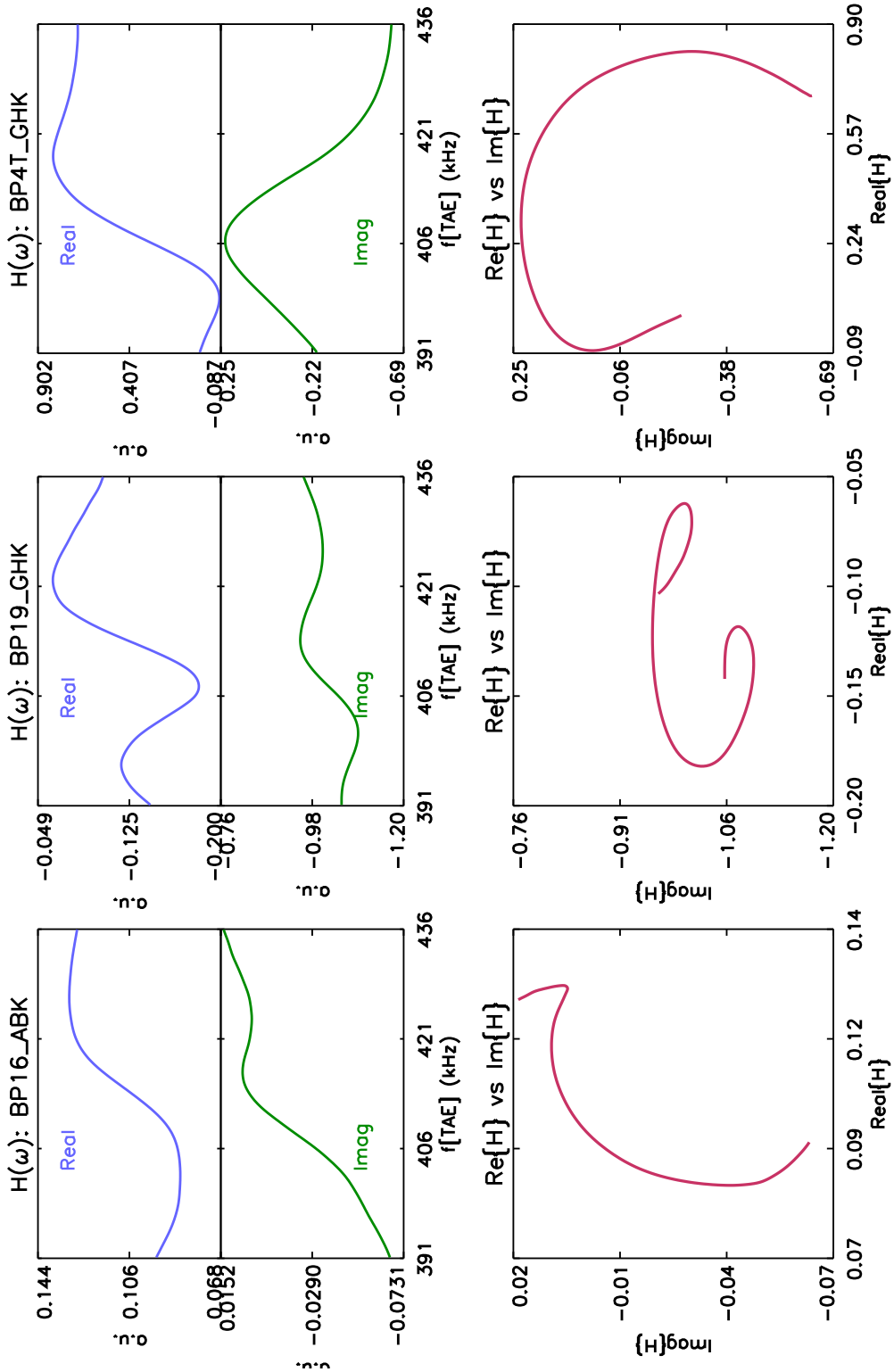

Figure 4-21: Synchronously detected signals for all coils on shot 1021003012 depicting the "turning" of the transfer function in the complex plane (2)

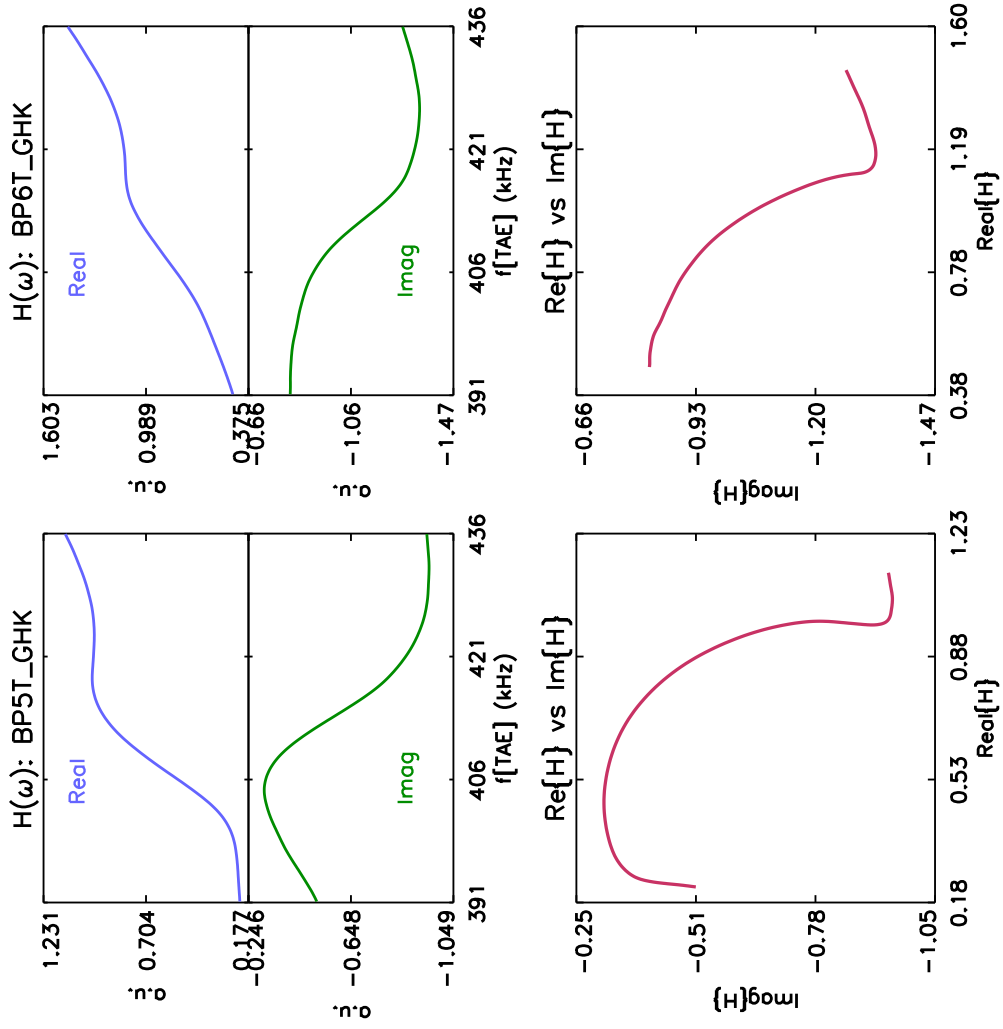

Figure 4-22: Synchronously detected signals for all coils on shot 1021003012 depicting the "turning" of the transfer function in the complex plane (3)

4.2.2 Damping Rates

A great advantage of the synchronous detection algorithm is that the complex transfer function calculated from the pick-up coil signals may be written in terms of complex conjugate poles $(p, p^{\star})$ and residues $(Res, Res^{\star})$ in the following form

$$H(\omega, x) = \frac{1}{2}\left[\frac{Res(x)}{i\omega - p} + \frac{Res^{\star}(x)}{i\omega - p^{\star}}\right] + D(\omega, x)$$

where the pole is defined as $p = i\omega_0 + \gamma$; ω_0 is the resonant frequency and γ is the difference between the damping rate and the growth rate due to fast particle drive. If no fast particles are present, as is the case for shots run on 1021003, then γ represents the damping rate of stable modes that have been excited by the Active MHD system. The variable ω refers to the theoretical TAE frequency computed as a function of time and used as the abscissa in the plots above. Spatial variation of the transfer function due to the different physical locations of the various pick-up coils is denoted by the variable x while background signal due in part to the unavoidable coupling of antenna flux is contained in the polynomial term $D(\omega, x)$. Since the resonance should be seen on all pick-up coil signals, a common pole is specified for each shot with residues unique to each coil. Defining a pole common to all pick-up coil signals reduces the associated statistical errors [27]. In addition, the computed residue for each coil yields information on the phase of the resonance at different locations and thus may be used to calculate the toroidal mode number.

In this way an algorithm may be developed to simultaneously fit the expression above to the entire set of synchronously detected pick-up coil signals. The result is

$$H_{fit}(\omega, x) = \frac{B(\omega, x)}{A(i\omega)}$$

for each coil such that the resonant denominator $A(i\omega)$, a polynomial of order nA containing the complex pole, is common to all pick-up coils signals. The numerator, meanwhile, is a polynomial of order $nB - 1$ specific to each coil. A routine developed by Jean-Marc Moret at the CRPP-Lausanne for fitting complex transfer functions such as outlined above during the experimental studies of TAE's may also be employed for this application, with some minor alterations in usage (see Appendix A).

The fitting algorithm is applied to each shot with the parameters $nA = 2$, $nB = 9$, maximum number of iterations = 2500, and tolerance of convergence = 10^{-8}. Solutions may be found using values of nB less than 9, however the fits produced by employing such a high order polynomial are of good quality. The output of the fitting routine may then be plotted over the original data gleaned from the synchronous detection calculation in order to illustrate good agreement, as depicted in Figure 4-23 for shot 1021003012.

As shown, there is excellent agreement between the synchronously detected transfer functions and the calculated fits from the fitting algorithm for all coils used as input. Coils such as BP15_ABK with peculiarly shaped transfer functions are omitted from this analysis in order to improve reliability of the estimated damping rates. Due to the large order of the numerator polynomial used in the fitting calculation, even sharp deviations from a strictly circular shape may be reproduced with good accuracy as seen on coils BP19_GHK and BP5T_GHK.

The poles and residues are calculated from the fitted complex transfer function and yield information on the damping rate and phase of the excited mode, as previously stated. In the case of shot 1021003012 above, the results of the fitting procedure give

Coil name	**Phase (rad)**
BP03_ABK	2.1317
BP04_ABK	-0.018253
BP16_ABK	2.4372
BP19_GHK	2.5247
BP4T_GHK	1.0675
BP5T_GHK	0.95044
BP6T_GHK	0.75403

$$\omega_0 = 409.3517 \text{ (kHz)}$$

$$\frac{\gamma}{\omega_0} = 2.7468\ \%$$

Recalling the definition of coil phase from Section 3.2.1

$$\varphi = m\theta + n\phi$$

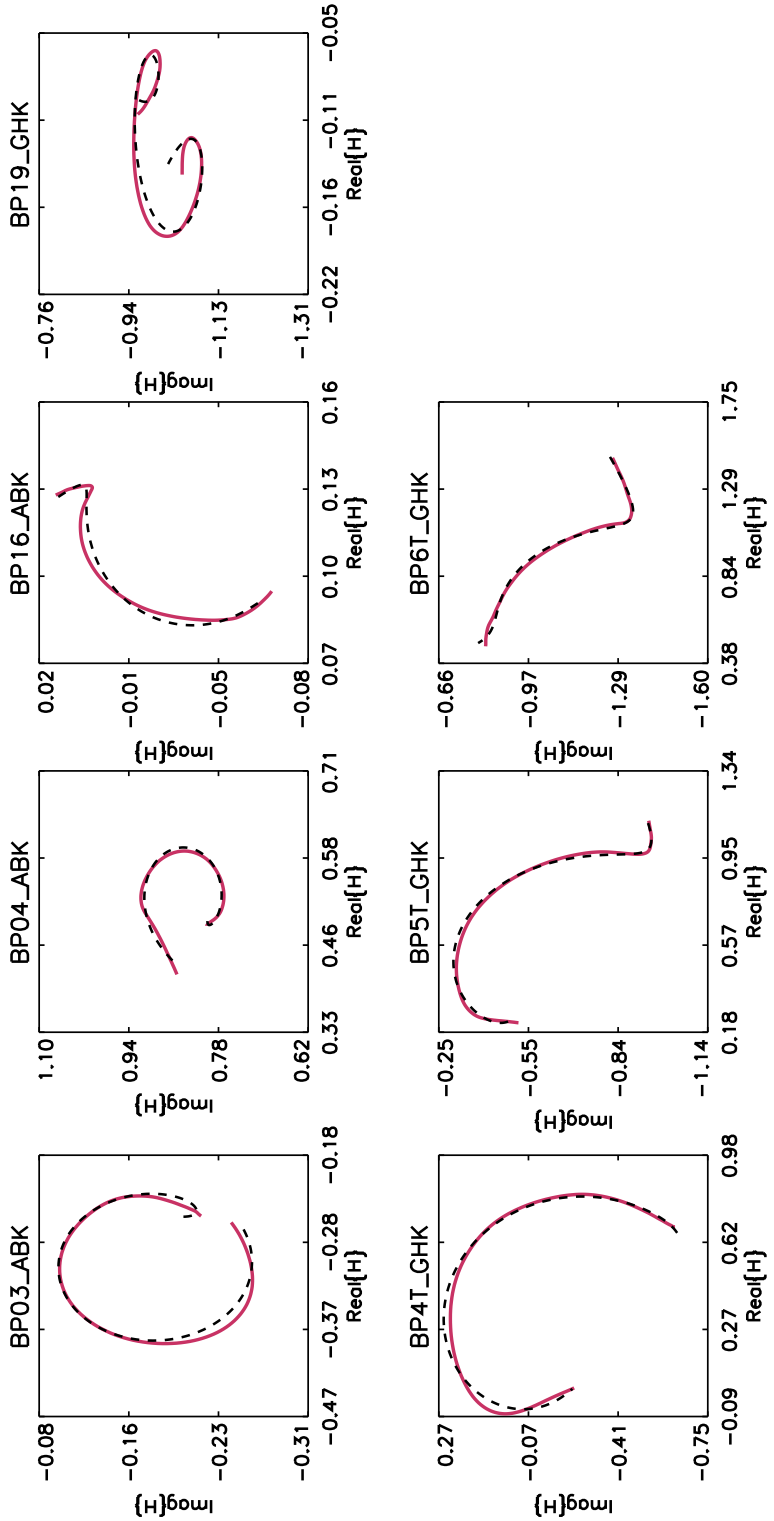

Figure 4-23: Complex transfer functions simultaneously calculated by fitting routine for synchronously detected coil signals (except BP15_ABK) on shot 1021003012

for coils at the same poloidal location, the phase should be a linear function of coil angle. The toroidal mode number n is then simply the slope of the line fitted to the corresponding data points. Magnetic pick-up coils BP4T_GHK, BP5T_GHK, and BP6T_GHK are indeed at the same poloidal angle, each separated by $\sim$.04 rad or $\sim$3.8 cm. The line-of-best-fit is shown in Figure 4-24 along with the data from those three pick-up coils. Solutions by this method are not possible for all shots on

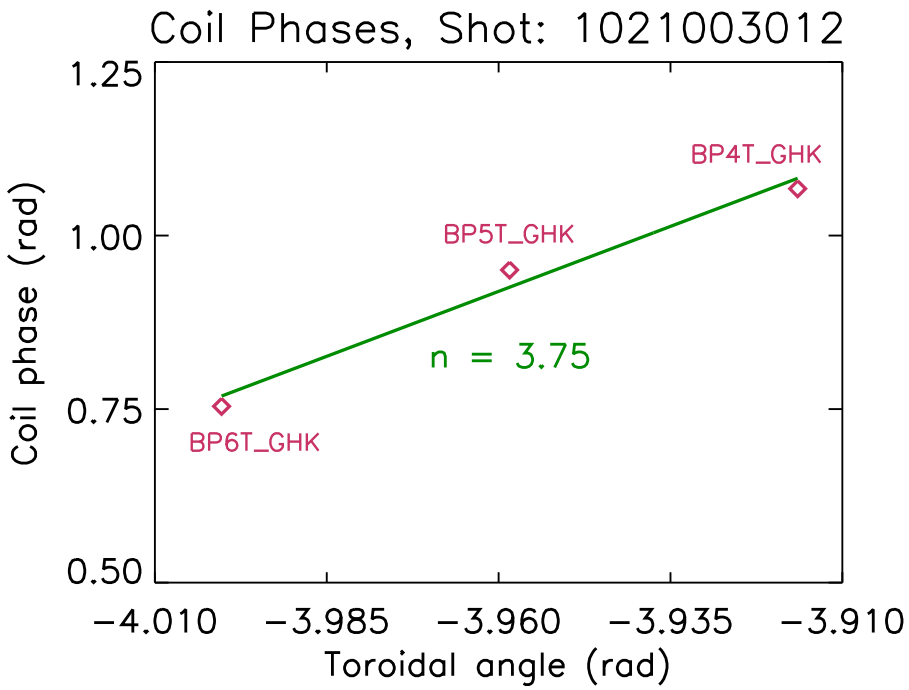

Figure 4-24: The calculated toroidal mode number is the slope of the best-fit line connecting data points for coils BP4T_GHK, BP5T_GHK, and BP6T_GHK

run day 1021003. Often the algorithm does not converge to an adequate solution for simultaneous fitting of all coils with useable synchronously detected pick-up coil signals. An example of this is shot 1021003025 for which the fitting solutions are shown in Figure 4-25. Both shot 1021003024 and 1021003025 were diverted discharges and this might account for the lack of a solution with sufficient convergence.

The results of the fitting calculation applied to all shots on run day 1021003 are summarized in Table 4.1 and Figure 4-26. Quantities of interest are the resonant frequency ω_0, the damping rate γ/ω_0, and toroidal mode number n.

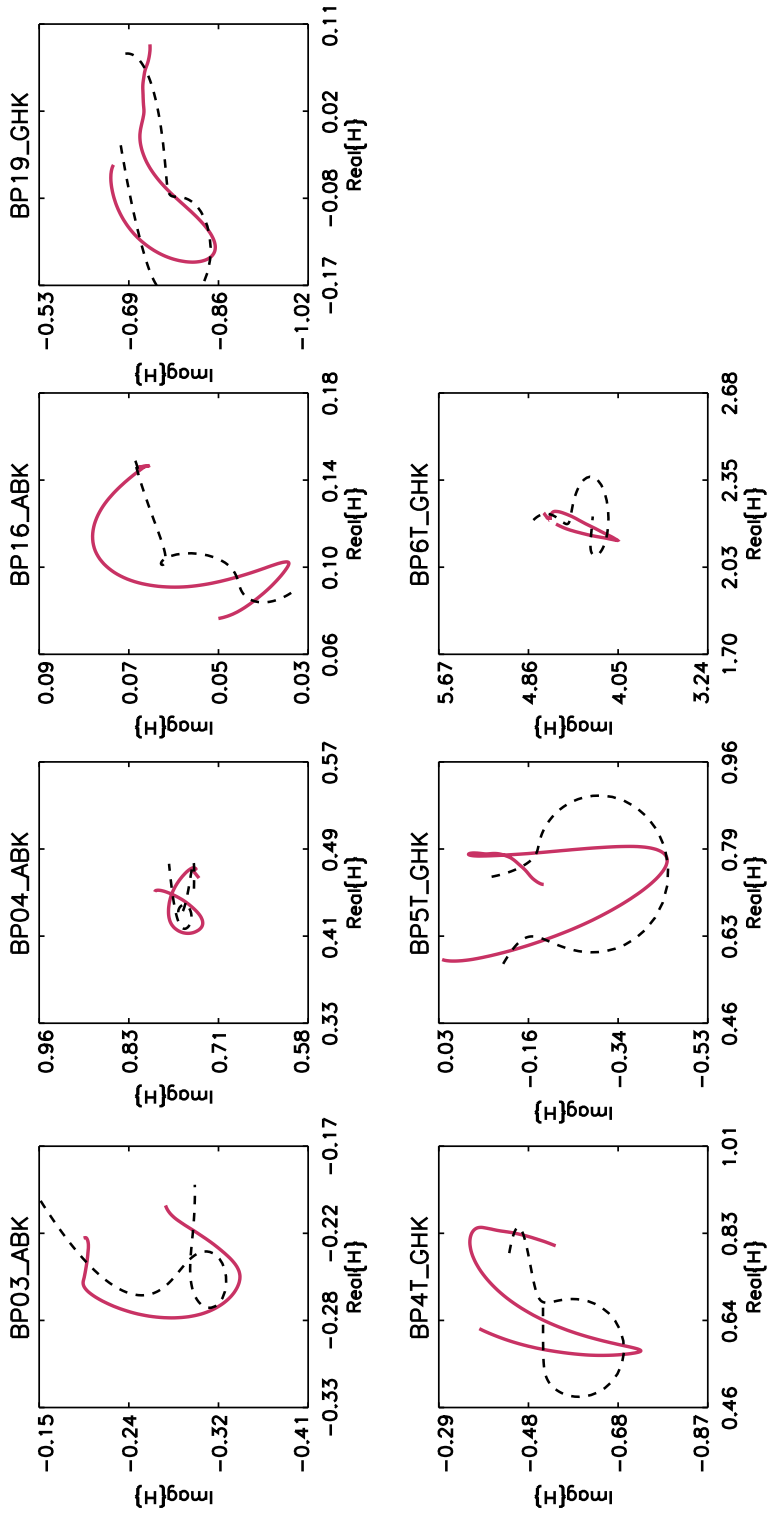

Figure 4-25: Complex transfer functions simultaneously calculated by fitting routine for synchronously detected coil signals (except BP15_ABK) on shot 1021003025

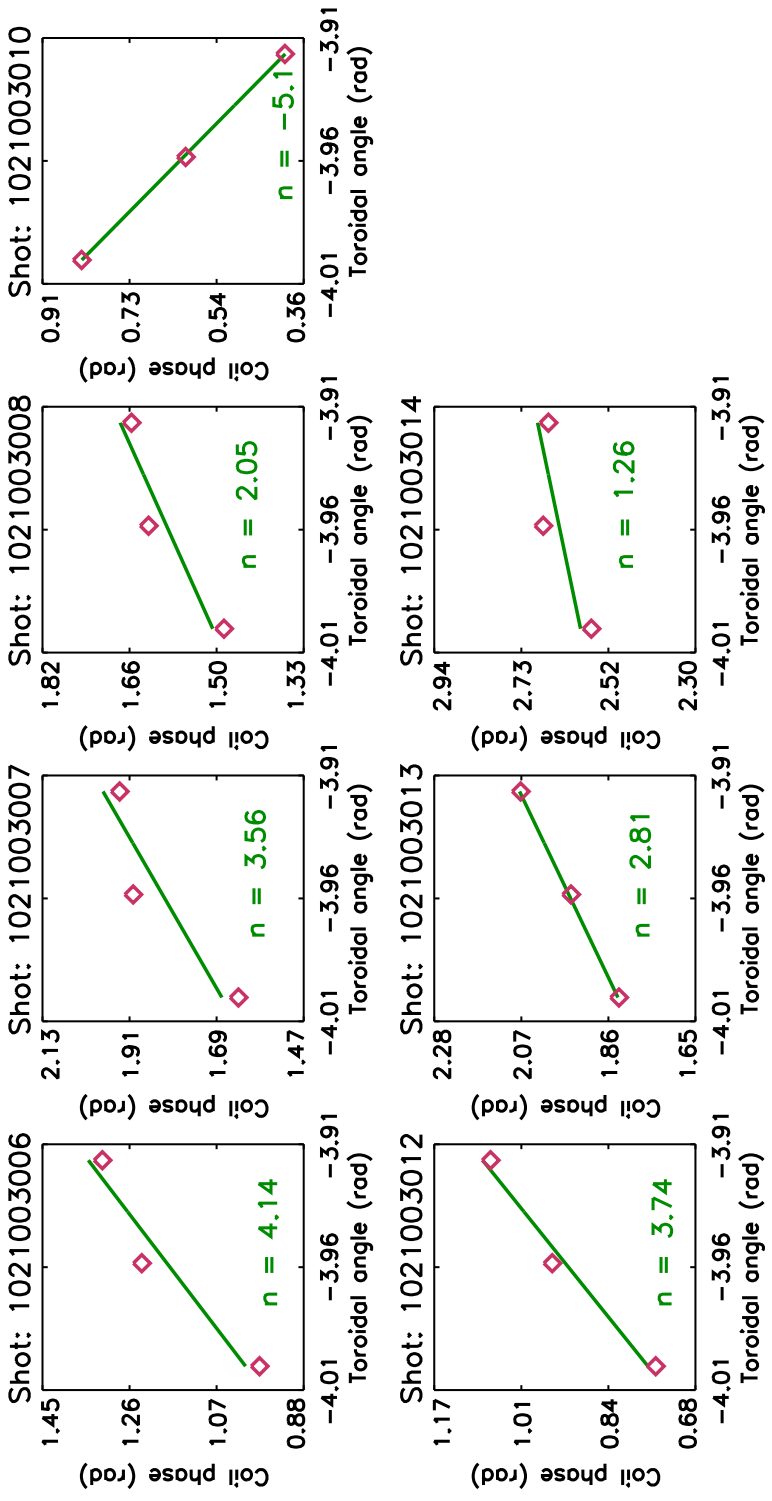

Figure 4-26: Calculated toroidal mode numbers for all shots on run day 1021003

Shot #	ω_0**(kHz)**	$\gamma/\omega_0(\%)$	n
1021003006	408.8	3.13	4.14
1021003007	430.6	2.84	3.56
1021003008	431.7	2.50	2.05
1021003010	398.1	1.82	-5.16
1021003012	409.4	2.75	3.75
1021003013	413.9	3.96	2.81
1021003014	389.7	2.58	1.26

Table 4.1: Output of the fitting routine including resonant frequency, damping rate and toroidal mode number for all shots on run day 1021003

Chapter 5

Conclusions

The motivation for studying global electromagnetic modes, such as Toroidal Alfvén Eigenmodes (TAE's), on present tokamaks is easily understood in the context of application to the burning plasma regime. Some classes of electromagnetic waves may interact with the supra-thermal population of ionized particles in a tokamak plasma when the wave resonates with the particles' motion. That is, interaction occurs when the phase velocity of the wave matches the velocity of an energetic particle. Fast particles in the tail of the distribution accelerated by conventional heating schemes, as well as fusion-born alpha particles, may satisfy this resonance criterion. Furthermore, the free energy contained in the pressure gradient of the energetic particles may be sufficient to drive the resonant modes unstable, leading to possible redistribution or prompt loss of these particles.

As a planned next-step experimental fusion device, the International Thermonuclear Experimental Reactor (ITER) will achieve reactor relevant conditions such that the overall fusion gain Q will be greater than 5 - 10, the so-called burning plasma regime. A significant population of alpha particles is created by fusion reactions between deuterium (D) and tritium (T), and the thermalization of these particles on the background ions as they slow from a birth energy of $\sim$3.5 MeV will provide the necessary heating to maintain a "steady-state" plasma temperature. However, since the velocity of the fusion-born alpha particles is larger than the typical phase velocity of TAE modes on ITER, it is possible that the interactions described above will

arise. Redistribution or outright loss of alpha particles from the core of the plasma may result in incomplete thermalization and consequently a lowering of the plasma temperature as energy is transported out of the core. Fusion cross-section for the DT reaction decreases with temperature and thus the final outcome of this process is a decrease in Q and a possible quenching of the fusion burn altogether.

The instability drive for electromagnetic waves supportd by the gradient in the fast particle pressure profile is opposed by several natural damping mechanisms. If the combined damping is sufficiently strong, unstable mode growth may be limited or even prevented altogether. Past studies have shown that the strength of each damping mechanism is dependent on the specific plasma conditions and excited mode number. Therefore, it is insightful to ascertain the magnitude of the total damping rate of TAE's under conditions relevant to a next-step burning plasma device such as ITER. An understanding of the conditions necessary to maximize mode damping rates and thus avoid mode destabilization leading to degradation of the fusion burn is desired. Because of the high toroidal magnetic field and electron densities, the Alcator C-Mod tokamak is well-suited to undertake this type of study.

In lieu of destabilizing TAE modes by interactions with resonant fast particles, damping rates may be ascertained by driving the modes at low amplitude with antenna structures. In the absence of fast particles, the measured growth rate is then simply the total damping rate of the mode provided by all damping mechanisms. A new diagnostic system on Alcator C-Mod, the Active MHD Spectroscopy system, was designed in part to carry out experimental studies of this kind. Installation was completed in September 2002 in order that the system be operated during the Fall 2002 C-Mod run campaign. Two rectangular, Bitter plate antennas are mounted to the C-Mod vacuum vessel wall near H-port. A high power amplifier excites the antennas in the frequency range of 100 - 900 kHz where TAE modes are expected, and magnetic fluctuation diagnostics measure the response of the plasma to this external excitation.

Modes were indeed excited by the Active MHD system on two run days during the fall: 1021003 and 1021107. Although both constant antenna excitation and frequency

sweeping shots were run on these two days, clearer results were obtained for constant frequency shots. This may be attributed in part to the very limited bandwidth of the impedance matching circuit employed with the ENI AP400B amplifier, but also the framework for analysis of frequency sweeping shots is not yet complete. Experimental data on shots with constant antenna excitation consists of magnetic pick-up coil, antenna current, and antenna voltage signals digitized at $\sim$2.5 MHz by the ACQ16 PCI-based digitizer. FFT analysis of the pick-up coil signals, specifically BP03_ABK, shows discernible peaks in the spectrogram for most shots on run day 1021003. Moreover, these peaks occur in general at the time when the theoretical TAE frequency at the $q = 1.5$ surface approaches the Active MHD excitation frequency (constant at 420 kHz). In addition, the magnitude of the toroidal magnetic field on axis at the time of maximum signal amplitude in the 420 kHz component of the FFT exhibits a square root dependence characteristic of all Alfvénic modes. These facts point to the conclusion that the excited modes were indeed TAE modes.

A synchronous detection algorithm developed for the software suite MATLAB provides a statistically robust method for calculating the damping rate of the excited mode. First, the experimental transfer function- defined as the ratio of the synchronously detected pick-up coil signal to the synchronously detected antenna current signal- is computed. This transfer function varies in time as the plasma conditions evolve throughout the discharge. A resonance in the transfer function is detected by noting exactly when the phase of each coil signal "turns" in the complex plane. Finally, a MATLAB routine developed specifically to fit experimental transfer functions to a numerical formula is applied with a few small alterations: the theoretical TAE frequency at the $q = 1.5$ surface is used as the frequency input. The output of this procedure determines the damping rate, resonant frequency, and coil phase. Toroidal mode numbers are calculated by fitting a line to the phase data from several closely-spaced pick-up coils in the same poloidal plane. Table 4.1 summarizes the results from the fitting routine for all shots on 1021003 with sufficient convergence.

In general, these results are similar to experimentally determined TAE mode damping rates in JET discharges. Resonant frequencies computed by the fitting

algorithm are close to 420 kHz in most cases, differing by at most ∼7%. It should be noted, however, that altering the input data slightly produced slight changes in the output of the fitting procedure. In addition, due to large uncertainties in the experimental quantities used as inputs for the fitting procedure, it is probable that the calculated damping rates are accurate only within a factor of ∼2. That is, for TAE modes with $1 \leq n \geq 5$, damping rates of order 2 - 4% are observed for limited discharges on Alcator C-Mod.

Based on calculations of the toroidal mode number spectrum that may be excited with only one operational Active MHD antenna, the computed n numbers are also in line with expectations. It is, however, somewhat disturbing that the calculated n numbers are not close to integer values since n must be strictly quantized in a toroidal plasma. Furthermore, it is unclear as to why only one discharge on run day 1021003 produced a solution with a negative toroidal mode number (shot 1021003010). Assuming that the detected mode is a propagating wave with a preferential direction, why that direction should vary between shots with very similar equilibrium configurations is undetermined.

5.1 Limitations and Questions

Undoubtedly the most conspicuous inadequacy in the process of characterizing TAE modes in C-Mod is the inability to analyze shots with frequency sweeping. The main impediment to the analysis at this point is likely the very narrow-band filtering needed to sufficiently compute the complex pick-up coil, antenna current, and antenna voltage signals necessary for synchronous detection. For a shot with constant frequency excitation, a bandpass filter with 5 kHz bandwidth is typically employed. However, sweeping of the excitation frequency may in general range over 50 kHz or more. A moving bandpass filter may therefore be needed to adequately filter out background components not related to Active MHD excitation. Since this particular method of TAE excitation will play an important role in the future operation of the Active MHD Spectroscopy system (see section 5.2, it is imperative that a better algorithm

to analyze frequency sweeping shots be quickly developed.

The high level of background noise not associated with the Active MHD system points out the largest limitation in effective use of the system to excite, detect, and ultimately characterize modes in the plasma. Simply put, the small magnetic flux output of the Active MHD antennas corresponds directly to the low signal levels detected on magnetic fluctuation diagnostics. It is likely that most of the inaccuracy of the calculations is due in large part to the small difference in excited mode amplitude relative to the background signal. This is perhaps most clearly exhibited by the inability of the fitting procedure to obtain a satisfactory solution for shot 1021003022 in which only 20 W of power was output by the amplifier. The low level of antenna current may produce such a low level of excited mode signal above the background that a convergent solution is simply not possible. Increasing the current flowing in the antennas by employing a larger power supply to feed higher power amplifiers as well as installing two additional Active MHD antennas will unquestionably ease this limitation somewhat. The latter solution also provides assistance for relieving another glaring limitation detailed below.

Another limitation that must be addressed is the inability of the Active MHD system to drive modes with $n \geq 5$. As shown, the calculated n numbers of excited modes on run day 1021003 (if they are to be believed) were in the range of 1 - 5. It is most worthwhile, as was discussed in Chapter 1, to examine medium- to high-n TAE's because these modes are predicted to be the most unstable in a future burning plasma device. However, the driven toroidal mode number spectrum of the Active MHD antennas is peaked at $n = 0$ and falls off with increasing n. The probability of exciting higher n number modes may be increased by increasing the number of antennas in the C-Mod vacuum vessel and applying certain phasing patterns.

Despite the believable results from the synchronous detection and fitting routines, lingering questions regarding the validity of the algorithm remain. As one example, the cut-off frequency of the low-pass Butterworth filter was set to 10 Hz because at this cut-off value a very low level of background noise was observed during a simulation with signals of constant phase. It should be pointed out, however, that

essential information may be lost if the phase of the signal varies at a rate greater than this cut-off frequency. It is unknown at this time as to how important this effect may be in introducing inaccuracies into the calculations. The various questions associated with the applicability of the synchronous detection routine could possibly be eliminated by appropriately benchmarking the procedure. This involves creating a signal with known parameters (resonant frequency, damping rate, n number, etc.) and passing this data through the synchronous detection routine in order to compare the known and computed characteristics. Unfortunately, this important verification task was not completed due in large part to lack of time.

5.2 Future Work

There is a large amount of work that must be carried out in the future in order to alleviate the limitations discussed above and ultimately optimize the excitation, detection, and characterization of TAE modes in Alcator C-Mod plasmas. Installation of additional Active MHD antennas as well as augmenting the system current are important modifications that will definitely increase the flexibility of the system while simultaneously improving the ease of measurement. Clearly, refinement of the synchronous detection routine to address some of the limitations and outstanding questions is necessary as well. A definitive test that validates the algorithm employed in synchronously detecting the important signals is much needed. Finally, a more long term goal involves incorporation of an "active" feedback control mechanism in order to track the excited modes over the course of an entire discharge. In this way the mode damping rate may be computed as the plasma evolves, allowing for a more complete understanding of how the damping rate depends on plasma conditions. Eventually the mode damping rate calculated in real time may provide a feedback signal for other systems, such as lower hybrid current drive, and therefore aid in holding the plasma at higher β for longer durations.

Appendix A

Codes

Data acquisition and analysis included in this thesis was performed with the MATLAB software suite licensed for use at the PSFC. Graphs and plots were in most cases generated using simple IDL scripts. Included below is source code for the most important functions related to the synchronous detection algorithm (see Figure 4-10).

Relevant Active MHD signals acquired at high frequency by the ACQ16 digitizer are stored in the C-Mod "MAGNETICS" tree. Accessing these signals for analysis is accomplished by the MATLAB user-defined function "getdata.m".

```
% Getdata routine for Active MHD synchronous detection algorithm
% Vb has multiple columns for multiple pick-up coil signals
%
% Inputs:   shot = shot to be analyzed
%           dumname = string of coil name (without BP) - argument present
%                     for getting data from only one coil
%
% Outputs:  Vb = pick-up coil signal
%           t = time base of ACQ16 digitizer
%           Ia = antenna current signal
%           r = amplifier voltage signal
%           cname = dumname (coil name input)

function [Vb,t,Ia,r,cname]=getdata(shot,dumname)
mdsconnect('alcserv2');
```

```
%Open tree and retrieve data arrays
mdsopen('magnetics',shot);
 quev='y';
 count=1;
 while upper(quev) == 'Y'
     if (nargin == 1)
        dumname(count,:) = magcoils(shot,count-1);
        Vb(:,count)=mdsvalue(['\magnetics::top.active_mhd.signals:bp',...
                dumname(count,:)]);
        count=count+1;
        quev=input('Use another coil? (y/n): ','s');
    else
        Vb(:,count)=mdsvalue(['\magnetics::top.active_mhd.signals:bp',...
                dumname(1,:)]);
        quev='n';
     end
 end
 if (nargout == 2)
      t=mdsvalue('dim_of(\MAGNETICS::TOP.ACTIVE_MHD.SIGNALS:HPFG_VOUT)');
 elseif (nargout == 3)
     t=mdsvalue('dim_of(\MAGNETICS::TOP.ACTIVE_MHD.SIGNALS:HPFG_VOUT)');
     Ia=mdsvalue('\MAGNETICS::TOP.ACTIVE_MHD.SIGNALS:I_GH_UPPER');
 elseif (nargout == 4)
     t=mdsvalue('dim_of(\MAGNETICS::TOP.ACTIVE_MHD.SIGNALS:HPFG_VOUT)');
     Ia=mdsvalue('\MAGNETICS::TOP.ACTIVE_MHD.SIGNALS:I_GH_UPPER');
     r=mdsvalue('\MAGNETICS::TOP.ACTIVE_MHD.SIGNALS:V_GH_UPPER');
 elseif (nargout == 5)
     t=mdsvalue('dim_of(\MAGNETICS::TOP.ACTIVE_MHD.SIGNALS:HPFG_VOUT)');
     Ia=mdsvalue('\MAGNETICS::TOP.ACTIVE_MHD.SIGNALS:I_GH_UPPER');
     r=mdsvalue('\MAGNETICS::TOP.ACTIVE_MHD.SIGNALS:V_GH_UPPER');
     cname=dumname;
 end
```

The next step in the synchronous detection process is to calculate the transfer function between a specific magnetic fluctuation coil and the excitation generated by the Active MHD antennas. This step involves bandpass filtering of the pick-up coil data, mixing signals with REF and $REF90$ (signal 90° out of phase to the driving voltage signal), low-pass filtering the results, resampling at much lower frequency, and then dividing V_{sync} by I_{sync} to yield H. Included below is the function "tfunc.m" which yields the synchronously detected transfer function and its time base for all

input coil signals.

```
% Active MHD Synchronous detection routine for calculating experimental
% transfer functions
%
% Inputs:   shot = C-Mod shot (used in taefreq.m and shotstr)
%           t = time array from getdata.m
%           Vb = pick-up coil signal from getdata.m
%                with size [length(t),# of coils]
%           r = r from getdata.m (usually V_antenna)
%           Ia = Ia from getdata.m (usually I_antenna)
%           frange = [fmin, fmax] for bandpass filter and FFT plot
%           win = nfft for specgram
%           numplf = 0 for no filter response plots, >0 for bandpass and
%                    lowpass filter response
%           numplfft = 0 for no FFT spectrogram, >0 for spectrogram
%           numplH = 0 for no plot, > 0 to plot Re{H} and Im{H} vs. ftae
%                    and Re{H} vs. Im{H}
%
% Outputs:  ts = resampled time base for H
%           H = complex transfer function (same size as ts)

function [ts,H]=tfunc(shot,t,Vb,r,Ia,frange,win,numplf,numplfft,numplH)

%Filter the data in frange and plot filter response + spectrogram
nt=size(t,1);
nor=5;        %filter order
fny=.5/(1000*(t(100)-t(99)));   %Nyquist frequency in kHz
fcnorm=frange./fny;
if numplf == 0
    pldum=0;
else
    pldum=fny;
end
cnum=size(Vb,2);
for i=1:cnum
    Vfilt(:,i)=butterfilt(t,Vb(:,i),nor,fcnorm,0,pldum);
    [sig,fcomp,tstep]=specgram(Vfilt(:,i),win,2.4444e6,win);
    fcomp=fcomp/1000;    %in kHz
    if i == 1   %use only the first coil for resonance calculation
        sig1=sig;
        fcomp1=fcomp;
        tstep1=tstep;
    end
```

```
    if numplfft > 0
        figure
        imagesc(tstep,fcomp,20*log10(abs(sig))),...
            axis([t(1) t(nt) frange(1) frange(2)]),...
            axis xy, xlabel('Time (s)'), ylabel('Frequency (kHz)'),...
            colormap(jet)
    end
end
ifreq=find(min(abs(fcomp1-420)) == abs(fcomp1-420));
itres=find(max(sig1(ifreq,:)) == sig1(ifreq,:));
t_res=tstep1(itres);
itres=find(min(abs(t-t_res)) == abs(t-t_res));

%Truncate without last 1024 points
ind1=1;
ind2=nt-1024;
tc=t(ind1:ind2);
V=Vfilt(ind1:ind2,:);
REF=r(ind1:ind2)/max(abs(r));
REF90=imag(hilbert(REF));
I_ant=Ia(ind1:ind2);

%Mixer
for i=1:cnum
    In_V(:,i)=REF.*V(:,i);
    Quad_V(:,i)=REF90.*V(:,i);
end
In_I=REF.*I_ant;
Quad_I=REF90.*I_ant;

%Lowpass filter + resample
nor=3;
fcnorm=.01/fny;
frs=1;  %resampling frequency in kHz
for i=1:cnum
    [In_Vrs(:,i),ts]=butterfilt(tc,In_V(:,i),nor,fcnorm,frs,pldum);
    [Quad_Vrs(:,i),ts]=butterfilt(tc,Quad_V(:,i),nor,fcnorm,frs,0);
end
[In_Irs,ts]=butterfilt(tc,In_I,nor,fcnorm,frs,0);
[Quad_Irs,ts]=butterfilt(tc,Quad_I,nor,fcnorm,frs,0);

%Synchronous output + transfer function
I_sync=complex(In_Irs,Quad_Irs);
for i=1:cnum
    V_sync(:,i)=complex(In_Vrs(:,i),Quad_Vrs(:,i));
```

```
    H(:,i)=V_sync(:,i)./I_sync;
end

%Plot the transfer function
if numplH > 0
    for i=1:cnum
        Hplot(shot,ts,H(:,i),[.1 1.5])
    end
end
```

The above function utilizes the lower level function "butterfilt.m" to filter the data given a range of frequencies normalized to the Nyquist frequency of the sampled data (or simply a cut-off frequency for low-pass filtering). This file is also provided below.

```
% Routine for Butterworth filtering and optional downsampling
%
% Inputs:   tc = time base of input signal
%           sig = signal to be filtered
%           nor = order of Butterworth filter
%           fcnorm = frequency range of filter;
%                    [1 x 2] for bandpass, [1 x 1] for lowpass
%           numrs = 0 for no resampling, = frs resampling rate in kHz
%           fny = 0 for no plotting, = Nyquist frequency for response plot

function [sfr,tout]=butterfilt(tc,sig,nor,fcnorm,numrs,fny)

[b,a] = butter(nor,fcnorm);
if fny > 0
    [htr,om] = freqz(b,a,4096);
    figure
    plot((om/pi)*fny,20*log(abs(htr))),...
        xlabel('Frequency (kHz)'), ylabel('Filter response (dB)')
end

if numrs == 0
    sfr = filter(b,a,sig);
else
    sfilt = filter(b,a,sig);
    np=ceil(1000*numrs*(tc(size(tc,1))-tc(1)));
```

```
    tout=linspace(tc(1),tc(size(tc,1)),np);
    sfr=interp1(tc,sfilt,tout,'linear');
    tout=reshape(tout,size(tout,2),1);  %change to nx1 arrays
    sfr=reshape(sfr,size(sfr,2),1);
    tout=tout(2:size(sfr,1)-1);    %cut off the first and last points
    sfr=sfr(2:size(sfr,1)-1);
end
```

Once all transfer functions for each shot have been detected, one may employ the fitting routine "fits.m". This script attempts to fit the experimental transfer function to a numerical equivalent given parameters nA, nB, tol, and $maxiter$ (the maximum number of iterations of the fitting procedure). Output from this routine may then be used to calculate the damping rate, resonant frequency, and phase of each coil. Information on individual coil phasing is then employed to derive a toroidal mode number, n.

```
% Routine for calculating and plotting fits for all coils, all shots

%function Hfits=fits(ft,realH,imagH)
clear all
mdsconnect('alcserv2');
shot_nums=[1021003006; 1021003007; 1021003008; 1021003009;...
           1021003010; 1021003012; 1021003013; 1021003014;...
           1021003022; 1021003024; 1021003025; 1021107034;];
%shot=1021003012;
trange_sh=[[.99 1.26];[1.17 1.47];[1.15 1.42];[1.30 1.48];...
          [.8 1.01];[1.02 1.23];[.92 1.19];[.71 .95];...
          [.78 1.02];[.56 .8];[.74 .98];[1.1 1.26];];
%trange=[1.02 1.23];
qshot=input('Shot # ');
indsh=find(qshot == shot_nums);
shot=shot_nums(indsh);
trange=trange_sh(indsh,:);

for i=1:size(shot,1)
    ques=input('Get data? (y/n): ','s');
    if upper(ques) == 'Y'
    coils=allcoils(shot(i));
    pathstr=['C:\Temp\DATf\',num2str(shot(i)),'\'];
```

```
for j=1:size(coils,1)
    %Open .dat files
    fid=fopen([pathstr,'imH',num2str(coils(j,:)),'.dat'],'r');
    imagH=fscanf(fid,'%f');
    fclose(fid);
    fid=fopen([pathstr,'reH',num2str(coils(j,:)),'.dat'],'r');
    realH=fscanf(fid,'%f');
    fclose(fid);
    Hcal(:,j)=complex(realH,imagH);
end
fid=fopen([pathstr,'ts',num2str(shot(i)),'.dat'],'r');
ts=fscanf(fid,'%f');
fclose(fid);
fid=fopen([pathstr,'ft',num2str(shot(i)),'.dat'],'r');
ftae=fscanf(fid,'%f');
fclose(fid);
end

%Now do the fitting
ques=input('Do fitting? (y/n): ','s');
if upper(ques) == 'Y'
    dum=find(ts >=trange(i,1) & ts <=trange(i,2));
    om=2*pi*ftae;
    om_fit=om./max(om);
    nA=2; nB=9;
    %cnums=[1,2,4:8];
    cnums=input('Coil nums: ');
    [fitden, fitnum, RAB, gamom, Hfits] = ...
        sti(om_fit,Hcal(dum,cnums),nA,nB,2500,1e-8);
end
Hplot_coils(shot(i),coils(cnums,:),ts,trange(i,:),Hcal(:,cnums),Hfits)

%Now save the data
ques=input('Save data? (y/n): ','s');
for j=1:size(Hfits,2)
    [Res(1:nA,j),Pole(1:nA,j),D,Rrpd]=...
        rpdcov(fitden,fitnum(j,:),RAB);
    Pole(:,j)=max(om)*Pole(:,j);
    phase(j)=angle(Res(1,j));
    disp(['phase(',num2str(coils(cnums(j),:)),') = ',...
          num2str(phase(j))])
    if upper(ques) == 'Y'
        fid=fopen([pathstr,'\Fit\imfit',...
            num2str(coils(cnums(j),:)),'.dat'],'w');
        adu=fprintf(fid,'%-6.6f ',imag(Hfits(:,j)));
```

```
            fclose(fid);
            fid=fopen([pathstr,'\Fit\refit',...
                num2str(coils(cnums(j),:)),'.dat'],'w');
            adu=fprintf(fid,'%-6.6f ',real(Hfits(:,j)));
            fclose(fid);
        end
    end
    if size(phase,2) > 1
        phase=reshape(phase,size(phase,2),1);
    end
    gam = abs(real(Pole(1)));
    f0 = abs(imag(Pole(1)))/(2*pi);
    disp(['f0 = ',num2str(f0),' kHz'])
    disp(['gamma/w0 = ',num2str(100*gam/(2*pi*f0)),' %'])

    %n number analysis for 4T,5T,6T coils
    mdsopen('magnetics',shot(i));
    cnames=mdsvalue('\MAG_RF_COILS:NODENAME');
    cnames=cell2mat(cnames);    %now in an array
    cnames=cnames(:,3:8);
    dum1=mdsvalue('\MAG_RF_COILS:PHI_AB');
    dum2=mdsvalue('\MAG_RF_COILS:PHI_GH');
    dumphi=vertcat(dum1,dum2);
    %disp(cnames(28:30,:))
    phi=pi*dumphi(28:30,:)./180;
    lco=polyfit(phi,phase(length(phase)-2:length(phase)),1);
    x_line=linspace(min(phi),max(phi),100);
    n_line=(lco(1)*x_line)+lco(2);
    ntor=lco(1)
    figure
    plot(phi,phase(length(phase)-2:length(phase)),...
        'linestyle','none','marker','o')
    hold on
    plot(x_line,n_line)
end
```

As stated in section 4.2.2, this script uses the complex transfer function fitting routine "sti.m" developed by Jean-Marc Moret at the CRPP-Lausanne. The source code for this important function is provided below.

```
function [A,B,RAB,gamom,Hfit] = sti(w,H,nA,nB,maxiter,tol)
```

```
% STI   Frequency domain transfer function reduction
%    [A,B] = STI(W,H,NA,NB) fits to an experimental transfer
%    function H(W), W in rad/s, with a rational function of s
%    B(s)/A(s) with degrees NB-1 and NA. Multi-output transfer
%    functions are represented by multi-column H. Additional
%    input arguments specify the maximum number and the tolerance
%    to stop iterations. Optional output arguments return the
%    covariance matrix of [A(2:NA+1) B(1,:) B(2,:) ...] and the
%    fitted transfer function.

% default arguments and argument size
if nargin < 5, maxiter = 20; end
if nargin < 6, tol = 1e-4; end
[nw,nH] = size(H);
if length(w) ~= nw, error...
        ('Frequency and transfer function size mismatch'), end
n = max([nA nB-1]); nth = nA + nB*nH;
if nth > 10, ktrace = 1:nA; else, ktrace = 1:nth; end

% normalise w
wnorm = max(w(:)); w = w/wnorm;
z = rep(j*w(:),n).^rep(1:n,nw);

% initial A guess and preallocation
A = [zeros(1,nA) 1]; th = zeros(nth,1);
phi = sparse([],[],[],nH*nw,nth,nH*nw*(nA+nB));
phy = zeros(nH*nw,1);

% iterate
G = Inf; iter = 0;
while iter < maxiter & G > tol
 iter = iter + 1;

 % fitting
 Aw = 1. ./ polyval(A,z(:,1)); % weights
 for kH = 1:nH
  kk = (kH-1)*nw+1:kH*nw;
  phi(kk,1:nA) = rep(Aw,nA) .*...
      [rep(H(:,kH),nA-1).*z(:,nA-1:-1:1) H(:,kH)];
  phi(kk,nA+(1+(kH-1)*nB:kH*nB)) = rep(Aw,nB) .*...
      [-z(:,nB-1:-1:1) -ones(nw,1)];
  phy(kk) = -Aw .* z(:,nA) .* H(:,kH);
 end
 thnew = real(full(phi'*phi)) \...
```

```
     real(full(phi'*phy)); % \ to use Cholesky
 G = norm(th - thnew);

 % trace
 %clc
 %disp('norm of difference = '), disp(G)
 %disp('prev    new'), disp([th(ktrace) thnew(ktrace)])
 simple=thnew(ktrace);
 gamom=0.5*simple(1)/simple(2);
 %disp('g/om (to be multiplied by fpeak/fmax)'), disp(gamom)
 % new A coefficient
 th = thnew; A = [1;th(1:nA)]';

end
disp('# of iterations = '), disp(iter)

% B coefficients dispatching and fitted H
B = zeros(nH,nB); Hfit = zeros(nw,nH);
Aw = 1. ./ polyval(A,z(:,1));
for kH = 1:nH
 B(kH,:) = th(nA+(1+(kH-1)*nB:kH*nB))';
 Hfit(:,kH) = polyval(B(kH,:),z(:,1)) .* Aw;
end

% covariance
phy = phi*th - phy;
RAB = real(phy'*phy)/nw/nH * (real(full(phi'*phi)) \...
    eye(nth)); % \ to use Cholesky

% denormalise
A = A .* wnorm.^(0:nA); B = B .* rep(wnorm.^(nA-nB+1:nA),nH,1);
Aw = 1:nA;
for kH = 1:nH, Aw = [Aw nA-nB+1:nA]; end
Aw = wnorm.^Aw;
RAB = RAB .* rep(Aw,nth) .* rep(Aw',nth);
```

Bibliography

[1] John Wesson. *Tokamaks*. Clarendon Press, 1997.

[2] J. P. Friedberg. *Ideal Magnetohydrodynamics*. Plenum Press, 1987.

[3] J. D. Lawson. Some criteria for a power producing thermonuclear reactor. *Proceedings of the Royal Society B*, 70(6), 1957.

[4] D. C. Pridmore-Brown. Alfvén Waves in a Stratified Incompressible Fluid. *Phys. Fluids*, 9(7):1290+, July 1966.

[5] C. Uberoi. Alfvén Waves in Inhomogeneous Magnetic Fields. *Phys. Fluids*, 15(9):1673+, September 1972.

[6] A. Hasegawa and C. Uberoi. The Alfvén Wave. United States DOE, 1982.

[7] A. Hasegawa and L. Chen. Kinetic processes in plasma heating by resonant mode conversion of Alfvén wave. *Phys. Fluids*, 19(12):1924+, December 1976.

[8] L. Chen and A. Hasegawa. Plasma heating by spatial resonance of Alfvén wave. *Phys. Fluids*, 17(7):1399+, July 1974.

[9] K. Appert et. al. Excitation of Global Eigenmodes of the Alfvén Wave in Tokamaks. *Plasma Phys.*, 24(9):1147+, 1982.

[10] D. A. D'Ippolito and J. P. Goedblood. Mode Coupling in a Toroidal, Sharp-Boundary Plasma– I. Weak-Coupling Limit. *Plasma Phys.*, 22:1091+, 1980.

[11] C. E. Kieras and J. A. Tataronis. The shear Alfvén continuous spectrum of axisymmetric toroidal equilibria in the large aspect ratio. *J. Plasma Phys.*, 28:395+, 1982.

[12] C. Z. Cheng, L. Chen, and M. S. Chance. High-n Ideal and Resistive Alfvén Waves in Tokamaks. *Annals of Physics*, 161:21+, 1985.

[13] C. Z. Cheng and M. S. Chance. Low-n shear Alfvén spectra in axisymmetric toroidal plasmas. *Phys. Fluids*, 29(11):3695+, November 1986.

[14] J. A. Snipes. Fast Particle Driven Modes in Alcator C-Mod. In *Proc.* 26^{th} *EPS Conference on Controlled Fusion and Plasma Phys.*, number 23J in Europhysics Conference Abstracts, Maastricht, June 1999. European Physical Society.

[15] G. Y. Fu and J. W. Van Dam. Stability of the global Alfvén eigenmode in the presence of fusion alpha particles in an ignited tokamak plasma. *Phys. Fluids B*, 1(12):2404+, December 1989.

[16] C. Z. Cheng. Alpha particle destabilization of the toroidicity-induced Alfvén eigenmodes. *Plasma Phys. B*, 3(9):2463+, September 1991.

[17] F. Zonca and Liu Chen. Resonant Damping of Toroidicity-Induced Shear-Alfvén Eigenmodes in Tokamaks. *Phys. Rev. Lett.*, 68(5):592+, February 1992.

[18] R. R. Mett and S. M. Mahajan. Kinetic theory of toroidicity-induced Alfvén eigenmodes. *Phys. Fl.*, B4(9):2885+, September 1992.

[19] N. N. Gorelenkov and S. E. Sharapov. Resonant Damping of Toroidicity-Induced Shear-Alfvén Eigenmodes in Tokamaks. *Phys. Scr.*, 45:163+, 1991.

[20] G. Y. Fu, C. Z. Cheng, and K. L. Wong. Stability of toroidicity-induced Alfvén eigenmode in axisymmetric toroidal equilibria. *Phys. Fl.*, B5(11):4040+, November 1993.

[21] R. Betti and J. P. Freidberg. Stability of Alfvén gap modes in burning plasmas. *Phys. Fl.*, B4(6):1465+, June 1992.

[22] E. J. Strait. Stability of Neutral Beam Driven TAE Modes in DIII-D. *Nucl. Fusion*, 33(12):1849+, 1993.

[23] K. L. Wong. First Evidence of Collective Alpha Particle Effect on Toroidal Alfvén Eigenmodes in the TFTR D-T Experiment. *Phys. Rev. Lett.*, 76(13):2286+, March 1996.

[24] K. L. Wong et. al. Excitation of Toroidal Alfvén Eigenmodes in TFTR. *Phys. Rev. Lett.*, 66(14):1874+, April 1991.

[25] R. B. White et. al. Toroidal Alfvén eigenmode-induced ripple trapping. *Phys. Plasmas*, 2(8):2871+, August 1995.

[26] A. Fasoli et. al. Alfvén eigenmode experiments in tokamaks and stellerators. *Plasma Phys. Control. Fusion*, 39:B287+, 1997.

[27] A. Fasoli et. al. Overview of Alfvén Eigenmode Experiments in JET. *Nucl. Fusion*, 35(12):1485+, 1995.

[28] D. Testa et. al. The effect of plasma shaping on the damping of low n Alfvén eigenmodes in JET tokamak plasmas. *Nucl. Fusion*, 41(7):809+, 1999.

[29] G. T. A. Huysmans et. al. MHD Spectroscopy Modelling the Excitation of TAE Modes by an External Antenna. In *Proc.* 20^{th} *EPS Conference on Controlled Fusion and Plasma Phys.*, number 17C, Part I in Europhysics Conference Abstracts, Geneva, June 1993. European Physical Society.

[30] L. Villard et. al. Alfvén Gap Modes in Elongated Plasmas. In *Proc.* 20^{th} *EPS Conference on Controlled Fusion and Plasma Phys.*, number 17C, Part IV in Europhysics Conference Abstracts, Geneva, June 1993. European Physical Society.